Title
Develop an artificial lipid bilayer array platform and screen nanoparticle-membrane interactions

Author
Lu, Bin

Publication Date
2014

Peer reviewed|Thesis/dissertation

UNIVERSITY OF CALIFORNIA, Los Angeles

Develop an artificial lipid bilayer array platform and screen nanoparticle-membrane interactions

A dissertation submitted in partial satisfaction of the

requirements for the degree Doctor of Philosophy

in Biomedical Engineering

by

Bin Lu

2014

ABSTRACT OF THE DISSERTATION

Develop an artificial lipid bilayer array platform and screen nanoparticle-membrane interactions

by

Bin Lu

Doctor of Philosophy in Biomedical Engineering

University of California, Los Angeles, 2014

Professor Jacob J. Schmidt, Chair

Artificial lipid bilayers have many uses. They are well established for scientific studies of reconstituted ion channels, used to host engineered pore proteins for sensing, especially DNA sequencing, and can potentially be applied in nanoparticle toxicity screening. To better explore these applications, we have simplified the formation and electrical measurement of the traditional method using an apparatus that only requires fluid dispensation. We achieved simultaneous bilayer formation and measurement over a 32-element array with ~80% yield and

no operator input following fluid addition. Cycling these arrays resulted in the formation and measurement of 96 out of 120 possible bilayers in 80 minutes, a sustainable rate that could significantly increase with automation and greater parallelization. We have also used this bilayer array platform to study nanoparticles. The platform was validated for this purpose through probing the interaction between amine or carboxyl modified polystyrene nanoparticles and bilayers in conditions of different ionic strength, particle concentration, bilayer charge, and pH. We discovered that NH_2-NP ruptures bilayers by generating either transient or persistent pores on bilayers. Furthermore, we conducted nanoparticle toxicity screening with our bilayer array platform. For the first time we identified that CeO_2, Co_3O_4, and In_2O_3 can damage lysosomal membranes, and that Fe_3O_4, HfO_2, and TiO_2 cannot. Our platform confirmed that ZnO, C_{60}, CuO, Er_2O_3, Eu_2O_3, La_2O_3, and Gd_2O_3 disrupt lipid bilayers. The data from our bilayer array platform also indicated that the ability of nanoparticles to destruct membranes largely depends on the surface coating. In general, positive coating makes the particles more potent to membranes, and negative coating makes the particles safer. Our results about nanoparticles' ability to rupture bilayers are highly correlated with the cytotoxicity data in the literature. Therefore, our bilayer array platform has a great potential of being used for nanoparticle toxicity screening.

The dissertation of Bin Lu is approved.

Dino Di Carlo

Gerard C. L. Wong

H. Ronald Kaback

Jacob J. Schmidt, Committee Chair

University of California, Los Angeles

2014

TABLE OF CONTENTS

1. Introduction **1**
1.1 Lipid bilayer formation techniques **1**
1.1.1 Painted bilayers **1**
1.1.2 Folded bilayers **2**
1.1.3 Dip-tip bilayers **3**
1.1.4 Pore spanning bilayers **4**
1.1.5 Droplet interface bilayers **5**
1.2 Lipid bilayer applications **6**
1.2.1 Ion channel study with lipid bilayers **6**
1.2.2 Stochastic sensing and DNA sequencing with lipid bilayers **7**
1.2.3 Nanoparticle study with lipid bilayers **8**
1.3 Existing lipid bilayer array platforms and their limitations **9**
1.4 The unmet need **11**
2. Development of automatable, scalable and cyclical lipid bilayer array platform **12**
2.1 Introduction **12**
2.2 Materials and methods **16**
2.2.1 Chip design and fabrication **16**
2.2.2 Solution preparation **17**
2.2.3 Bilayer formation **17**
2.2.4 Apparatus for multiple bilayer formation and measurement **18**
2.3 Results and discussion **19**
2.3.1 Bilayer formation **19**
2.3.2 Screening of the aperture size **22**
2.3.3 Parallel bilayer formation and ion channel measurement **24**
2.3.4 Cycled, parallel bilayer formation and measurement **26**
2.3.5 Stabilize bilayer size with agarose **28**

2.4 Conclusion **30**

3. Validation of the lipid bilayer array platform for nanoparticle study with amine or carboxyl modified polystyrene nanoparticles **32**

3.1 Introduction **32**

3.2 Materials and methods **35**

3.2.1 Nanoparticle characterization **35**

3.2.2 Solution preparation, chip fabrication and bilayer array formation **35**

3.2.3 Electrical measurements of nanoparticle-bilayer interaction **36**

3.2.4 Data analysis **36**

3.3 Results and discussion **37**

3.3.1 Interaction of NH_2-NP or COOH-NP with bilayers of different lipid compositions **37**

3.3.2 Effect of ionic strength, particle concentration, bilayer surface charge and pH **41**

3.3.3 The presence of serum proteins attenuated the membrane activity of NH_2-NP **45**

3.3.4 Pore formation analysis **46**

3.4 Summary and conclusion **53**

4. Screening nanoparticle toxicity with lipid bilayer arrays **55**

4.1 Introduction **55**

4.2 Materials and methods **56**

4.2.1 Materials **56**

4.2.2 Nanoparticle characterization **57**

4.2.3 Solution preparation, chip fabrication and bilayer array formation **57**

4.2.4 Electrical measurements of nanoparticle-bilayer interaction **58**

4.2.5 Data analysis **58**

4.3 Results and discussion **59**

4.3.1 Interaction of nanopaticles with lipid bilayers **59**

4.3.2 Rare earth oxides (REOs) nanoparticles **61**

4.3.4 Nanoparticles of different surface coating **66**

4.3.5 Cobalt oxide **68**

4.3.6 Indium oxide **70**

4.3.7 Zinc Oxide, Copper oxide, and C_{60} fullerene **71**

4.3.8 Titanium oxide, Hafnium oxide, and Iron oxide 73
4.4 Conclusion..... 73
5. Conclusion and future plans 74
5.1 Conclusion..... 74
5. 2 Future plans..... 75
6. References..... 77

ACKNOWLEDGEMENTS

First, I would like to thank my advisor Prof. Jacob Schmidt for his guidance in the past 5 years. Without his insightful suggestions, ideas, discussions and visions, I would not have been able to complete this research. I would also like to thank my committee members Prof. Di Carlo, Prof. Gerard C. L. Wong, and Prof. H. Ronald Kaback for their time and suggestions. I also want to express my gratitude to my team members who contributed a lot to my research: Gayane Kocharyan, Tyler Smith, Isaac Caleb Wang, Henry Yong, Shayson Edwards, Andre Erfe Petersen, and Alexander Chen. I'd like to thank all other Schmidt lab members for their support during good and bad times, with special thanks to: Leyla Esfandiari, Shiv Acharya, Shiva A. Portonovo, Robert Tan, Carl Salazar, Ahmad El-Arabi, Dr. Jason Polous, and Dr. Takashi Nisisako.

Also, I want to thank my parents and my wife, Shenglan Peng, for their patience, love, and support. Because of them, the Ph.D. journey became easy. They motivated and inspired me when I faced difficulties and frustrations.

Lastly, I want to acknowledge that this research is supported by the National Institution of Health (NIH) and National Science Foundation (NSF).

Bin Lu

Los Angeles

September 2014

VITA

2009 B.S., Wuhan University, China,

Life Sciences and Biotechnology

2014 Ph.D. Candidate, University of California, Los Angeles,

Biomedical Engineering

PUBLICATIONS

Bin Lu, Gayane Kocharyan, Jacob Schmidt. Lipid bilayer arrays: cyclically formed and measured. *Biotechnology Journal* 2014, 9, 446-451

Bin Lu, Tyler Smith, Jacob Schmidt. Measurement of nanoparticle-membrane interactions with lipid bilayer arrays. 247th ACS National Meeting and Exposition, 2014

Bin Lu, Tyler Smith, Jacob Schmidt. Nanoparticle-membrane interaction studies with lipid bilayer array platform. 2014 Biophysical Society Meeting

Bin Lu, Gayane Kocharyan, Jacob Schmidt. High throughput bilayer formation platform. 2013 Biophysical Society Meeting

Bin Lu, Abha Jeurkar, Jacob Schmidt. Reconstitution of CLIC1 into droplet lipid bilayers. 2012 Biophysical Society Meeting

Chapter 1

1. Introduction

Artificial lipid bilayers are made of two lipid monolayers *in vitro* with a thickness of 5 nm to mimic cell membranes (Figure 1).The lipid molecules consist of a hydrophilic head and hydrophobic tail. When the bilayers are formed in solution, the hydrophilic head faces the aqueous phase and the tail is embedded inside the bilayers (Figure 1).

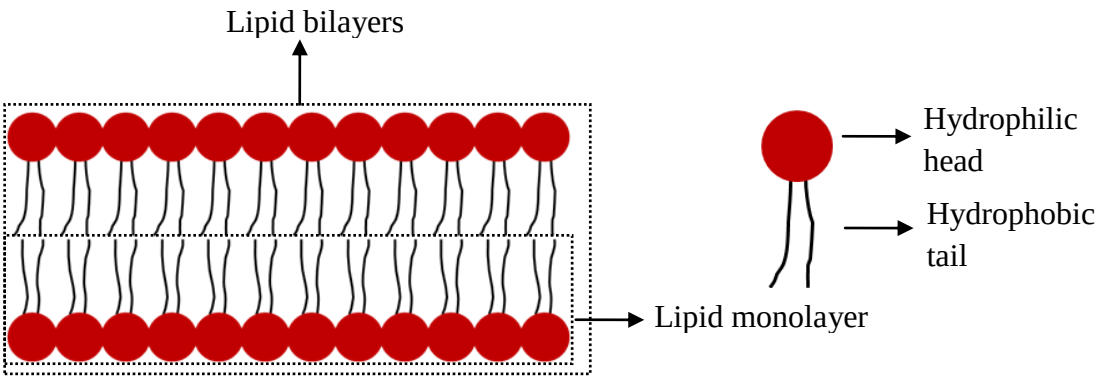

Figure1. Diagram artificial lipid bilayers. The bilayers comprise two lipid monolayers with the hydrophilic head facing the aqueous solution and the hydrophobic tail embedded inside.

Since the introduction of free-standing artificial lipid bilayers over 50 years ago[1], a variety of bilayer formation approaches have been developed which enable a high degree of control over the lipid composition and contents of the bilayer[2–6]. These approaches are painted, folded, tip-dip, pore-spanning bilayer, or droplet interface bilayer formation techniques.

1.1 Lipid bilayer formation techniques

1.1.1 Painted bilayers

The painted bilayer technique was first introduced by Mueller and co-workers[1]in 1962, and it

was also the first approach for formation of artificial lipid bilayers. The bilayers are made by spreading lipid-oil solution across an aperture on a thin hydrophobic film, which divides a chamber into two compartments filled with electrolyte solutions (Figure2A). The lipids self assemble into bilayers after the organic solution is absorbed by the hydrophobic film. The formation of bilayers is monitored by measuring the bilayer capacitance[7]. Once the capacitance exceeds a certain value, it is determined that the bilayers have formed. This approach requires the operator to be experienced in applying lipid solution across the aperture and to be able to determine when the bilayers form

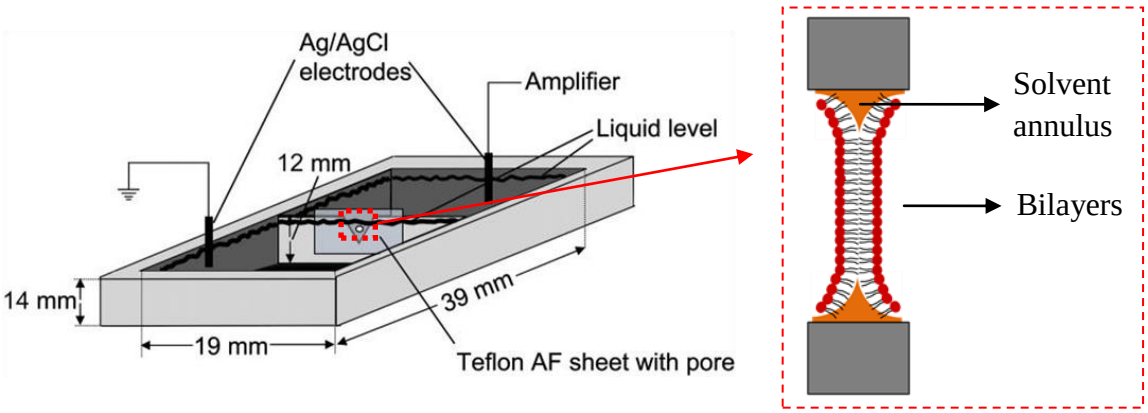

Figure 2. Schematics of apparatus for forming painted bilayers. (A) The apparatus is divided into two compartments by a Teflon film with a pore of about 50~300 μm in diameter. The liquid level is above the level of the pore. Ag/AgCl electrodes connected to an amplifier are inserted into solution to measure the electrical property of the bilayers. (B) Cross section view of the bilayers formed across the pore. After the bilayers form, there is still solvent annulus at the boundaries between bilayers and the edge of the pore. Adapted by permission from Elsevier: [Biophysical Journal][8], copyright (2003).

1.1.2 Folded bilayers

The folded bilayer technique was first introduced by Montal and Mueller in 1972[2]. With this

approach, the bilayers are formed by bringing pre-formed lipid monolayers together (Figure 3). The monolayers are formed by spreading a small amount of lipid-hexane solution over aqueous solution. After hexane evaporates, the two monolayers are brought into contact when the level of aqueous solution is raised via the movement of the trough or addition of more aqueous solution. Since there is no solvent left inside the bilayers, this method is also called solvent-free bilayer technique. This method has demonstrated great applications in the study of proteins that are sensitive to solvent. Another feature of this type of bilayers is that the lipid composition of the two monolayers could be different.

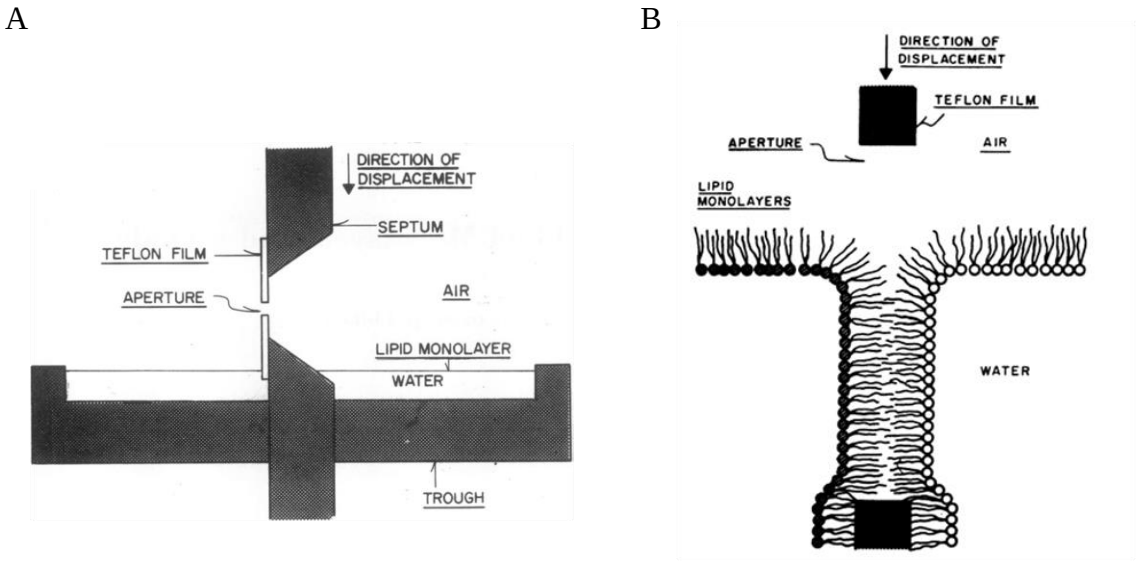

Figure 3. Diagram of formation of folded bilayers. (A) Apparatus for bilayer formation. (B) Formation of bilayers by folding two monolayers. Drawings are not to scale. Adapted from PNAS[2], copyright (1972).

1.1.3 Dip-tip bilayers

The dip-tip bilayer formation technique was invented by Corondo and Latorre to form bilayers on the tip of a glass pipet[4]. As shown in Figure 4, liposome solution is added to a container, and a monolayer forms at the water-air interface. A glass pipette tip is dipped into the liposome

solution for a few minutes and then pulled up. As a result, a lipid monolayer forms around the tip once it is in the air. Finally, the tip is inserted into the liposome solution again, resulting in the two monolayers in contact forming a bilayer.

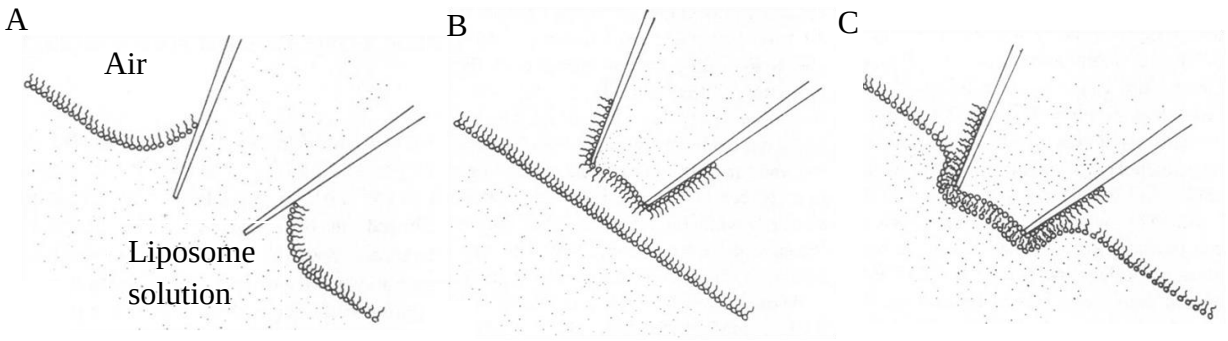

Figure 4. Schematics of bilayer formation with the dip-tip technique. (A) Lipid monolayer forms at the water-air interface, and the tip of a pipette is inserted into liposome solution. (B) The tip is lifted into air, resulting in the formation of a lipid monolayer around the tip. (C) The tip is dipped into the liposome solution to bring the two monolayers into contact to form bilayers. Adapted by permission from Elsevier: [Biophysical Journal] [4], copyright (1983).

1.1.4 Pore spanning bilayers

Researchers have also explored forming bilayers by spanning liposomes over nanopores[5,9,10]. With this techniques, liposomes are brought to close proximity of the pores on a solid substrate by electrical field[5], UV light, or gravity, and there they span over the pores. And then the liposomes are ruptured to form bilayers.

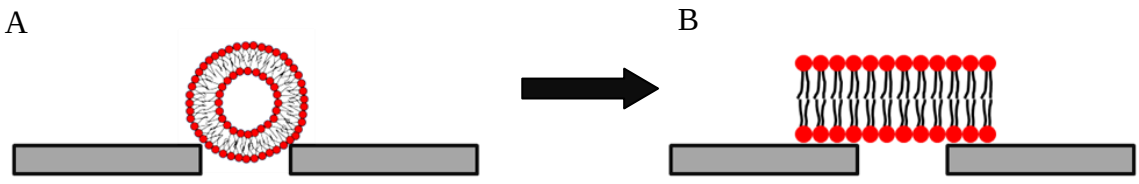

Figure 5. Process of forming pore spanning bilayers. (A) Span liposomes over the pores. (B) Liposomes are ruptured to form bilayers across the pore.

1.1.5 Droplet interface bilayers

The technique of droplet interface bilayers was first introduced by Tsofina and co-workers in 1966[6]. However, this method was not further pursued until the mid-2000s[11,12]. As shown in Figure 6[13], the method starts with putting two separate water droplets into oil with lipids either inside or outside the droplets. After a few minutes, monolayers form at the water-oil interface. Bilayers are formed by bringing the two droplets together through the movement of the electrodes to which the droplets are attached. Such bilayers, commonly called 'droplet interface bilayers'[6,12,14], are attractive technologically because of the simplicity of bilayer formation, which can essentially be reduced to a problem of droplet positioning, achievable using micromanipulators[12,14,15], microfluidic flows[16], gravity[17,18], or electric fields[19,20], among others. Droplet bilayers are highly amenable to technological applications because these approaches can be automated and parallelized[18,21].

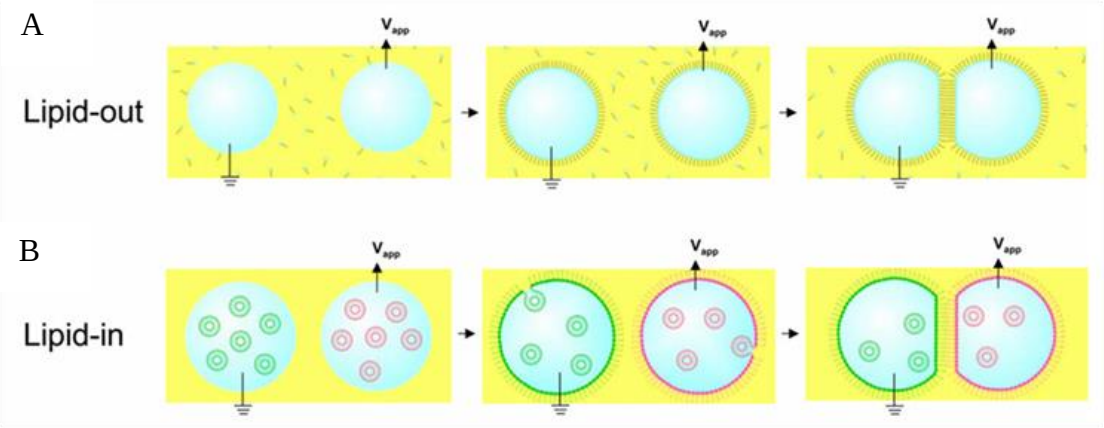

Figure 6. Formation of droplet interface bilayers. Two separate water droplets are attached to the end of two electrodes (not shown in the figure), respectively, and then they are immersed into oil

solution with either lipid outside (A) or inside (B) the droplets. Once the monolayers form on the droplet surface, they are brought into contact to form bilayers through the movement of electrodes. Adapted with permission from Asymmetric Droplet Interface Bilayers[13]. Copyright (2008) American Chemical Society.

1.2 Lipid bilayer applications

Along the course of technology development, a lot of applications with artificial lipid bilayers have also been demonstrated. So far, those applications include ion channel study, stochastic sensing, nanopore DNA sequencing, and membrane-nanoparticle interactions.

1.2.1 Ion channel study with lipid bilayers

The first ion channel measurement in lipid bilayers was conducted by Bean and co-workers in 1969[22]. In this experiment, the bilayers were made with the painted method. The ion channel was called excitability inducing material (EIM), which was extracted from *enterobacter cloacae*. EIM was self-incorporated into bilayers shortly after it was added to the solution. Since then, more bacterial ion channels such as Alamethicin[23], gramicidin A[24], α-hemolysin[25,26] were studied in lipid bilayers. Furthermore, a number of mammalian ion channels including potassium channels [27–32], sodium channels [33–39], calcium channels[40–46], chloride channels[47–50], and acetylcholine receptors[51,52]were incorporated into lipid bilayers to study their pore size, opening probability, gating behaviour, and even their responses to the change of factors like ionic strength, pH, and lipid compositions. Recently, lipid bilayers have also been used to investigate the response of ion channels to drugs[53,54] in the hope of replacing the expensive patch clamp based ion channel drug screening technology[55–59] someday. Despite that many mammalian ion channels have been successfully reconstituted into lipid bilayers, it is still premature to use lipid bilayer technology for ion channel drug screening. One of the biggest obstacles is the lack of an

easy, scalable, and automatable high throughput lipid bilayer array platform.

1.2.2 Stochastic sensing and DNA sequencing with lipid bilayers

Stochastic sensing is to use nanopores to detect analytes by monitoring the nanopores' conductance change resulted from the interaction between analytes and nanopores[60–62]. Lipid bilayers come into play when protein pores are used[63–65]. In this case, single protein pore is first inserted into lipid bilayers (Figure 7). When the analytes bind to the protein pore, the current passing through the pore is reduced (Figure 7). The reduction of the current is proportional to the volume of the analytes. The frequency of the binding event is governed by the concentration of the analytes. So far, metal ions[66,67], organic molecules[64], nitrogen mustards[68], neurotransmitters[69] and proteins[70,71] have been detected using lipid bilayer based stochastic sensors.

Among all the applications of lipid bilayer based stochastic sensing, DNA sequencing is of significant interest. The idea is to map out DNA sequence based on conductance change resulted from the presence of DNA in a nanopore. Because each DNA base has a different shape, it generates different current change when a base passes through the nanopore. As such, DNA sequence is derived from the change of currents. Since the first experiment of passing DNA or RNA through α-hemolysin pore conducted by Kasianowicz and co-workers[72] in 1996, lipid bilayer based nanopore DNA sequencing has attracted a lot of attention[73–77]. After some challenges like fast DNA translocation[78] and inaccuracy of sequence discrimination are gradually solved[79,80], lipid bilayer based DNA sequencing has shown great promise in sequencing the whole genome under $1000 within a day[81–86]. To achieve the goal, a lipid bilayer array platform is a must. Based on the data from Manrao and co-workers[84], we estimated that some 3000 parallel lipid bilayers are needed in order to sequence the whole genome within a day.

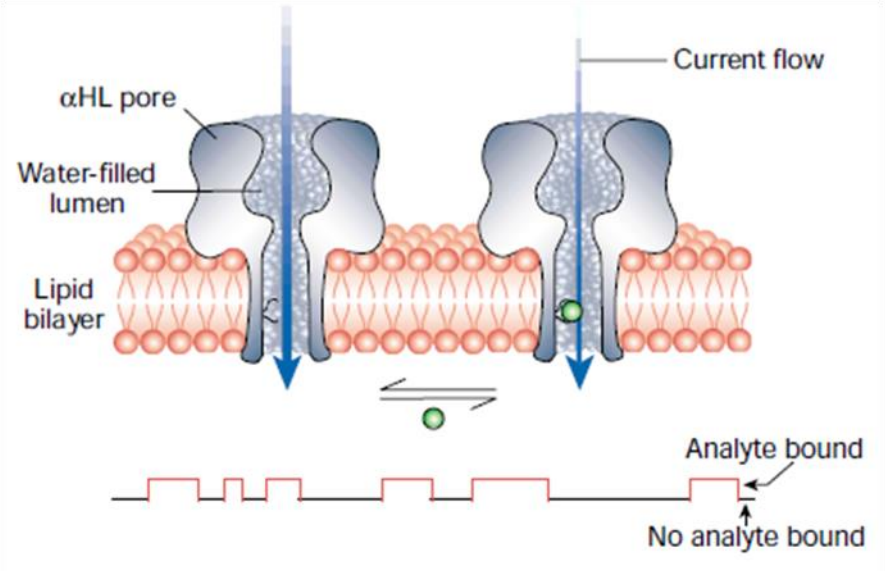

Figure 7. Schematics of stochastic sensing with α-hemolysin (αHL) pore incorporated into lipid bilayers. When analyte binds to the pore, it reduces the magnitude of the current. Adapted by permission from Macmillan Publishers Ltd: [Nature][87], copyright (2001)

1.2.3 Nanoparticle study with lipid bilayers

Recently, lipid bilayers have also been used to probe nanoparticle-membrane interactions. For this application, bilayers are made first and then nanoparticles are added to the solution, followed by the surveillance of any change to the bilayers[88] (Figure 8A). The detection methods include both electrophysiological measurement[88–91] and AFM imaging[92,93]. As shown in Figure 8, reported particle-bilayer interaction is either the change of bilayer capacitance or the change of conductance (pore formation). Through the bilayer-nanoparticle interaction study, the ultimate goal is to help determine the toxicity of nanoparticles[94]. Due to the low speed and low throughput, lipid bilayer experiments conducted at a single-plex level have only provided insightful information for a handful of nanoparticles such as amine or carboxyl modified polystyrene[90], amine silica nanoparticles[89], gold nanoparticles[93] and few other cationic

nanoparticles[92]. On the other hand, there are safety concerns regarding hundreds of thousands of different types of nanoparticles resulting from both natural and human activities. Therefore, a lipid bilayer array platform is strongly needed to accelerate the screening of nanoparticles.

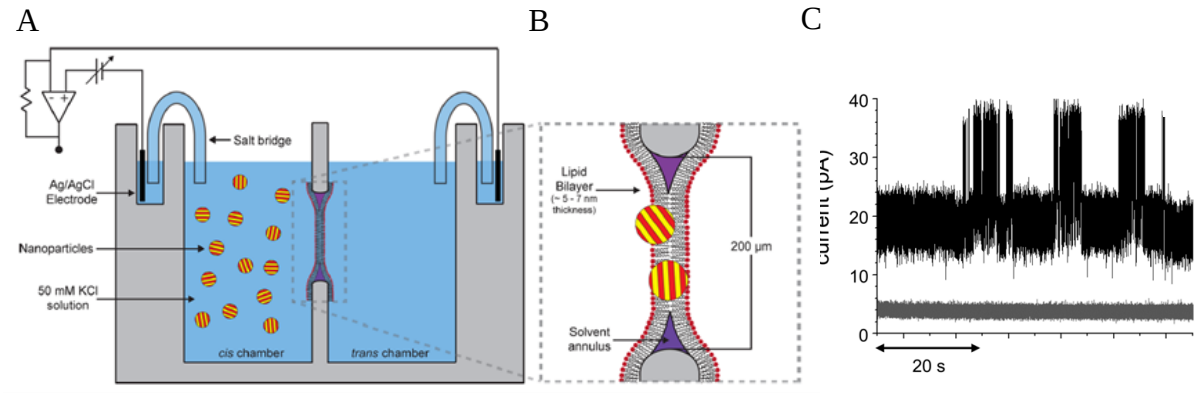

Figure 8. Schematics of nanoparticle-membrane interaction studied with lipid bilayers. (A) Nanoparticles were added to the solution in which there is a bilayer. (B) Bilayer capacitance was increased by nanoparticles. (C) Pore formation on bilayers caused by nanoparticles (black trace). Grey trace represents the current passing bilayers without nanoparticles. Adapted with permission from Electrical method to quantify nanoparticles interaction with lipid bilayers[88]and Electrophysiological characterization of membrane disruption by nannoparticles[89]. Copyright (2013&2011) American Chemical Society.

1.3 Existing lipid bilayer array platforms and their limitations

As we discussed above, those aforementioned applications would strongly benefit from an artificial lipid bilayer array platform that is scalable, automatable, and requires minimal operator input and equipment. To advance those applications, there have been a lot of efforts in developing such a platform.

Han and coworkers were able to make arrays of bilayers on nanopores based on the painting method[95]. Although the method significantly enhanced the stability of bilayers with life time over several days, its application was limited because of the challenges in determining membrane capacitance and inaccessibility to DC voltage.

Kleefen and coworkers also utilized nanopores to form bilayer arrays by spreading liposomes over the pores[96]. The competitive advantage of this technique was its capability of making solvent-free bilayers. However, it seemed that it was only suited for fluorescence-based analysis but not for electrical measurement, which limited its applications in ion channel study, nanopore sequencing and nanoparticle-membrane study. Similar problems also hindered the application of the micropatterned lipid bilayer arrays made by flowing liposome solution to a silica substrate[97] and the droplet interface bilayer arrays patterned on hydrogel[98].

Baaken and coworkers also used the painting principle to form parallel bilayers over 16 micropores on a so-called microelectrode cavities based device[99]. The device showed a reasonable yield of obtaining single channel recording of α-hemolysin. However, the yield of bilayer formation based on observed channel activities was only 50%. Also, only there were only 16 pores for bilayer formation at a time and the solution on one side of the bilayers was not accessible (2011).

Takeuchi and coworkers developed a microfabricated bilayer array chip with 96 bilayer formation sites with eight multiplexed fluidic and electrical connections[16,100]. Following sequentially pumped microfluidic flows of aqueous and lipid solutions, however, only 44 bilayers out of 96 attempts were formed and four sites were electrically measured simultaneously.

Our group developed a high throughput droplet bilayer platform using robotic 96 well pipettes capable of producing >2200 bilayers in two hours[18]. However, bilayer measurement occurred at a conventionally slow rate because the electrodes required individual, manual positioning.

1.4 The unmet need

In summary, despite all the endeavors, there is still a strong need to develop an artificial lipid bilayer array platform that is of high yield, scalable, automatable, accessible to electrical measurement, and requires minimal operator input and equipment in order to facilitate bilayer application in ion channel drug screening, nanopore DNA sequencing, and nanoparticle toxicity screening.

Chapter 2

2. Development of automatable, scalable and cyclical lipid bilayer array platform

2.1 Introduction

In the past, we automated bilayer formation and measurement by robotically manipulating a measurement electrode containing a sessile aqueous droplet[15]. Programmed motion of this electrode resulted in droplet bilayer formation upon contact with a second aqueous solution. To reduce the sensitivity of bilayer formation on electrode position in this system, we implemented a masking aperture constraining the droplet contact area[101].

Although the masking apertures greatly enhanced the bilayer stability and constrained bilayer size, there were alignment challenges in forming arrays of bilayers in parallel. First, it was difficult to precisely position electrodes to the aperture area for multiple wells simultaneously. Second, maintaining all the droplets at the same vertical level was proven to be critical for achieving high bilayer formation yield, and it was difficult.

To solve the alignment issues, we investigated the possibility of forming droplet interface bilayers without using the electrode pins to hang droplets (Figure 9B-E). In this method, the initial steps, including adding aqueous solution the bottom and lipid oil solution to the top, stay unchanged. Lipid monolayer (lower) forms at the water-oil interface. When the droplet is to be introduced, it is just added to the top well with a pipette instead of being hung from an electrode pin. Then, there is another monolayer (upper) forming at the new oil-water interface. The two monolayers are brought into contact to form bilayers by both gravity and hydrostatic pressure.

Since no electrode pins are used, and therefore there are no alignment issues, the method is

highly compatible with parallelization. Bilayer arrays are easily formed simultaneously on four chips with each containing eight wells (Figure 9F-I).

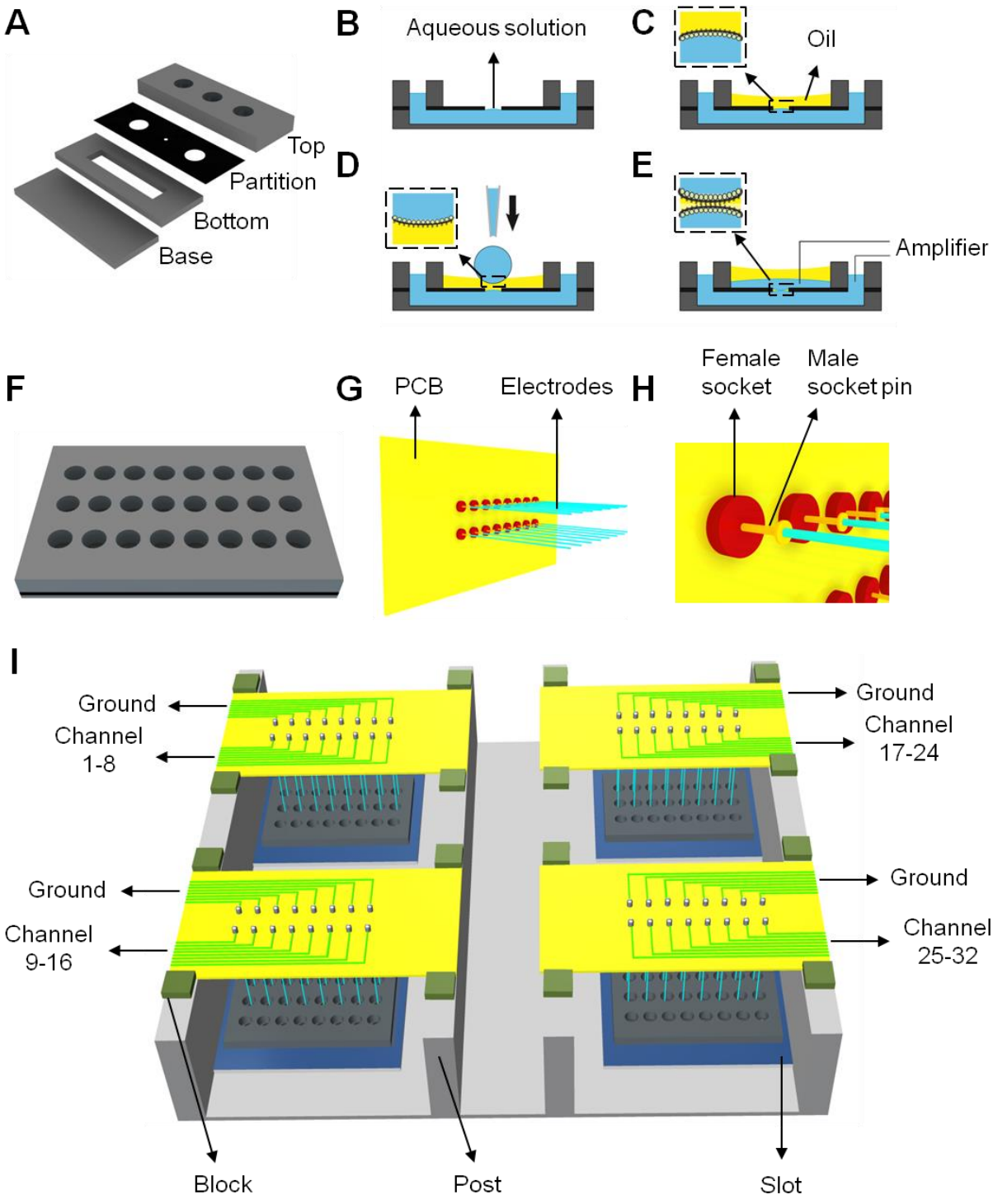

Figure 9. Bilayer formation schematic and apparatus. (A) Exploded diagram of chip assembly. The small pore in the center of the partition connects the center well at the top and the bottom channel. Side wells access the bottom channel from the top, facilitating top-mounted fluid and electrode access. (B) To form bilayers, aqueous solution is first added to the bottom channel through the outer wells. (C) Then oil is added to the central well for lipid monolayer formation (inset) at the aqueous/organic interface, constrained by the masking aperture. (D) Aqueous solution is then added to the central well to form another lipid monolayer (inset). (E) Finally, bilayer formation begins (inset) after adding additional lower aqueous solution through the outer well. (F) Chip schematic in which the wells in (A) are arrayed eight times. (G) Side view of a printed circuit board (PCB) to which eight pairs of bleached silver wire electrodes are connected. (H) Close-up of the socket connections allowing the electrodes to be easily removed from the PCB. (I) Apparatus schematic for simultaneous bilayer formation and measurements in 32 wells. Four eight-well chips are first placed into four slots in the bottom of the acrylic plate. After adding aqueous and organic solutions, four electrode PCBs are placed between the posts, putting the electrodes into contact with the aqueous solutions in the wells. A connector (not shown) on the edge of each PCB mates with an amplifier cable for electrical measurement of eight wells.

We have partially characterized this system and demonstrated its technological potential with simultaneous bilayer formation and ion channel measurement in parallel in 32 wells with yield of ~80%. Since preparation is simple and fast, the apparatus has the potential to be quickly cycled to measure additional multi-well arrays. To facilitate this, we also designed a modular system for array and electrode placement that allowed the measurement plates and electrodes to be quickly removed and accurately re-positioned. To demonstrate this, we manually cycled this apparatus four times (Figure 10), resulting in the formation and measurement of 120 wells at 80% yield in

approximately 80 minutes. Further scaling and use of automation hardware is straightforward and could further increase the measurement throughput. This platform has two benefits: the fluidic phases may be completely dispensed before electrode placement, and the electrodes may be imprecisely positioned into contact with the aqueous phases and still allow successful measurement. These benefits facilitate high throughput bilayer formation with parallel robotic fluid handling equipment and greatly increase measurement throughput without requirement of high precision motion control apparatus.

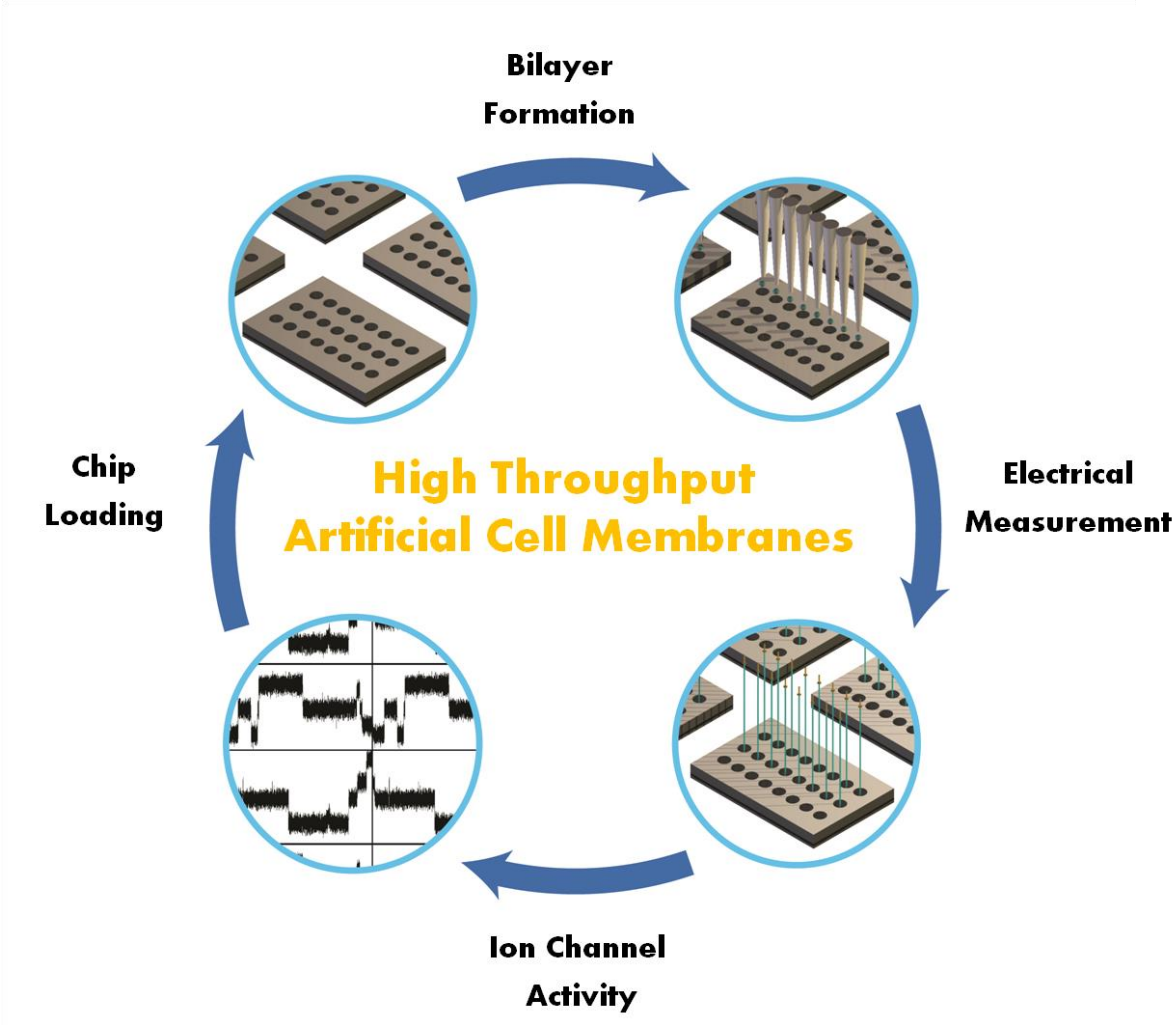

Figure 10. Cycling of the high throughput artificial cell membrane system. Steps include:

loading solutions to the chips, forming bilayers, conducting electrical measurements and recycling the process.

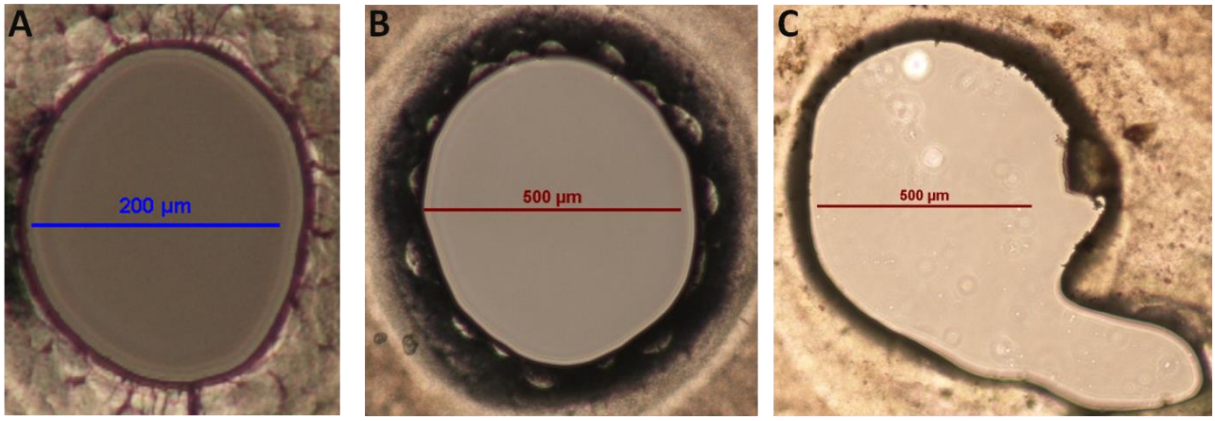

Figure 11. Microscopic images of partitions of different size or shape. (A) The size of the partition is about 200 µm in diameter and it is of good shape. (B) The size of the partition is about 500 µm in diameter and it is also of good shape. (C) The shape of the partition is abnormal and it is not used for chip assembly.

2.2 Materials and methods

2.2.1 Chip design and fabrication

The basic chip design (Figure 9A), which is similar to previous work[53,101], was created in Rhinoceros (McNeel) and illustrator (Adobe). Briefly, a 75 µm thick Delrin partition (McMaster-Carr) containing a central aperture 200-1000 µm in diameter and two outer circular openings collinear with the aperture was sandwiched between a 1/4" thick cast acrylic sheet (McMaster-Carr) and a 1/16" thick acrylic sheet (Figure 9A). The top sheet contained three collinear circular openings centered on corresponding features in the Delrin. The bottom piece had a slot cut in it so that the three openings were connected below the Delrin film following assembly of the chip. Below the bottom piece another acrylic sheet was attached to seal the slot. This basic design was

repeated eight times to form an array (Figure 9F), which itself was repeated four times (Figure 9I). The openings and slots in the acrylic sheets, as well as the apertures of different sizes in the delrin films, were laser cut (VersaLaser). The partition size was measured under microscope (Nikon). Only the partitions of good shape (Figure 11 AB) were used to assemble a chip for bilayer formation. The chip was assembled using VHB foam tape (McMaster-Carr). After assembly, 500 µl of decane (Sigma-Aldrich) was loaded to side wells of each unit of the chip and the entire chip with decane was left on the bench for about 30 mins. Then the chip was washed with methanol three times, followed by three washes with water. At last, the chip was dried under argon and stored in a desiccator for later use.

2.2.2 Solution preparation

Liposome solutions were made as described previously[15]. Briefly, 10 mg of lipids (Unless mentioned otherwise, the lipid was usually 2-diphytanoyl-sn-glycerol-3-phosphocholine (DPhPC) (Avanti Polar Lipids)) in chloroform was dehydrated under argon then rehydrated in 1 ml buffer B (1 M KCl, 10 mM HEPES, pH 8.0). The solution was then extruded through a 200 nm filter (Avanti Polar Lipids) to form 200 nm diameter liposomes. In all liposome experiments, the lipid concentration was 250 µg/ml. Lipid in oil solutions were made by dissolving 10 mg of DPhPC into 1 ml of squalene:decane (2:1 v:v) (Sigma-Aldrich). Gramicidin A (Sigma) was dissolved in ethanol at 1 mg/ml and used in bilayer experiments mixed with Buffer B at 20 ng/ml; α-hemolysin (Sigma) was prepared in buffer B at 0.5 µg/ml. In experiments measuring gramicidin and α-hemolysin, these channel-containing solutions were used as the aqueous solutions for bilayer formation.

2.2.3 Bilayer formation

Lipid bilayers were formed as shown in Figure 9B-9E. When liposomes were present in the

aqueous buffer, 400 µl of liposome solution was added to each of the outer wells of the chip, filling the lower channel, followed by addition of 50 µl decane:squalene to the central well. After waiting 5 minutes for monolayer formation, 50 µl of liposome solution was added to the central well for bilayer formation[12]and electrodes were placed into the aqueous solutions in the central and outer well for electrical measurement (described below). Finally, an additional 150 µl of liposome solution was added to the outer well.

When bilayers were formed using lipids present in the decane:squalene, 400 µl of buffer was added to the outer well, followed by 25 µl of lipid/decane:squalene solution was added to the central well. After waiting for 40 minutes, 50 µl of buffer was added to the central well. Electrodes were then placed into the aqueous solutions in the central and outer well and an additional 150 µl of buffer was added to the bottom well.

In some experiments, 1% agarose[98,102–104] (Sigma-Aldrich) (mass/volume ratio) was also used to stabilize the sizes of bilayers. Briefly, 1% agarose was prepared in buffer and then boiled. Before the solution solidified, it was loaded to the bottom wells of the chip. After the solution gelled, lipid oil solution and other solutions were added as described above.

2.2.4 Apparatus for multiple bilayer formation and measurement

An 8-channel electrode array (Figure 9G) was made by connecting bleached silver wires (CC Silver and Gold, SFW22a) to a customized printed circuit board (PCB, ExpressPCB), which was designed to fit the electrode pairs at a spacing that matched the 8-well chip. The PCB contained female sockets (Newark, 86C2226) into which male sockets (Newark, 87H9360) soldered to the silver wires could be inserted and removed, allowing easy replacement and conditioning of the electrodes (Figure 9H). The PCB routed electrical connections from the electrode pairs to a connector (Terrapin, Tecella Inc.) soldered on the edge of the board which connected to the

amplifier through a cable.

A rectangular plate made out of acrylic was used to hold the electrode and chip arrays (Figure 9I). There were four slots and four posts containing alignment blocks glued to the plate bottom. These elements formed cavities matching the chip arrays and PCBs precisely, allowing the plates and electrodes to be rapidly positioned and aligned without adjustment.

To make and measure bilayers in 32 wells simultaneously, four 8-well chips were placed into the slots. After adding oil to the central wells, the four electrode PCBs were placed onto the posts between the blocks. The height of the posts, the location of the slots and the blocks and the length of the electrodes were designed so that with the chips and fluidic volumes used, electrical connection between the electrodes and aqueous solutions occurred 100% of the time.

For measurements of single bilayers, an Axopatch 200B with a Digidata 1440A (Axon Instruments) was used. Measurements of multiple bilayer measurements used a multichannel amplifier (Apollo, Tecella Inc.). Bilayer formation was monitored capacitively[7].

2.3 Results and discussion

2.3.1 Bilayer formation

Bilayers were successfully formed and measured following simple solution dispensation with the lipid source present in either the oil or aqueous solution. Following addition of 400 µl of the lower aqueous solution and 50 µl of decane to the central well, no further solutions were added during the lipid monolayer formation time, conservatively 5 minutes when liposomes were present in the aqueous phases and 40 minutes when the lipid was in decane:squalene. When this waiting time was not observed, the subsequent addition of 50 µl of the aqueous solution to the central well sometimes resulted in fusion of the upper and lower aqueous solutions. However, with the waiting time, the upper aqueous solution was stably separated from the lower aqueous

solution (Figure 9B-9E). This was observed electrically using measurement electrodes in the outer and center wells; the fused solutions showed a very low resistance between the electrodes whereas the separated aqueous solutions showed high resistance (> 50 GΩ). The initial measured capacitance was about 40 pF, a background value from which increases indicated bilayer formation. To verify that the increase in measured capacitance corresponded with bilayer formation, α-Hemolysin or gramicidin A were added into the buffer in some experiments; pores were observed (Figure 12A-B) when the capacitance exceeded 40 pF.

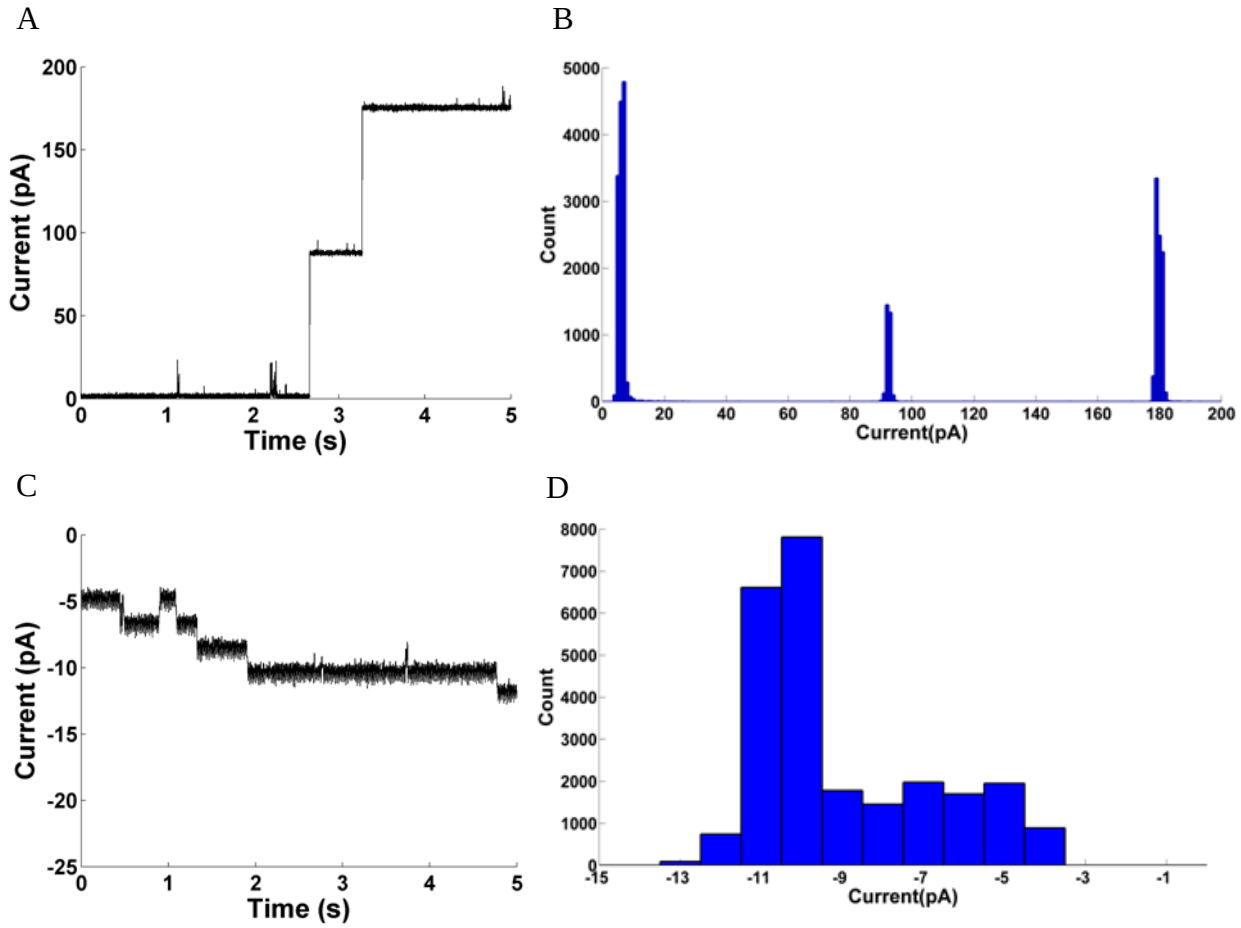

Figure 12. Ion channel recordings. Single channels of α-Hemolysin (A) and gramicidin A (C) measured in a single well. (B) and (D), histogram analysis of the single channels. Applied

voltage was 100 mV in (A) and -100 mV in (B).

The capacitance usually did not change from the background values unless the final 150 µl of the aqueous solution was added to the outer well. The separate addition of the 400 µl and 150 µl solutions to the outer well was necessary; if 550 µl was initially added to the outer well, the lower and upper aqueous phases usually fused following addition of the 50 µl aqueous solution to the central well. We hypothesize that when the final 150 µl of solution is added to the outer well, the curvature of the lower lipid monolayer decreases as a result of the increase in pressure according to the Young-Laplace equation, $P = \frac{2\gamma}{R}$, where P is the pressure difference across the lipid monolayer, γ is the monolayer surface tension, and R is the radius of curvature[105]. This decrease in curvature raises the center of the lower monolayer, bringing it into contact with the upper monolayer for bilayer formation. The time it took to bring the two monolayers together varied, but generally ~10 minutes was required for maximum yield when the lipid was in aqueous solution and 30 minutes when lipid was in decane:squalene (Figure 13). This hypothesis is additionally supported by observations that the solution volumes resulting in successful and stable bilayer formation changed with aperture size.

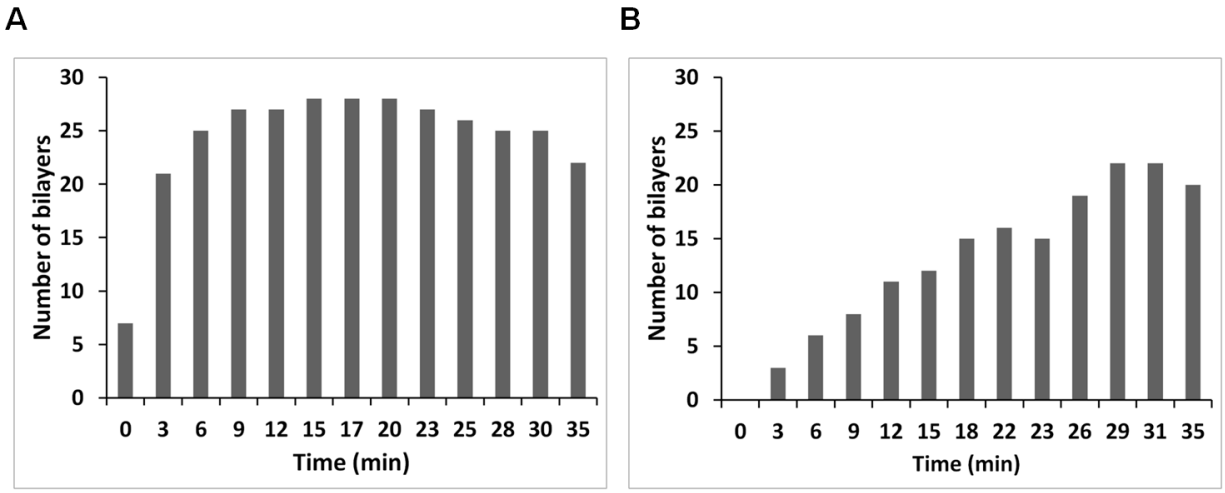

Figure 13. Number of bilayers as a function of time in both (a) liposome and (b) lipid in oil methods. In liposome method, 32 wells were done at a time. In lipid in oil method, 31 wells were done at a time. In both methods, the time was set to zero after all the solutions were added.

2.3.2 Screening of the aperture size

To screen aperture sizes that provided the greatest yield, we measured capacitance and bilayer formation over 15 wells simultaneously. As described above, we observed that apertures of different sizes required different volumes of added solutions to facilitate bilayer formation. To simplify the screening measurement, a fixed 550 µl solution volume was used for all aperture sizes.

Due to variations in the laser cut aperture sizes, the aperture diameters were measured microscopically and each size was averaged. For lipid present in the aqueous solution, the average aperture diameters tested were 318 ± 23 µm (n = 15), 398 ± 35 µm (n = 15), 596 ± 21 µm (n = 15) and 829 ± 49 µm (n = 15). Bilayer formation and measurement proceeded as described above, and 10 minutes following the addition of the final 150 µl to the outer well, the capacitance and resistance were noted. If the resistance was small (< 1 GΩ), the result was categorized as a fusion of the aqueous phases. If the resistance was large but the capacitance stayed at a background value (< 40 pF), the result was categorized as an unformed bilayer. Finally, for high resistance and a capacitance greater than background value, the result was categorized as successful bilayer formation. As shown in Figures 14A, apertures of 400-600 µm in diameter resulted in a bilayer yield ~80% at 10 minutes following the final solution addition. This yield was lower for the smaller aperture size, with the bulk of the non-bilayer measurements being background events, whereas for large aperture size, the lower yield resulted from an increase in bilayer failure or fusion of the aqueous phases.

This experiment was repeated for lipid present in decane; in general, we found that when the lipid was present in decane, larger apertures were required to result in bilayer formation compared to measurements in which the lipid was present in aqueous solution for the same solution and chip volumes. Owing to the long bilayer formation time, the bilayer yield was assessed 30 minutes following final addition of solution to the central well. The general trends observed previously were seen again (Figure 14B), but for larger average aperture diameters (596 ± 21 μm (n=15), 680 ± 27 μm (n=15), 795 ± 22 μm (n=15) and 1032 ± 41 μm (n=15)). The maximum yield of 73% occurred with 795 μm diameter apertures. Again, there were more background events for smaller apertures and more fusion events for bigger apertures.

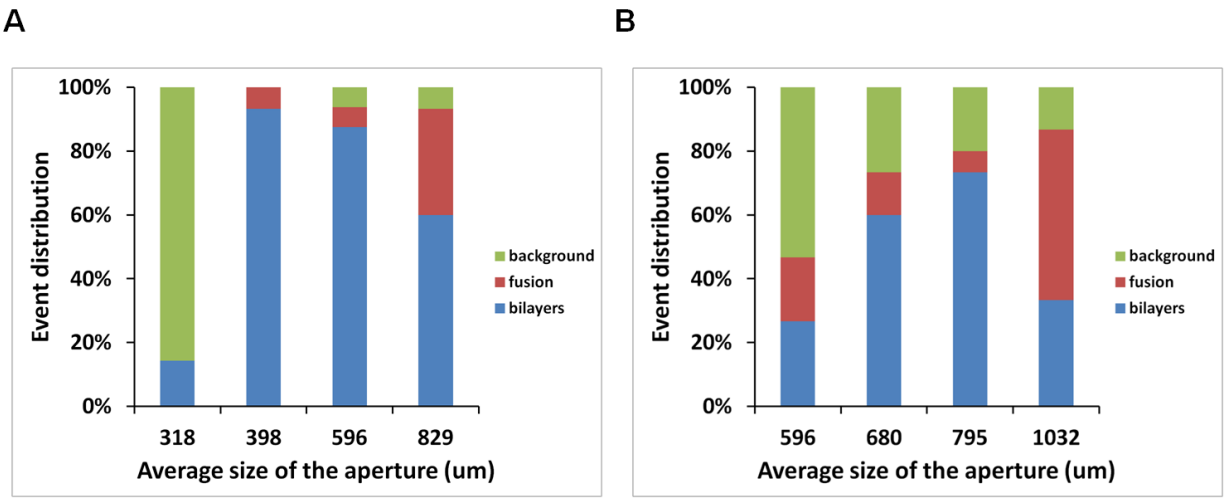

Figure 14. Yield of bilayer formation as a function of aperture size in both (a) liposome and (b) lipid in oil methods. In liposome method, the maximum yield for each aperture was counted 10 minutes after all the solutions were added. In lipid in oil method, the maximum yield was counted 30 minutes after all the solutions were added. This experiment was repeated twice more, with similar results. Similar experiments to those shown in were repeated for two more times and similar trends were observed: apertures of 400-600 μm in diameter resulted in a bilayer yield ~80% in liposome method; the maximum yield occurred with 795 μm diameter

apertures in lipid oil method.

In addition, we noticed that the volumes of solutions that resulted in successful and stable bilayer formation changed with aperture size. Specifically, for aperture diameters < 200 µm, > 550 µl of lower aqueous solution was required to increase the measured capacitance past the 40 pF background value. For aperture diameters > 600 µm, < 550 µl was required; for greater volumes, the aqueous solutions were observed to fuse. Since the same chips (apart from aperture size) were used in all experiments, increases in volume of lower aqueous solution resulted in larger heights of the fluid column in the outer wells. Since the volume and therefore height of the solutions in the center well remained unchanged, there was a hydrostatic pressure difference at the aperture, which formed the boundary of the aqueous and oil phases. As the pressure difference increases, the Laplace pressure would cause this interface to curve upwards. This would bring the lower interface closer to the upper interface, enhancing bilayer formation. For small apertures, the same curvatures result in a lower vertical increase of the lower interface, explaining why we needed more fluid to obtain bilayers in that case. For large apertures, the large vertical increase of the lower interface readily resulted in formation of large bilayers which were less able to sustain the pressure difference. This was similar to our previous work exploring bilayer area and stability as a function of hydrostatic pressure[105].

2.3.3 Parallel bilayer formation and ion channel measurement

In the previously described experiments, bilayers were formed easily and in high yield following fluid dispensation with no other operator intervention, aside from coarse placement of the electrodes in the center and outer wells. As a result, this is highly amenable to parallelization

and automation. To explore this, we created an apparatus for parallel bilayer formation and measurement in multiple wells (Figure 9I). The bilayer array chips were made with aperture diameters previously identified with highest yields (400-600 µm for aqueous lipid and 800 µm for lipid in decane:squalene). The apparatus allows simultaneous formation of 32 bilayers in parallel and measurement using a Tecella multichannel amplifier. Solutions were added to each chip using an 8 channel pipette. Bilayer formation was again monitored through resistance and capacitance measurements. For lipid present in the aqueous solution, bilayers formed in 27 of 32 wells (84%) after 10 minutes, with a simultaneous yield >80% at 20 minutes and >70% at 30 minutes. For lipid in decane:squalene, yield was >50% after 22 minutes and >70% after 29 minutes. In terms of overall yield, lipid in aqueous solution was slightly superior to lipid in decane:squalene.

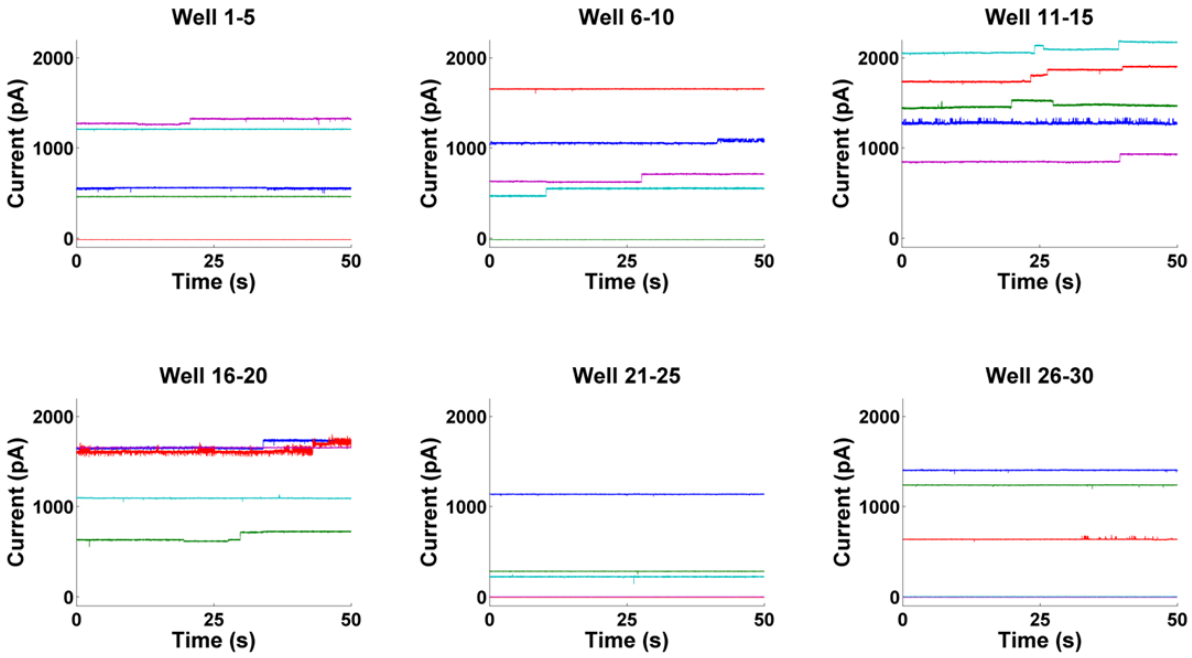

Figure 15. Ion channel recordings. Simultaneous recordings from 30 wells in which α-Hemolysin was present in the surrounding solution. Traces shown are 20 minutes following final

solution addition (100 mV applied).

Next, formation of bilayers from aqueous lipid in the presence of α-Hemolysin was measured in 30 wells simultaneously. Similar to the previously described experiments, stepwise increases in conductance resulting from α-Hemolysin insertions were observed following bilayer formation. These steps were observed to continue and therefore the measured current increased with increasing time from bilayer formation. Figure 15 shows conductance measurements 20 minutes following final solution addition; α-Hemolysin steps were seen in 24 out of 30 wells simultaneously (80%), with bilayer failure (fusion of aqueous solutions) in the remaining wells. Repetition of this experiment was consistent, finding successful α-Hemolysin measurement in 26 out of 32 wells and 25 out of 30 wells, with the bilayers in the remaining wells rupturing. The number of α-Hemolysin pores in each membrane varied, a consequence of the variable bilayer area (14000 – 38000 μm^2 (measured capacitively), variable time of bilayer formation (2-10 minutes following final solution addition), and stochastic insertion of the pores in each membrane[16,106].

2.3.4 Cycled, parallel bilayer formation and measurement

Bilayer arrays have been described previously[18,21,96,97,99,100,107,108]; these arrays can increase efficiency by increasing the number of bilayers measured simultaneously, but to increase measurement throughput further, the array density must increase or the apparatus must be partially disassembled and prepared for another measurement cycle. Our apparatus was designed to decrease the effort and time required to cycle through repeated measurement of the arrays. To demonstrate this, we repeated the preparation of the chips for simultaneous formation and

measurement of 30 bilayers with lipid in aqueous solution, cycling the apparatus four times. In one experiment, 30 bilayers were simultaneously formed and measured in parallel, measured for 10 minutes, discarded, and 30 new bilayers were freshly formed and measured, repeating this process four times sequentially for 120 total possible bilayers. While the electrical measurements were being carried out on one set of chips, the next set of chips were prepared by adding aqueous lipid solution to the outer well and the decane:squalene to the central well. When the next set of chips was to be measured, they were put in place and the central aqueous and final lower aqueous solutions were added to the chips, following which the monolayer formation time was observed. Aside from the 10 minute measurement time, approximately 10 minutes for solution loading and monolayer formation was also needed for each set, bringing the total process time to approximately 20 minutes per set. Bilayer formation was indicated once the capacitance exceeded 40 pF.

As shown in Table 1, 96 bilayers were formed in 120 wells, an average yield of 80%, with a total time of 79 minutes to process four 30-well sets sequentially. Although in this experiment ion channels were not utilized, we saw similar bilayer yield with ion channels measured in the previous experiment (Figure 15). This yield is comparable to yields of 46%-56% in previous reports of bilayer arrays with integrated electrodes.[18, 28, 40] The throughput of this experiment could be easily increased with automated fluid handling, greater parallelization, shorter measurement time, or switching between two sets of measurement electrodes, which could effectively eliminate any non-measurement time.

Table 1. Statistics of cycled bilayer formation in 4 sets of 30 attempts each

Batch	1	2	3	4	Total	Total time
Yield	24/30	25/30	24/30	23/30	96/120	79 min

2.3.5 Stabilize bilayer size with agarose

One problem with the previously described bilayers was that the size of bilayers usually increased over time (Figure 16 A-B). To address this issue, we used agarose at the bottom to support the bilayer formation. Our results showed that agarose significantly stabilized bilayer size (Figure 16 C-F). The existence of bilayers was validated by the occurrence of Gramicidin-A and alamethicin activities (Figure 17). The yield of bilayer formation was 87.5%, or 28/32, which was comparable with the method without the use of agarose. Out of 28 bilayers, 24 bilayers did not show significant increase in size, whereas all of the 26 bilayers out of 32 wells showed size increase when there was no agarose used. The size variance of bilayers with agarose support was also much smaller than that without agarose. We think this was due to the fact that the vertical position of the bilayers could not be changed once the agarose solution at the bottom solidified.

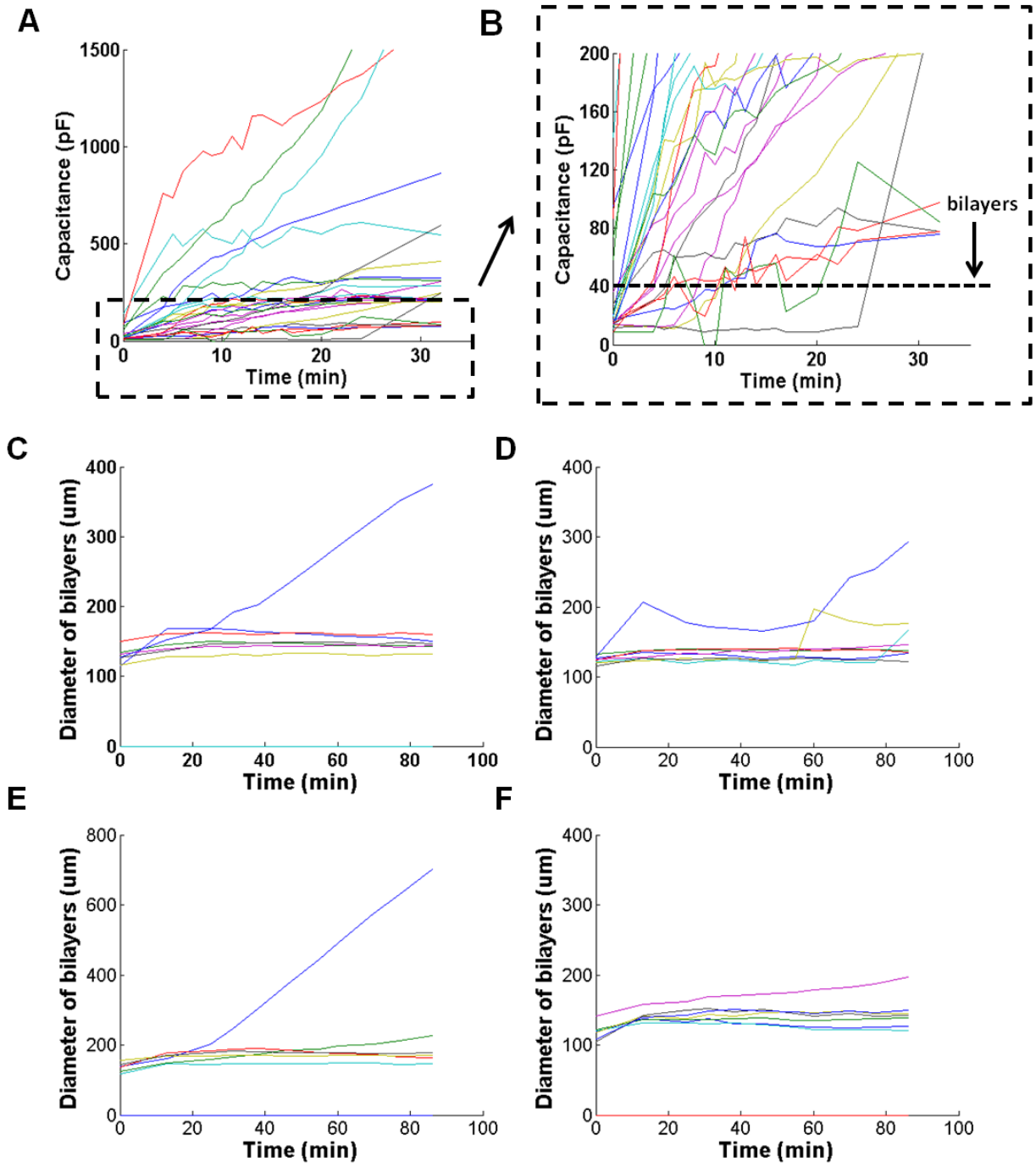

Figure 16. The change of bilayer size with/without the use of agarose. (A-B) Without the use of agarose, bilayer sizes of 32 bilayers were shown as a function of time. The bilayer size increased for most of the bilayers over time and more than half of the bilayers showed rapid increase in size within 10 minutes after bilayer formation. (C-F) The change of the sizes of 32 bilayers with

agarose support. The size did not change too much over time for most of the bilayers and the bilayer sizes were similar to each other.

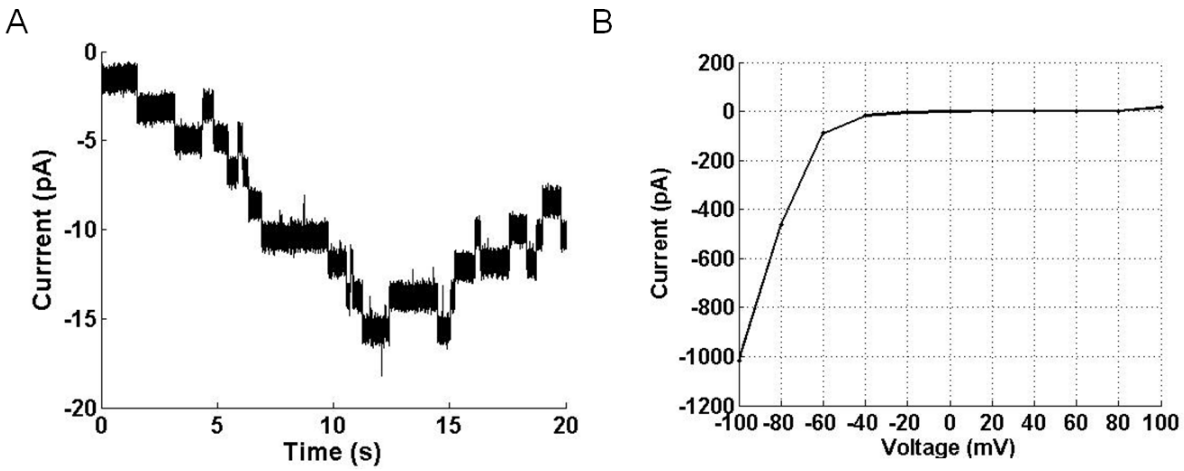

Figure 17. Ion channel recordings of Gramicidin-A (A) and alamethicin (B) in bilayers supported by agarose. For Gramicidin-A, the applied voltage was -100 mV. For alamethicin, a series of voltages from -100 mV to 100 mV with 20 mV increment were applied.

2.4 Conclusion

We present a very simple and user friendly platform for parallel formation and measurement of artificial lipid bilayers with highly repeatable yield of 80% in initial studies. The design of the apparatus enabled quick and accurate alignment of the electrode arrays with the wells so that electrical connection was guaranteed with minimal positioning precision required. More importantly, the design minimized time, effort, and training or expertise required for bilayer formation and ion channel measurement, potentially opening artificial bilayer measurements to a wider audience. Since each part is set, all that is required from the user is to place the chips and electrode arrays in position. The electrodes were also easily removable and replaceable from the PCBs for easy maintenance. The platform is highly automatable and scalable; if scaled for high

throughput operation, the platform may have potential for application to ion channel drug screening, nanopore-based DNA sequencing and nanoparticle-membrane study.

Chapter 3

3. Validation of the lipid bilayer array platform for nanoparticle study with amine or carboxyl modified polystyrene nanoparticles

3.1 Introduction

Nanoparticles have attracted much attention because of their wide applications and existence. In biomedical applications[109], nanoparticles are used for drug delivery[110], therapeutics[111], diagnostics[112], and imaging[113].There are also nanoparticles used in many other applications, such as paints[114], sports equipment, sunscreens, cosmetics, cooking products and wound dressings[115]. Besides those applications, nanoparticles are also present in the environment resulted from both natural and anthropogenic activities[116] including forest fires[117], volcanoes[118], desktop 3-D printers[119], and vehicle and airplane engine exhaust[120]. As more and more nanoparticles are used and discovered, there are raising concerns regarding the impact of nanoparticles on human health[116]. Therefore, many in vitro and in vivo assays are conducted to assess the cytotoxicity of nanoparticles by exploring if and how nanoparticles affect cell viability and cellular processes including DNA synthesis, gene expression, immune response, and oxidative stress[121,122]. One aspect of the toxicity assessment is to examine the impact of nanoparticle on cell membranes, especially the likelihood of nanoparticles to damage the membranes[94].

Up to date, there are a number of techniques used in the nanoparticle-membrane interaction study. Through hemolysis or patch clamp[123–125], it is easy to determine if a nanoparticle could rupture cell membranes. However, because of the use of live cells both techniques do not have too much freedom of changing conditions such as lipid type, ionic strength, and pH for further probing of the mechanism of interaction. As such, artificial cell membranes combined with

AFM[92–94], fluorescence imaging[126,127], neutron reflectometry[128], FRET[129], or electrical measurement[88–91,130] are utilized to investigate how nanoparticles interact with lipid bilayers under different conditions. Despite the significant amount of information regarding the mechanism of nanoparticle-membrane interaction provided by those methods, their applications are limited by the low speed and low throughput. Also, there are questions remaining such as the mechanism by which some positively charged nanoparticles induced lysosomal membrane damage[131] and how nanoparticles interact with membranes under different physiological conditions, especially with artificial membrane systems. Therefore, there is a need to use a fast and high throughput lipid bilayer platform to investigate nanoparticle-membrane interaction in many different conditions in depth.

In this study, we demonstrated the use of a parallel lipid bilayer array platform[132] for the study of nanoparticle-membrane interaction. Amine modified polystyrene nanoparticles (NH_2-NP) and carboxyl modified polystyrene nanoparticles (COOH-NP) were chosen as model particles to test our platform. Plasma membranes and lysosomal membranes were mimicked based on their lipid compositions and surrounding environment in mammalian cells. The effect of NH_2-NP or COOH-NP on membranes was compared in different conditions. Factors like particle concentration, ionic strength, bilayer charge, pH, and serum were investigated as to how they regulate nanoparticle-membrane interaction. Extra efforts were also focused on how NH_2-NP breaks lysosomal membranes by looking at the biophysical behaviors in interaction. To the best of our knowledge, it was the first time that we mimicked the mammalian plasma and lysosomal membranes with more than 90% similarity to study nanoparticle-bilayer interaction. It was also the first time that nanoparticle-membrane interaction was studied in lipid bilayer array system and that the results were derived collectively from statistical analysis of more than 1000 bilayers.

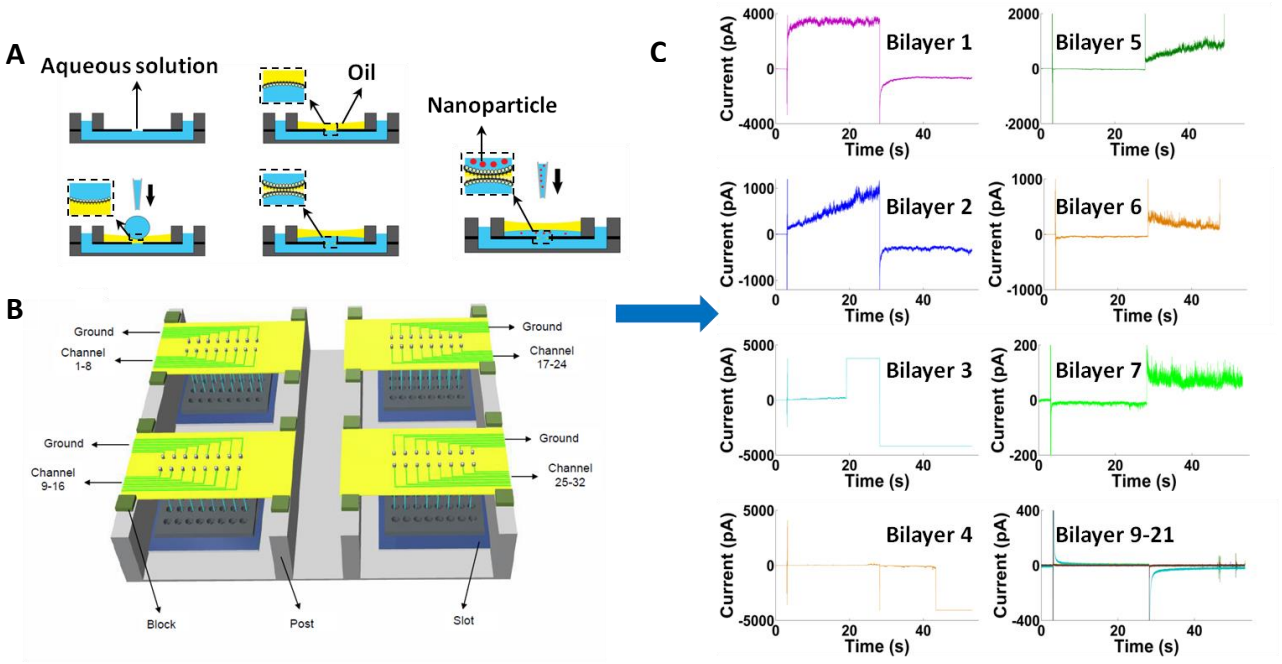

Figure 18. Schematics of bilayer formation, nanoparticle measurement, and measurement display. (A-D) Bilayer formation: (A) To form bilayers, aqueous solution is first added to the bottom channel through the outer wells. Oil is then added to the central well for lipid monolayer formation (inset) at the aqueous/organic interface, constrained by the masking aperture. Aqueous solution is then added to the central well to form another lipid monolayer (inset). Finally, bilayer formation begins (inset) after adding additional lower aqueous solution through the outer well. Nanoparticles were added to the central well after bilayer formation. (B) Apparatus schematic for simultaneous bilayer formation and measurement in 32 wells. (C) A typical display of simultaneous current recordings of multiple bilayers. Bilayer 1-7: currents induced by 100 µg/ml NH_2-NP. Bilayer 9-21: half of the bilayers were tested with 100 µg/ml COOH-NP, and the other half with control buffer. There were 11 other bilayers which were not of high quality for use. Voltage protocol: for bilayer 1-4 and 9-21, 0 mV was applied for 3 s, followed by 70 mV for 25s

and then -70 mV for 25 s; for bilayer 5-7, 0 mV was followed by -70 mV for 25 s and then 70 mV for 25 s. Bilayer composition: POPC/POPE/Chol/ POPS CB/BMP (3:3:3:1:2:2, molar ratio). Buffer: 80 mM NaCl, pH 4.5.

3.2 Materials and methods

3.2.1 Nanoparticle characterization

Amine polystyrene nanoparticles (NH_2-NPs) and carboxyl polystyrene nanoparticles (COOH-NPs) (Bang's Laboratory) were gifts from Tian Xia's lab at UCLA. The size of the particles and the zeta potential were measured with Zetasizer (Malvern).

3.2.2 Solution preparation, chip fabrication and bilayer array formation

Liposomes and lipid in oil solutions were prepared as described previously[132]. Usually one of or a combination of some of the following lipids was used to make liposomes and lipid oil solutions depending on the goal of the experiments: 1-palmitoyl-2-oleoyl-sn-glycero-3-phosphocholine (POPC), 1-palmitoyl-2-oleoyl-sn-glycero-3-phosphoethanolamine (POPE), Cholesterol (Chol), 1-palmitoyl-2-oleoyl-sn-glycero-3-phospho-L-serine (POPS), Cerebroside (CB), sn-(3-oleoyl-2-hydroxy)-glycerol-1-phospho-sn-1'-(3'-oleoyl-2'-hydroxy)-glycerol (BMP), 1,2-diphytanoyl-sn-glycero-3-phosphocholine (DPhPC), and brain lipid extract (Avanti Polar Lipids). The molar ratio of the lipids was specified in the result session. For any given bilayers, the lipid composition for both liposomes and lipid oil solution was the same. The chips for bilayer formation were also fabricated as described previously[132].

As shown in Figure 18A-D, bilayers were made by following the protocol described in previous work [132] with slight modification. Briefly, bilayers were formed by adding 450ul of 250ug/ml liposome solution to the outer wells of the chip, followed by 25ul of 10mg/ml lipid

organic solution (decane) to the central well. After allowing 15 minutes for monolayer formation, 50ul of buffer solution without any lipid was added to the central well for bilayer formation and electrodes were placed into the aqueous solution in the central and outer wells for electrical measurement. After waiting an additional 15 minutes, 50~100 µl of liposome solution was added to each of the outer wells. To form bilayer arrays, two to four 8-well chips were used at a time (Figure 18F). The quality of bilayers was checked by applying 100/-100 mV for 10 minutes and the bilayers were considered good only if there was zero current passing the bilayers.

3.2.3 Electrical measurements of nanoparticle-bilayer interaction

The same measurement apparatus used in the previous work[132] was also used here as shown in Figure 18F. 5.5 µl of nanoparticle solutions (250 µg/ml~1 mg/ml) was added to the central wells with good bilayers (Figure 18E). The final concentration of the particles was in the range of 25 µg/ml to 100 µg/ml as specified in the result session. The particles were sonicated and vortexed to ensure full dispersion before use. At the same time, a control experiment in which 5.5 µl of buffer was added to the central wells was also conducted. Once the particles were added, a periodic voltage sweep composed of 70 mV for 25 seconds followed by -70 mV for another 25 seconds was applied to the bilayers and the conductance of the bilayers was monitored all the time for the next two hours unless the bilayers were ruptured earlier. There were multiple bilayers tested for each condition and the number was denoted as "n = #" in the result session.

3.2.4 Data analysis

The bilayer rupture percentage was calculated by dividing the total number of bilayers used by the number of bilayers ruptured. The difference in the bilayer rupture percentage between two

experimental groups was analyzed using two-tail Fisher's test. If the p value from the test for the two groups is less than 0.05, it is concluded that there is significant difference between the two groups, and vice versa.

The recorded data by Tecella was converted into text files and then transferred into Matlab (MathWorks) for analysis. A baseline was chosen at a value which equals to the sum of lowest current for a given trace and the peak-to-peak noise level. Any current above the baseline was noted as the opening of pores. A transient pore event was defined as a time interval between the first time the current is above the baseline and the immediate next time the current is below the baseline. A matlab script was written to pick out the opening events, the magnitude of the peak current for each event, and the duration of each event. The average pore size was calculated by modeling the pores as electrolyte-filled cylinders.

3.3 Results and discussion

3.3.1 Interaction of NH_2-NP or COOH-NP with bilayers of different lipid compositions

Nanoparticles first encounter cells through their plasma membranes[133]. We investigated the interaction between NH_2-NP or COOH-NP and the lipid combination POPC:POPE:Chol:POPS:CB (molar ratio 3:1:1:1:1), which represents more than 90% of the total lipids on the plasma membrane[134]. Bilayers of these lipids were formed and measured in buffered 150 mM NaCl (pH 7) and tested for stability for 10 minutes under alternating +70 mV/-70 mV potentials, following which NH_2-NP or COOH-NP were added to the central wells to a final concentration of 100 μg/ml. The trans-membrane current was measured for two hours during application of ±70 mV potentials, and currents resulting from bilayer pore formation or rupture indicated nanoparticle-bilayer interactions. Concurrently, control experiments in identical

conditions were performed without nanoparticles present in several wells in each membrane array chip.

Representative data from measurements of control, NH_2-NP, and COOH-NP with POPC:POPE:Chol:POPS:CB lipid bilayer membranes at in 150 mM NaCl (pH 7) is shown in Figure 19. Control experiments with no nanoparticles present and experiments with COOH-NP showed little to no current (Figure 19A). However, measurements with NH_2-NP showed large current fluctuations (Figure 19C) and membrane rupture (Figure 19B) indicating that the NH_2-NP interacted with membranes in these conditions quite strongly. Many measurements showed that interaction took place instantly (Figure 19B), while others showed a prolonged interaction (Figure 19C). For observations of prolonged interactions, the transmembrane currents were greater for positive versus negative applied potentials (Figure 19D). This dependence on the sign of the applied potential suggests that the positively charged NH_2-NP particles follow the electrical field, and more closely associate with the bilayer at positive potentials, increasing the magnitude of the interaction. This voltage dependence was also seen in the observations of instant rupture in that the ruptures were always observed when the membrane side on which the NH_2-NP were present was at a higher electrical potential relative to the particle-free side.

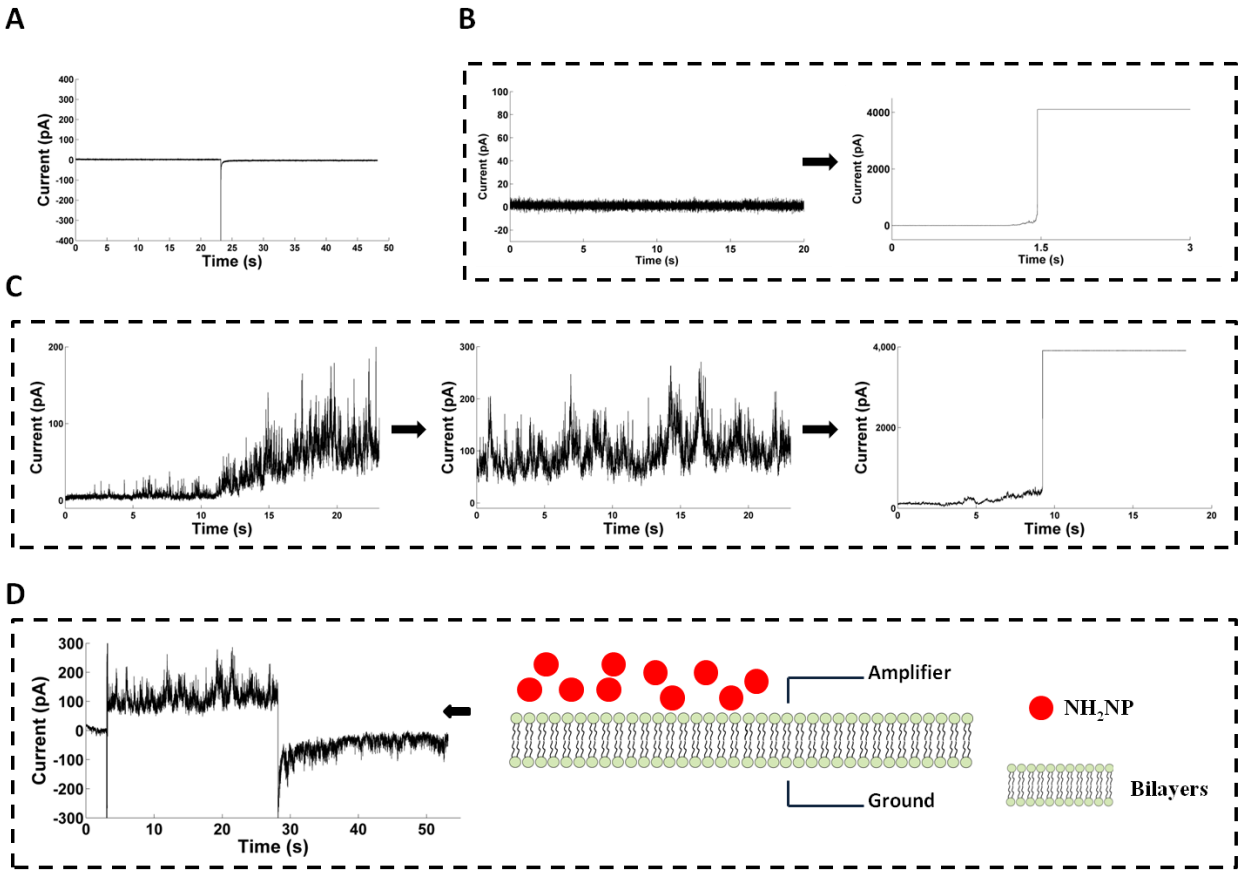

Figure 19. Electrophysiology recordings of particle-bilayer interactions. (A) Bilayers with either control buffer or COOH-NP were stable and did not pass any current under +70/-70 mV. The bilayers were monitored for 2 hours after adding control buffer or particles. (B) Instant bilayer rupture caused by NH_2NP. (C) Prolonged NH_2NP-bilayer interaction. The particles started to interact with bilayers by generating pores, and then more currents passed through the bilayers. Eventually bilayers were also ruptured. (D) Voltage dependence of NH_2NP-bilayer interaction. Bilayer composition: POPC/POPE/CHOL/POPS/CB (3:1:1:1:1, molar ratio); Buffer: 150 mM NaCl, pH 7; Particle concentration: 100 µg/ml.

These results were sustained over repeated experiments: COOH-NP did not interact with POPC:POPE:Chol:POPS:CB lipid bilayer membranes (N= 17) significantly different from the

control (N = 35), while NH_2-NP (N = 11) showed interactions significantly greater than the control (Figure 20). Other bilayer compositions (POPC/POPE/Chol/POPS, POPC/POPE/Chol/CB, DPhPC, and brain lipid extract) were also tested with NH_2-NP and COOH-NP in the same conditions (100 µg/ml in 150 mM NaCl at pH 7) with similar results: NH_2-NP exhibited interactions while COOH-NP did not significantly different from the control (Figure 20). Between 0-20% of control bilayers ruptured over the two hour measurement time, and with redundant measurement we assessed that the membranes exposed to NH_2-NP ruptured at a rate that was statistically significant compared to the control, while the COOH-NP results were statistically indistinguishable from the control.

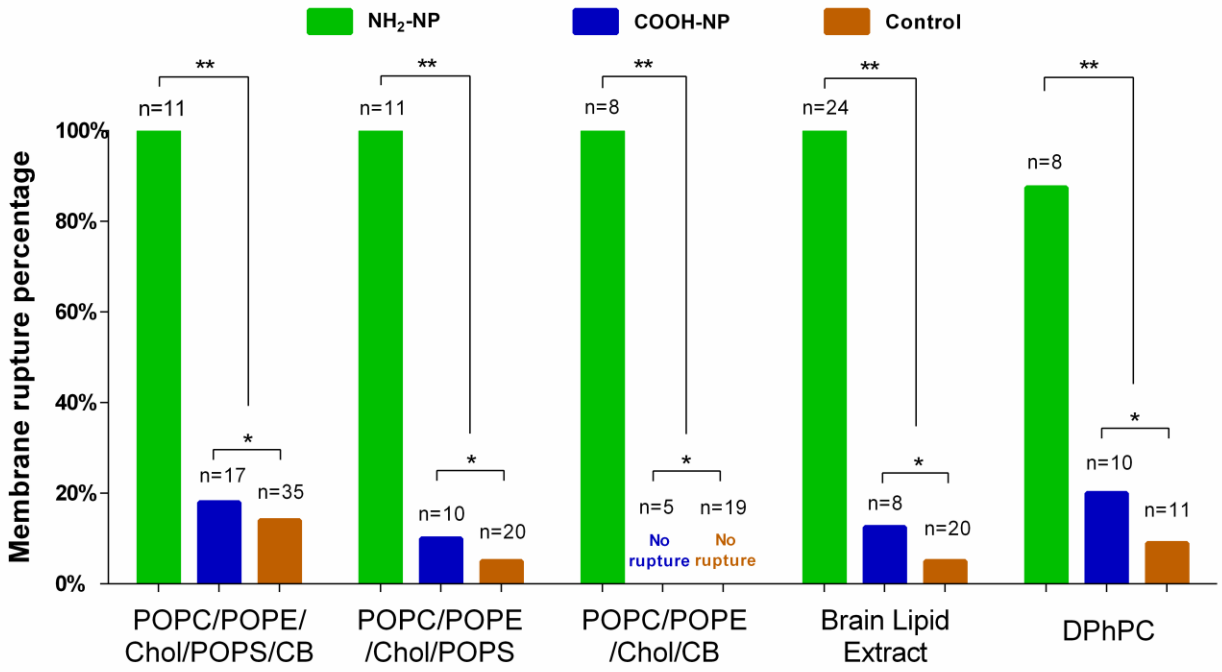

Figure 20. Interaction between NH2-NP or COOH-NP and different types of bilayers measured by the percentage of bilayers ruptured. The rupture percentage was counted as the ratio of the number of ruptured bilayers to the total amount of bilayers. NH2-NP interacted with all types of

bilayers with a rupture percentage of 100% for the bilayers made of POPC/POPE/Chol/POPS/CB, POPC/POPE/Chol/POPS, POPC/POPE/Chol /CB, or brain lipid extract and 87.5% for DPhPC bilayers. There was no difference between COOH-NP and control in terms of fusion percentage. Buffer: 150 mM NaCl, pH 7; Particle concentration: 100 μg/ml. The number of bilayers tried for each condition was denoted as "n=number". "*":Chi-squared test $P>0.05$; "**":Chi-squared test $P<0.05$.

These results are consistent with other groups' findings: Malmstadt's group showed that COOH-NP had weaker interaction with liposomes compared to NH_2-NP[126]; Granick's group showed that COOH-NP did not induce any shape change on liposomes whereas NH_2-NP induced tubular protrusions[127]; Negoda and coworkers found that COOH-NP are significantly less potent in inducing pores in lipid bilayers compared to NH_2-NP[90]

3.3.2 Effect of ionic strength, particle concentration, bilayer surface charge and pH

We also investigated the impact of ionic strength on NH_2NP interactions with POPC/POPE/Chol/POPS/CB (3:1:1:1:1) bilayers and found, consistent with the results from other groups[126,127], that the NH_2NP- membrane interaction decreased with increasing ionic strength (Figure 21A). With 25 μg/ml particle concentration, the percentage of ruptured bilayers decreased from 90% to 20% when the ionic strength increased from 5 mM to 150 mM. The high rate of bilayer rupture at 150 mM was restored from 20% to 100% by increasing the particle concentration from 25 μg/ml to 100 μg/ml. The time required for bilayer rupture was also much lower in lower ionic strength. For 25 μg/ml NH_2NP, in 5 mM 9 out of 10 bilayers ruptured, with an average membrane lifetime of 10 minutes. But in 150 mM only 2 out of 10 bilayers ruptured over two hours of observation, with an average lifetime of 103 minutes. This average time to

rupture in 150 mM decreased from 103 minutes with 25 μg/ml NH_2NP concentration to 13 minutes with 100 μg/ml NH_2NP. Similar results were also observed in measurements of NH_2NP with POPC/POPE/Chol/POPS bilayers (Figure 21B).

We also investigated the effect of membrane charge on NH_2NP interactions at 150 mM (pH 7) (Figure 21C). Three different bilayer compositions were compared: neutral (POPC/POPE/Chol/ CB (3:1:1:1), negatively charged (POPC/POPE/Chol/POPS/CB (3:1:1:1:1)), and positively charged (POPC/POPE/Chol/DOTAP (3:1:1:1)). NH_2-NP ruptured 100% of the neutral (N = 8) and negatively charged (N = 11) bilayers measured, but did not interact with positively charged membranes (N = 4). We also found that negative bilayer charge facilitated the interaction as it took less time on average for rupture of negatively charged bilayers (13 min) than neutral bilayers (47 min). The same positive, negative, and neutral bilayers were also tested with COOH-NP, but no interactions were observed different from control.

We also studied the effect of NH_2NP charge on membrane interaction by varying the solution pH in 150 mM NaCl. When the pH was at 4.5 or 7, NH_2-NP interacted with the bilayers by breaking the bilayers instantly. In contrast, when the pH was at 10, there was no NH_2NP-bilayer interaction (Figure 21D). We believed those interaction behaviors were caused by the change of the particle surface charge density on the particle as a result of the pH change. The zeta potential of the particles decreased from about 35 mV to 5 mV as increasing the starting pH from 7 to 10, which indicated that the density of positive charges decreased when increasing pH.

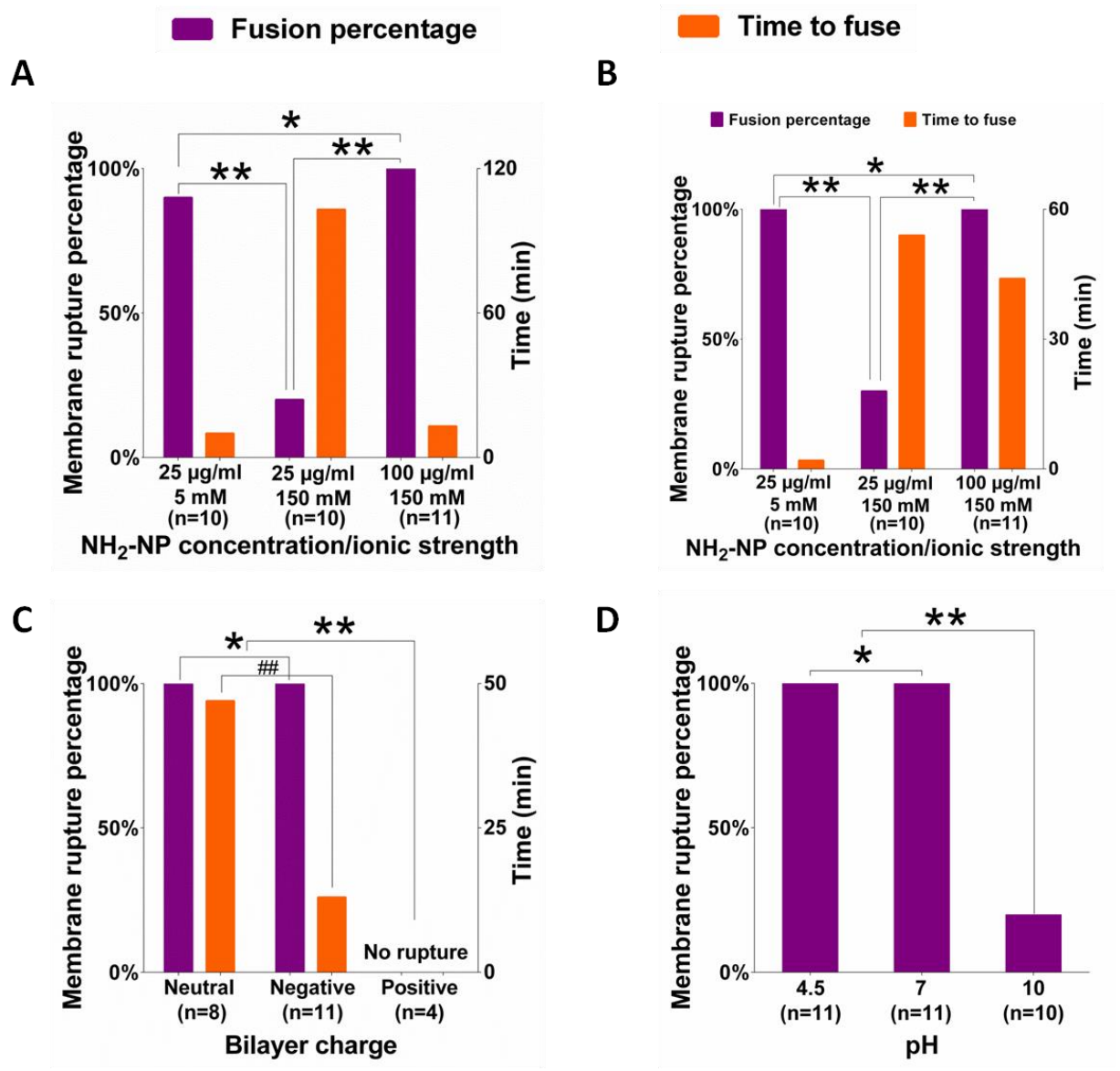

Figure 21. Impact of ionic strength, particle concentration, bilayer surface charge, and pH on NH_2NP-bilayer interaction. (A-B) Ionic strength and particle concentration. 25 µg/ml NH2-NP interacted with the bilayers in 5 mM NaCl with a rupture percentage of 90%. On average, it took 10 minutes for the bilayers to fail after the addition of the particles. For bilayers in 150 mM NaCl with the addition of 25 µg/ml NH_2NP, the rupture percentage was 20% and it took about 103 minutes. In 150 mM NaCl, 100 µg/ml NH2-NP fused 11/11 bilayers with an average time of 13

minutes. Bilayer composition: POPC/POPE/Chol/POPS/CB, 3:1:1:1:1, molar ratio; Buffer: pH 7 with different ionic strength. (B) Bilayer surface charge. NH2-NP interacted with both neutral and negative bilayers with a rupture percentage of 100%. On average, it took 47 minutes for NH2-NP to break the neutral bilayers and 13 minutes to break the negative bilayers. For the positive bilayers, NH2-NP did not show any effect. Buffer: 150 mM NaCl, pH 7; particle concentration: 100 μg/ml. (C) Effect of pH. NH2-NP interacted with bilayers made in pH 7 or pH 10, but not in pH 12. The pH indicated here was the starting pH of the solutions to which the particles were added. After addition of the particles, the pH decreased over time. Bilayer composition: POPC/POPE/Chol/POPS/CB, 3:1:1:1:1, molar ratio; Buffer: 150 mM NaCl with different pH; particle concentration: 100 μg/ml. The number of bilayers tried for each condition was denoted as "n=number". "*":Chi-squared test $P>0.05$; "**":Chi-squared test $P<0.05$; "##": student t-test $P<0.05$.

The modulation of the NH_2-NP membrane interaction with particle charge, membrane charge, polarity of applied voltage, and solution ionic strength is consistent with an electrostatic interaction. However, the lack of interactions observed of COOH-NP with all bilayers measured indicates an asymmetry between positive and negatively charged particles. This is consistent with the findings of Granick and coworkers that positively charged nanoparticles induce the zwitterionic phosphocholine (PC) lipid head group to bend, while negatively charged nanoparticles keep the PC head group straight and induce gelation in fluid bilayers[129]. Li and Malmstadt confirmed this result, also finding that the key interaction is between the cationic nanoparticle and the phosphate group of the lipid[126].

3.3.3 The presence of serum proteins attenuated the membrane activity of NH_2-NP

In physiological conditions, nanoparticles encounter cellular plasma membranes in an environment rich in serum proteins[133]. To investigate the effect of serum on particle-bilayer interactions, we repeated the previously described measurements of COOH-NP and NH_2-NP separately in 150 mM NaCl (pH 7), pure αMEM medium, and αMEM medium with 10% FBS. We did not observe any interactions with COOH-NP. For NH_2-NP, we observed 100% rupture in 150 mM NaCl (N =19) and pure αMEM medium (N =11), but no interactions in the presence of 10% FBS (N =9) (Figure 22A). We also observed that NH_2-NP aggregated when incubated with the medium with 10% FBS and that aggregation did not happen without 10% FBS (Figure 22B), indicating that the serum proteins bind to NH_2-NP, forming a protein corona, as observed previously[135,136]. This phenomenon was not observed for COOH-NP. Once the corona forms, NH_2-NP does not break cellular plasma membranes[137].

However, endocytotic capture and transfer to the proteolytic-rich environment of lysosomes[138] of serum-coated NH_2-NP can degrade the corona proteins and expose the particle surface[137]. To study the interaction of re-exposed nanoparticles with lysosomal membranes, we measured them with POPC/POPE/Chol/ POPS/CB/BMP (3:3:3:1:2:2, molar ratio) or POPC/POPE/Chol/CB (3:1:1:1,molar ratio) bilayers in serum-free 80 mM NaCl (pH 4.5) to mimic lysosomal membrane composition and solution pH[134,139]. Our experiments showed that NH_2-NP damaged the lysosomal membranes and that COOH-NP did not (Figure 22C), similar to results from Dawson and coworkers[131,137]. Similarly, we observed pore formation before bilayer rupture and voltage dependence of the interaction.

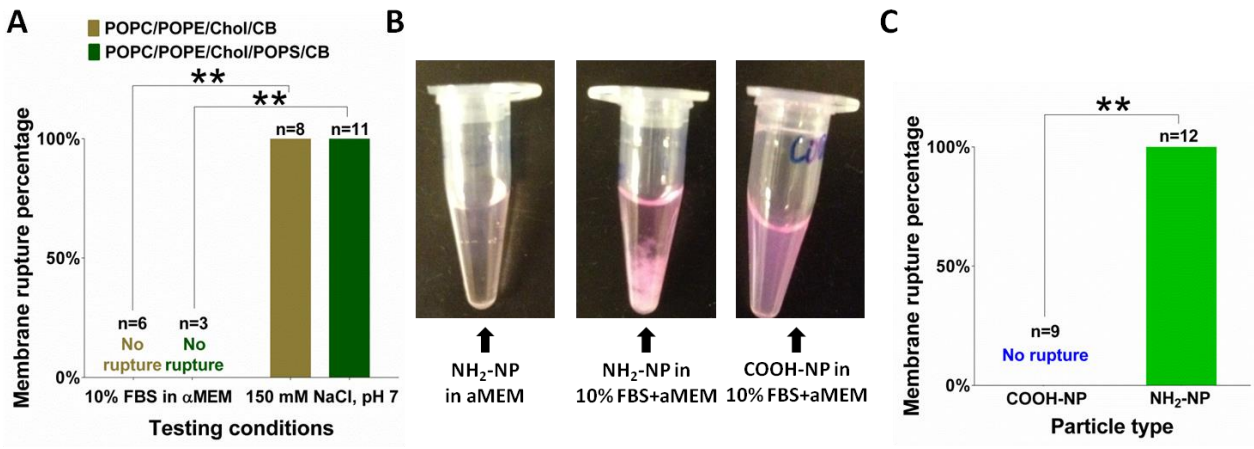

Figure 22. Impact of serum on NH_2NP-bilayer interaction (A and B) and interaction between NH_2-NP or COOH-NP and lysosomal membrane (C). (A) The effect of serum. NH_2-NP did not interacted with the membranes made in αMEM containing 10% FBS, but it did rupture bilayers made in the 150 mM NaCl buffer or pure αMEM medium. POPC/POPE/Chol/POPS/CB, 3:1:1:1:1, molar ratio. (B) Images of NH_2-NP or COOH-NP in pure αMEM medium or αMEM with 10% FBS. NH_2-NP precipitated in αMEM with 10% FBS, but not in pure αMEM. COOH-NP did not show any aggregation in either condition. (C) Interaction between NH_2-NP or COOH-NP and lysosomal membranes. NH_2-NP ruptured all 12 lysosomal membranes, whereas COOH-NP did not interact with the membranes at all. POPC/POPE/Chol/ POPS CB/BMP (3:3:3:1:2:2, molar ratio); Buffer: 80 mM NaCl, 5mM Tris-HCl, pH 4.5. Particle concentration: 100 μg/ml. The number of bilayers tried for each condition was denoted as "n=number". "*":Chi-squared test $P>0.05$; "**":Chi-squared test $P<0.05$.

3.3.4 Pore formation analysis

There have been questions about how NH_2-NP breaks lysosomal membranes[131]. In addition to qualitative analysis of NP-membrane interaction and rupture, we also examined pore formation in detail. In general, there were two types of pores observed: transient (Figure 23A-B & Figure

24 A-B) and persistent (Figure 23C & Figure 24C). The transient pores formed and then closed. In some experiments, the pores showed two different kinds of closing behaviors: gradual closure (Figure 23A & Figure 24A) and sharp closure (Figure 23B & Figure 24B). There were also transient pores when persistent pores were formed. Usually, the transient pores lead to either bilayer rupture or persistent pore formation followed by bilayer rupture. The small size and discrete step changes of the currents suggest the opening or closing of a single pore. The size of these single pores was estimated by modeling the pores as electrolyte-filled cylinders with radius 0.3-2.3 nm.

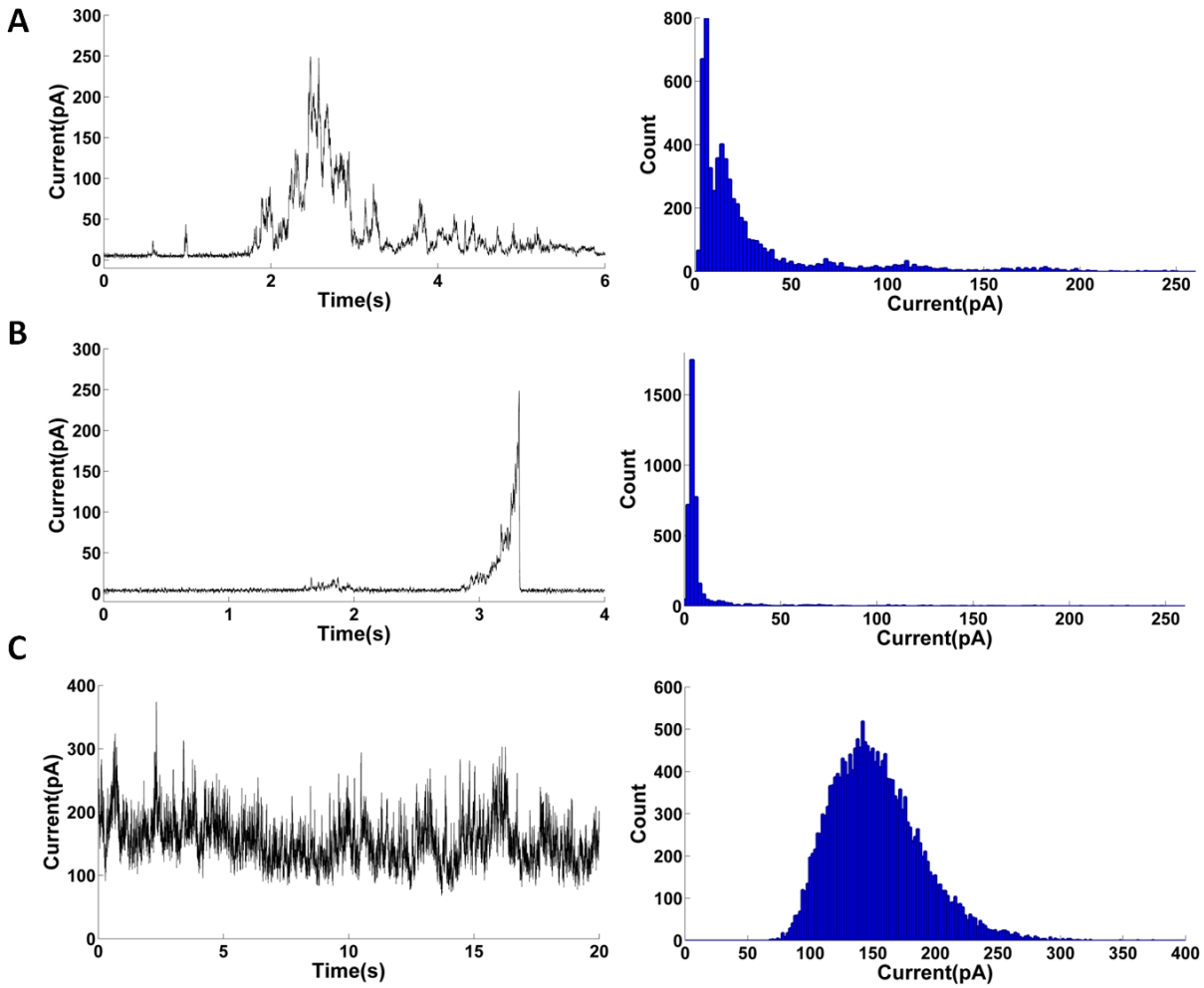

Figure 23. Representative traces of different pore formation and histogram analysis of the pores. (A) Transient pore formation with gradual closure and its histogram analysis. (B) Transient pore formation with sharp closure and its histogram analysis. (C) Persistent pore formation and its histogram analysis.

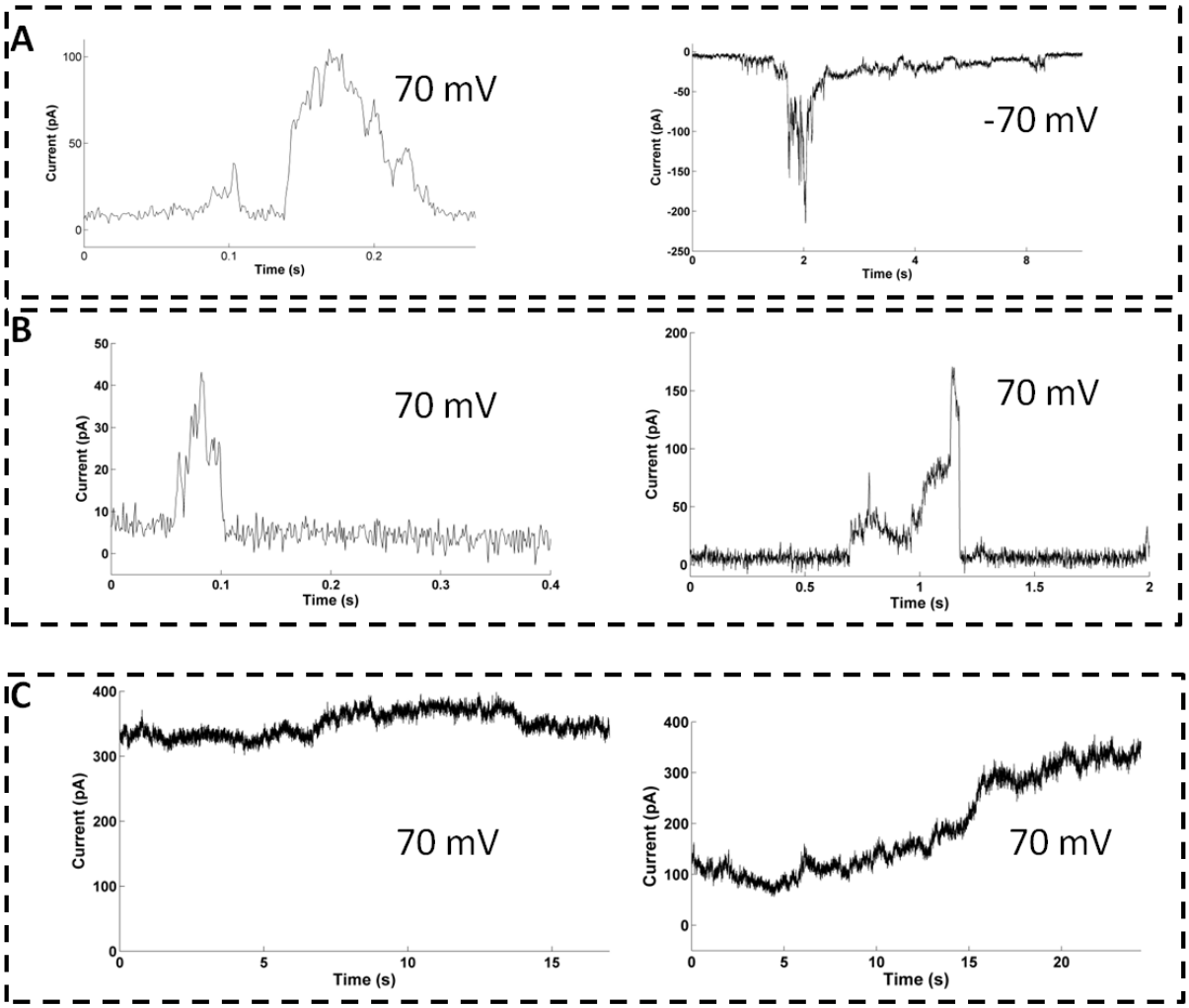

Figure 24. Pore formation analysis. (A) Transit pore formation with gradual pore closure. (B) Transit pore formation with sharp pore closure. (C) Persistent pore formation.

Table 2. Comparison of average pore size and open probability under different conditions

Factors	**Voltage (mV)**		**Bilayer charge**		**Voltage sign**		**Ionic strength (mM)**	
	20	70	Neutral	Negative	Positive	Negative	5	150
Pore diameter (nm)	0.45	0.42	0.29	0.42	0.52	0.38/0*	1.36	0.52
Open probability	51%	56%	70%	56%	58%	21%/0*	78%	58%

Note: * Under negative voltage, in some experiments there was pore formation, and in other experiments there was no pore formation.

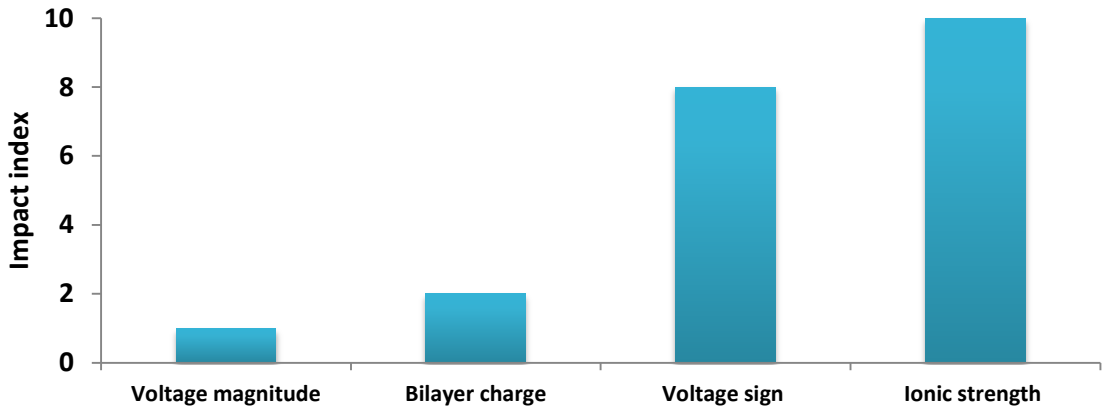

Figure 25. The impact of voltage magnitude, bilayer charge, voltage sign and ionic strength on the pore size. The impact is quantified by the impact index, with 1 being no impact and 10 being the strongest impact. Voltage magnitude in the range of 20-70 mV does not affect the pore size.

Bilayer charge affects the pore size a little with slightly bigger pores on negative bilayers. Voltage sign significantly poses impact on the pore formation. There is no pore formation or smaller pores under negative voltage compared to that under positive voltage. Ionic strength dramatically affects the size of the pores with pores at 5 mM being about 2 times bigger than that at 150mM.

The transient pores were also analyzed in depth to determine the impact of voltage magnitude, bilayer charge, voltage sign and ionic strength on the pore formation (Table 2). The four factors were quantified by the impact index to measure how they affected the pore formation (Figure 25). The magnitude of the voltage in the range of 20-70 mV did not affect either the pore size or its open probability, with the pore size and open probability of being 0.45 nm and 51% at 20 mV, respectively, and 0.42 nm and 56% at 70 mV (Figure 26). The slight difference in the pore size and open probability could be caused by the voltage offset on the electrodes, which was 3-5 mV.

The average radius of the pores on the negative bilayers seemed to be 1.4 times that on neutral bilayers (Figure 27). There were two possible causes. One explanation could be that the negative charge enhanced the particle-membrane interaction and ultimately generated bigger pores. The other could be that the concentration of cations in close proximity to the negative bilayers was higher than that to the neutral bilayers, which resulted in a higher conductivity and more currents passing the bilayers. In this scenario, the size of the pores may just stay the same as that with neutral bilayers.

In general, there were more activities at the positive voltage than that at the negative voltage. In the traces analyzed (Figure 28), the average pore size at the positive voltage was about 1.4 times that at the negative voltage. The percentage of total open time of all the pores was 58% at

the positive voltage and 21% at the negative voltage. In some other experiments (Figure 28B), there was no pore formed at the negative voltage, whereas there were transient or persistent pores at the positive voltage. We believe this phenomenon was due to the fact that the positive voltage drove the positively charged particles towards the bilayers while the negative voltage pulled the particles away from the bilayers.

The average conductance of the pores at 5mM was about 2.6 times of that at 150 mM, with the open probability of being 78% at 5mM 58% at 150 mM (Figure 29). The data agreed with a hypothesis that the NH2-NP-bilayer interaction is electrostatic in nature. At lower ionic strength, the interaction was stronger, and therefore it caused bigger pores and longer interaction time.

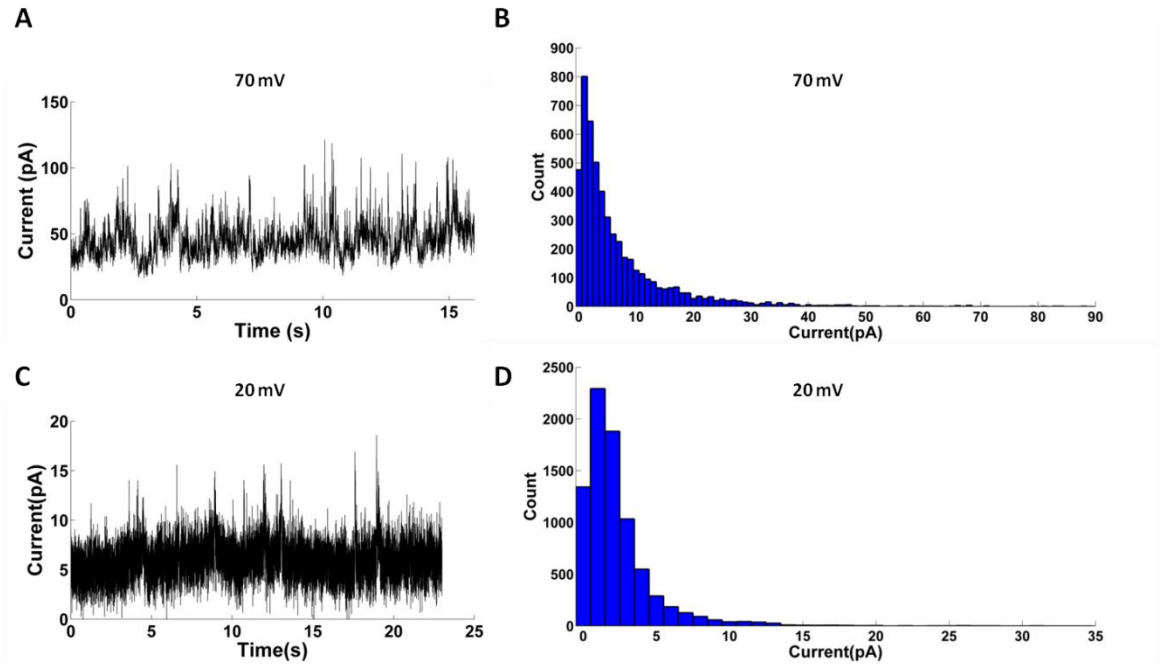

Figure 26. Impact of voltage magnitude. Representative traces at 70 mV (A) and 20 mV (C), and histogram of the transient pores at 70 mV (B) and 20 mV(D).

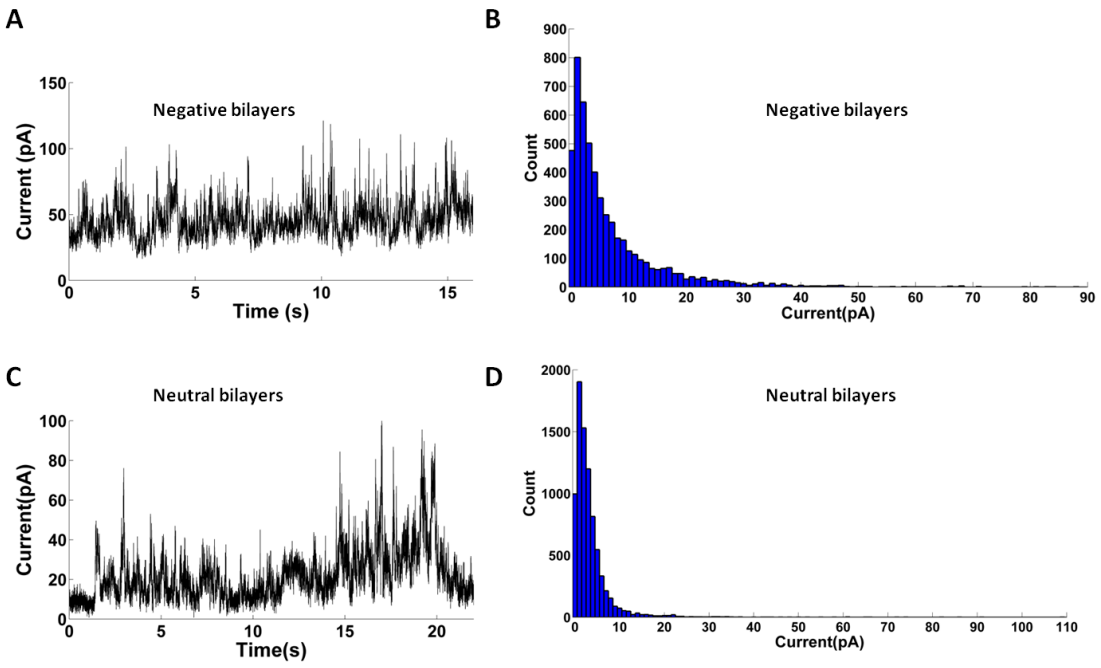

Figure 27. Impact of bilayer charge. Representative traces with negative bilayers (A) and neutral bilayers (C), and histogram of the transient pores with negative bilayers (B) and neutral bilayers (D).

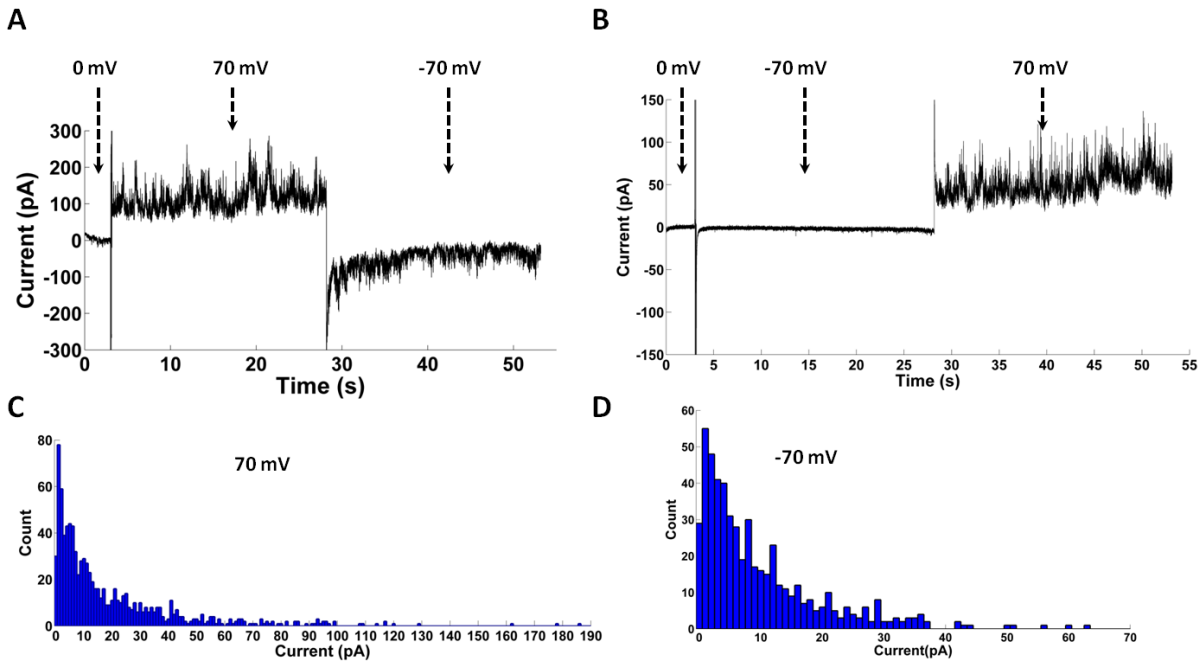

Figure 28. Impact of voltage sign. A and B are representative traces with sequential application of both positive and negative voltages. C is the histogram of the transient pores under the positive voltage in A. D is the histogram of the transient pores under the negative voltage in A.

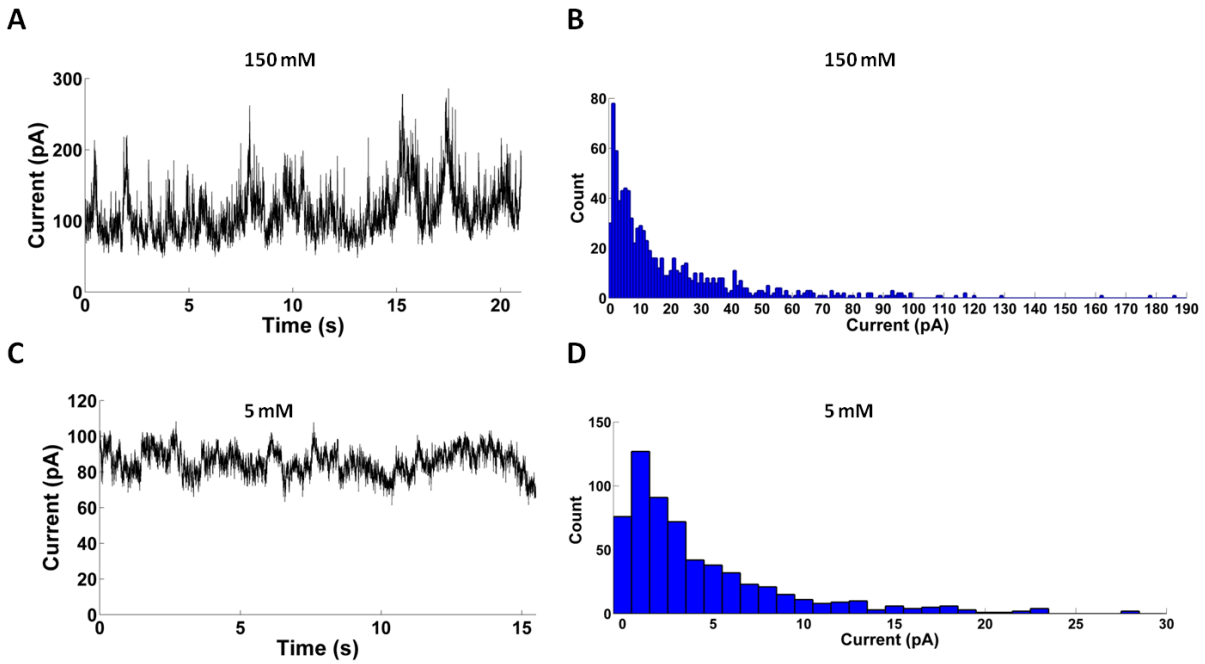

Figure 29. Impact of ionic strength. Representative traces at 150mM (A) and 5mM (C), and histogram of the transient pores at 150 mM (B) and 5 mM (D).

3.4 Summary and conclusion

We demonstrated that our lipid bilayer array platform could be used for the study of nanoparticle-membrane interaction. We confirmed that NH_2NP ruptured lipid membranes while COOHNP did not interact with membranes and that the NH_2NP-membrane interaction was electrostatic. Furthermore, our results proposed a mechanism of the membrane rupture: there were two different types of rupture: instant rupture or observable pore formation before rupture.

In the latter case, transient and persistent pores were formed with size of 0.3 ~ 2.3 nm in diameter. Sometimes, the pores grew over time and suddenly died down.

Chapter 4

4. Screening nanoparticle toxicity with lipid bilayer arrays

4.1 Introduction

Since our bilayer array platform was successfully validated with NH_2NP and COOHNP particles, we started to screen more nanoparticles against their abilities of interacting with membranes, further validating our bilayer array platform for the use of nanoparticle toxicity screening. A list of 16 nanoparticles (Table 3) was chosen for this study because of their industrial and biomedical applications.

Table 3. List of nanoparticles and their applications

Particle	**Applications/sources**
C60	MRI agent, drug delivery[140,141]
Cerium oxide	Industrial catalysts[142], drug delivery[143,144], cancer therapeutics[145,146]
Cobalt oxide	Pigments, catalysis, sensors, energy storage[147]
Copper	Inks[148], cosmetics
Copper oxide	Antimicrobial activity[149], semiconductor[150], sensors[151,152]
Erbium oxide	Display monitors, optical communication, biomedical imaging[153]
Europium oxide	Phosphors, fluorescent Label[154]
Gadolinium oxide	MRI contrast agent[155]
Hafnium oxide	Refractory materials[156], radiotherapy[157]
Indium oxide	Gas sensor[158,159], nanoelectronics[160], transistors[161], photo detector[162]

Iron oxide	Celluar therapy, tissue repair, drug delivery, MRI agent, hyperthermia[163], wastewater purification[164]
Lanthanum oxide	Catalytic material, exhaust-gas convectors[165], strengthening agent[166], biological applications: imaging, protein and DNA detection[167]
Platinum	Catalysis, cosmetics[168], DNA detection[169]
Silver	Antimicrobial activity[170], wound dressings, medical instruments, paint, laundry detergent[171]
Titanium oxide	Food colorant, sunscreen, pharmaceuticals, cosmetics[172–174]
Zinc oxide	Antibacterial activity[175], semiconductor, sunscreen, facial cream, and anti-caner treatment[176]

4.2 Materials and methods

4.2.1 Materials

A list of nanoparticles (Table 3) were purchased from Nanocomposix, Inc (San Diego, CA) or NanoAmor, Inc (Houston, TX). 1-palmitoyl-2-oleoyl-sn-glycero-3-phosphocholine (POPC), 1-palmitoyl-2-oleoyl-sn-glycero-3-phosphoethanolamine (POPE), Cholesterol (Chol), 1-palmitoyl-2-oleoyl-sn-glycero-3-phospho-L-serine (POPS), Cerebroside (CB), and sn-(3-oleoyl-2-hydroxy)-glycerol-1-phospho-sn-1'-(3'-oleoyl-2'-hydroxy)-glycerol (BMP) were ordered from Avanti Polar Lipids, Inc (Alabaster, Alabama). Decane was from Sigma-Aldrich (St. Louis, MO). Acrylics, delrin films, andVHP tapes were purchased from McMaster Carr (Santa Fe Springs, CA). aMEM and FBS were from Life Technologies (Camarillo, CA).

4.2.2 Nanoparticle characterization

The size of the particles and the zeta potential were measured with Zetasizer. Briefly, the particles were prepared in the solutions which were used for bilayer experiments, and 1 ml of the particle solution was transferred to a cuvette. Then the cuvette was loaded into the slot on the Zetasizer for measurement (Malvern). Triplicates of each measurement were conducted.

4.2.3 Solution preparation, chip fabrication and bilayer array formation

Liposomes and lipid in oil solutions were prepared as described previously[132]. Usually, the bilayers were made in two different conditions: 80 mM NaCl, 5mM Tris-HCl, pH 4.5 or aMEM with 10% FBS. The bilayers were made of POPC, POPE, Chol, POPS, CB, and BMP with a molar ratio of 3:3:3:1:2:2. The chips for bilayer formation were also fabricated as described previously[132].

As shown in Figure 18A, bilayers were made by following the protocol described in previous work [132] with slight modifications. Briefly, bilayers were formed by adding 450ul of 250ug/ml liposome solution to the outer wells of the chip, followed by 25ul of 10mg/ml lipid organic solution (decane) to the central well. After allowing 15 minutes for monolayer formation, 50ul of buffer solution without any lipid was added to the central well for bilayer formation and electrodes were placed into the aqueous solution in the central and outer wells for electrical measurement. After waiting an additional 15 minutes, 50~100 ul of liposome solution was added to each of the outer wells. To form bilayer arrays, two to four 8-well chips were used at a time (Figure 18B). The quality of bilayers was checked by applying 100/-100 mV for 10 minutes and the bilayers were considered good only if there was zero current passing the bilayers.

4.2.4 Electrical measurements of nanoparticle-bilayer interaction

The same measurement apparatus used in the previous work[132] was also used here as shown in Figure 18B. 5.5 ul of nanoparticle solutions (250 ug/ml~1 mg/ml) was added to the central wells with good bilayers (Figure 18A). The final concentration of the particles was in the range of 25 ug/ml to 1 mg/ml as specified in the result session. The particles were sonicated and vortexed to ensure full dispersion before use. At the same time, a control experiment in which 5.5 ul of buffer was added to the central wells was also conducted. Once the particles were added, a periodic voltage sweep composed of 70 mV for 25 seconds followed by -70 mV for another 25 seconds was applied to the bilayers and the conductance of the bilayers was monitored all the time for the next two hours unless the bilayers were ruptured earlier. There were multiple bilayers tested for each condition and the number was denoted as "n = #" in the result session.

4.2.5 Data analysis

The bilayer rupture percentage was calculated by dividing the total number of bilayers used by the number of bilayers ruptured. The difference in the bilayer rupture percentage between two experimental groups was analyzed using two-tail Fisher's test. If the p value from the test for the two groups is less than 0.05, it is concluded that there is significant difference between the two groups, and vice versa.

The recorded data by Tecella was converted into text files and then transferred into Matlab (MathWorks) for analysis. A baseline was chosen at a value which equals to the sum of lowest current for a given trace and the peak-to-peak noise level. Any current above the baseline was noted as the opening of pores. A transient pore event was defined as a time interval between the first time the current is above the baseline and the immediate next time the current is below the

baseline. A matlab script was written to pick out the opening events, the magnitude of the peak current for each event, and the duration of each event. The average pore size was calculated by modeling the pores as electrolyte-filled cylinders.

4.3 Results and discussion

4.3.1 Interaction of nanopaticles with lipid bilayers

A library of 17 different types of nanoparticles (Table 3) was screened against their impact on the bilayer conductance. When a particle was screened, an equal amount of control experiments was also conducted. Any events including either pore formation on bilayers or membrane rupture that led to the bilayer conductance change were monitored for both experimental and control groups. A particle-membrane interaction was evaluated by comparing the difference between the experimental and control groups. If the difference was statistically significant and the majority of the control bilayers did not show change in conductance, the nanoparticle was determined as having interaction with lipid bilayers. As shown in Figure 30, indium oxide (In_2O_3), zinc oxide (ZnO), C_{60} fullerene, cobalt oxide (Co_3O_4), copper oxide (CuO), erbium oxide (Er_2O_3), europium oxide (Eu_2O_3), cerium oxide (CeO_2), lanthanum oxide (La_2O_3), gadolinium oxide(Gd_2O_3) , and silver coated with branched polyethyleneimine (BPEI) nanoparticles interacted with bilayers, whereas Titanium oxide (TiO_2), Hafnium oxide (HfO_2), Iron oxide (Fe_3O_4), and Platinum and silver nanoparticles coated with citrate or polyvinylpyrrolidone (PVP) did not. The interaction for each nanoparticle is described in detail in the following sections.

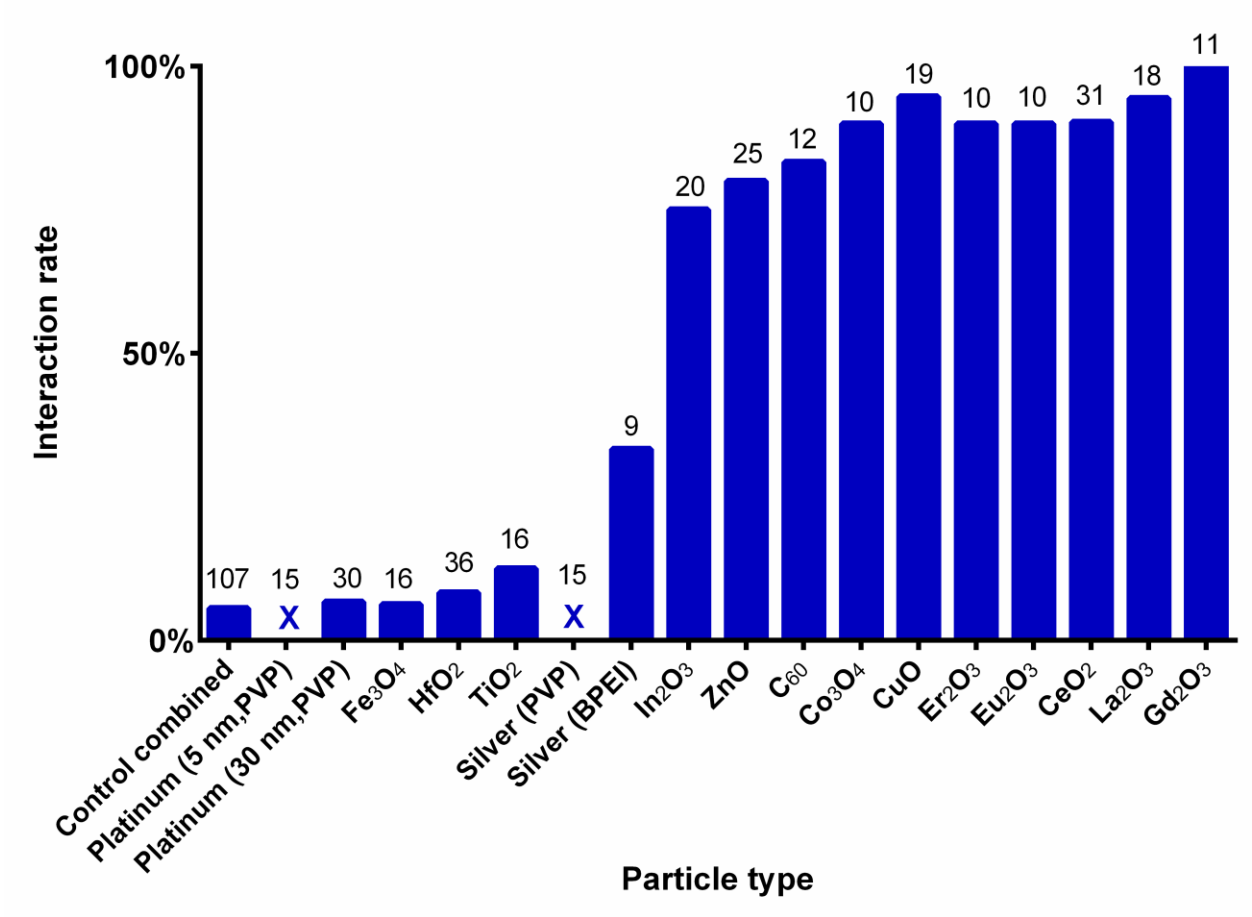

Figure 30. Interaction of different nanoparticles with lipid bilayers. In_2O_3, ZnO, C_{60}, Co_3O_4, CuO, Er_2O_3, Eu_2O_3, CeO_2, La_2O_3, Gd_2O_3, and BPEI-silver nanoparticles interacted with bilayers, but TiO_2, HfO_2, Fe_3O_4, PVP-Platinum, and citrate-silver nanoparticles did not. Both pore formation on bilayers and bilayer rupture caused by the particles were counted as particle-membrane interactions. Bilayer composition: POPC, POPE, Chol, POPS, CB, and BMP (molar ratio, 3:3:3:1:2:2). Buffer: 80 mM NaCl, 5mM Tris-HCl, pH 4.5. Particle concentration: 20~500 μg/ml. The number of bilayers tested for each particle was marked down on top of each bar in the graph. "X" denotes as no interaction.

4.3.2 Rare earth oxides (REOs) nanoparticles

Five different rare earth oxides: CeO_2, La_2O_3, Gd_2O_3, Er_2O_3, and Eu_2O_3 were chosen in our study and all of them showed interactions with bilayers. The interaction was categorized into three types (Figure 31 & Table 4):

Type I: Instant bilayer rupture. Bilayers were damaged instantly and no pore formation was observed (Figure 31B).

Type II: Pore formation leading to bilayer rupture. Pores formed on bilayers first, and then the bilayers were ruptured (Figure 31C-D).

Type III: Pore formation without leading to bilayer rupture. There were pore formation activities, but the pores disappeared over time and the bilayers did not get ruptured (Figure 31E-F).

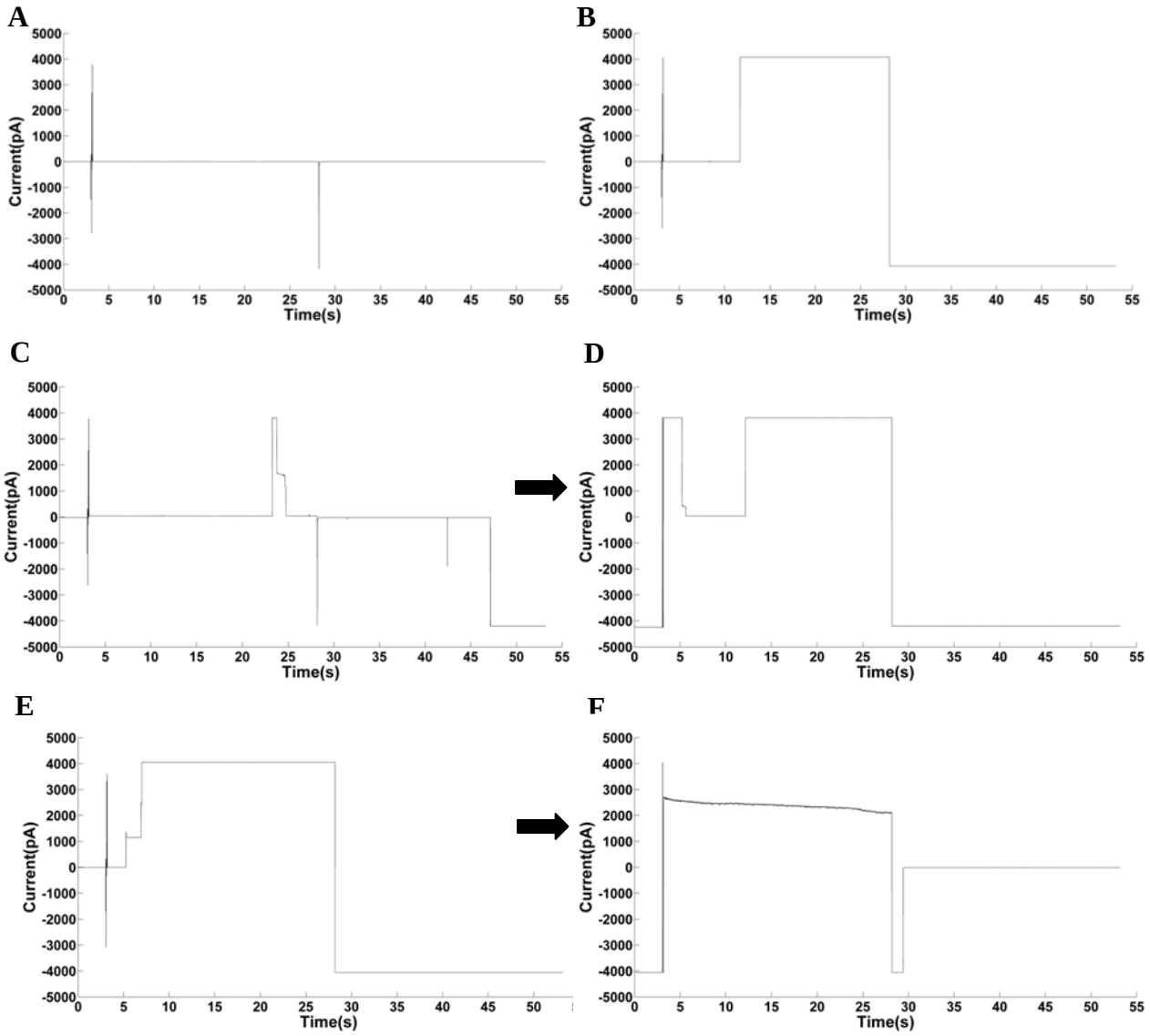

Figure 31. Representative current recordings of bilayers without (A) and with (B-F) REOs nanoparticles. (A) Bilayers without nanoparticles showed 0 current under the applied voltage. (B) Instant bilayer rupture. (C-D) Pore formation leading to bilayer rupture. There was transient pore formation, followed by bilayer rupture. (E-F) Pore formation without leading to bilayer rupture. Transient pore formation did not lead to bilayer rupture, instead the pores were gone and bilayers regained high resistance. Applied voltage: 0 mV for 3 s, and then triangle wave for 180

ms, followed by 100 mV (A-D) or 20 mV (E-F) for 25 s and -100 mV (A-D) or -20 mV (E-F) for another 25 s.

Table 4 Percentage of each interaction type for different REO nanoparticles

Interaction type	CeO_2	La_2O_3	Gd_2O_3	Er_2O_3	Eu_2O_3
I (instant rupture)	9/28, 32%	11/14, 79%	4/9, 44%	5/9, 56%	5/9, 56%
II (pore + rupture)	15/28, 54%	2/14, 14%	5/9, 56%	4/9, 44%	4/9, 44$
III (pore + no rupture)	4/28, 14%	1/14, 7%	0/9, 0%	0/9, 0%	0/9, 0%

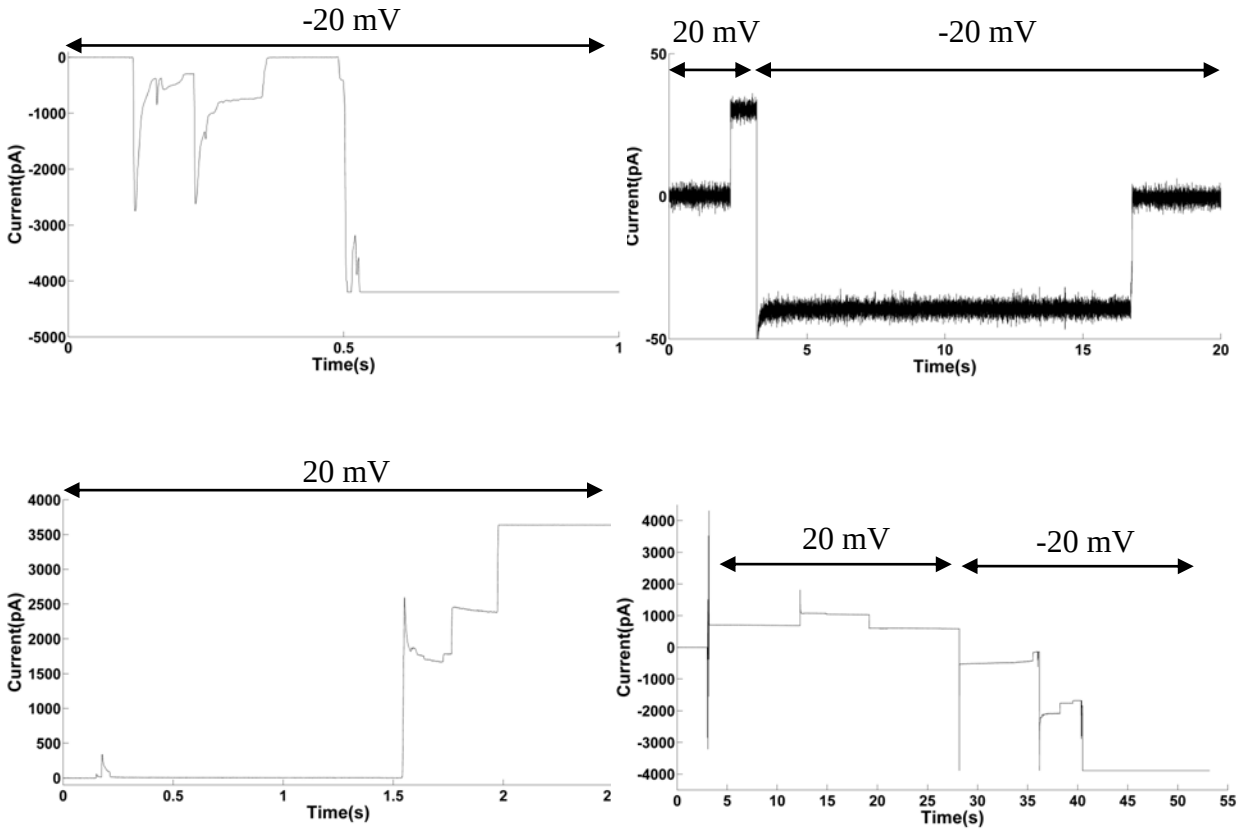

Figure 32. Representative traces of pore formation in CeO_2-bilayer interaction.

4.3.2.1 CeO_2

When CeO_2 was used at 500 μg/ml or 100 μg/ml, the particle broke all bilayers (n=8) instantly. At 20 μg/ml, CeO_2 ruptured 28 out of 32 bilayers. Out of the 28 bilayers, 9 were ruptured instantly and 19 experienced transient pore formation (Table 4). For the 19 bilayers with transient pore formation, 15 were ruptured eventually while the other 4 were not (Figure 31C-D). Instead, those 4 bilayers regained high resistance and showed zero current under the applied voltage (Figure 31EF). The transient pores (Figure 32) behaved like ion channels, with some sudden discrete step change of currents greater than 4 nA under 20 mV. If the pores were modeled as electrolyte filled cylinders, the diameter of the pores was estimated with the smallest being 1.9 nm and the largest being greater than 18.6 nm. The pore size is very close to that of CeO_2 nanoparticles (15~30 nm). As such, we hypothesized that it was very likely that CeO_2 nanoparticles penetrate bilayers when the pores formed. Also, there was a possibility that CeO_2 nanoparticles came together on the bilayer surface and helped form pores.

4.3.2.2 La_2O_3, Gd_2O_3, Er_2O_3, and Eu_2O_3

La_2O_3 nanoparticles also showed three types of interactions, with 11/14 or 79% for instant rupture, 2/14 or 14% for pore formation leading to rupture, and 1/14 or 7% for pore formation without leading to rupture (Table 4). Some transient pores behaved similarly to the ones in the CeO_2 case, but the size was smaller (Figure 33).

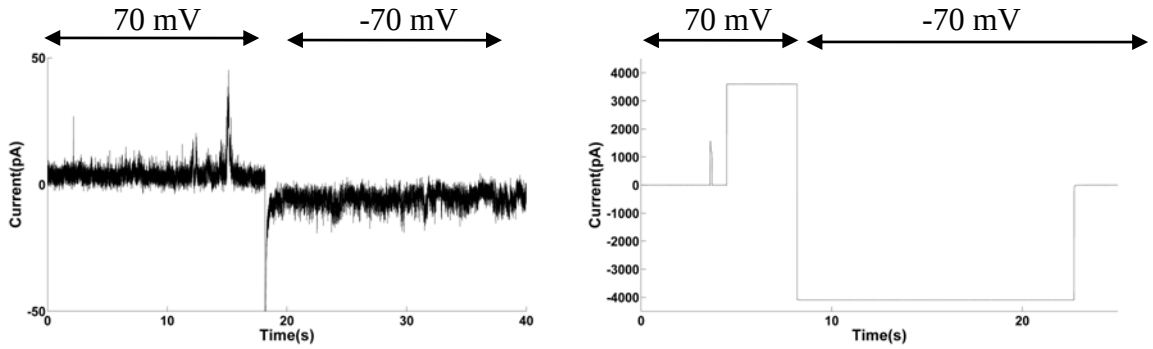

Figure 33. Representative traces of pore formation in La_2O_3-bilayer interaction.

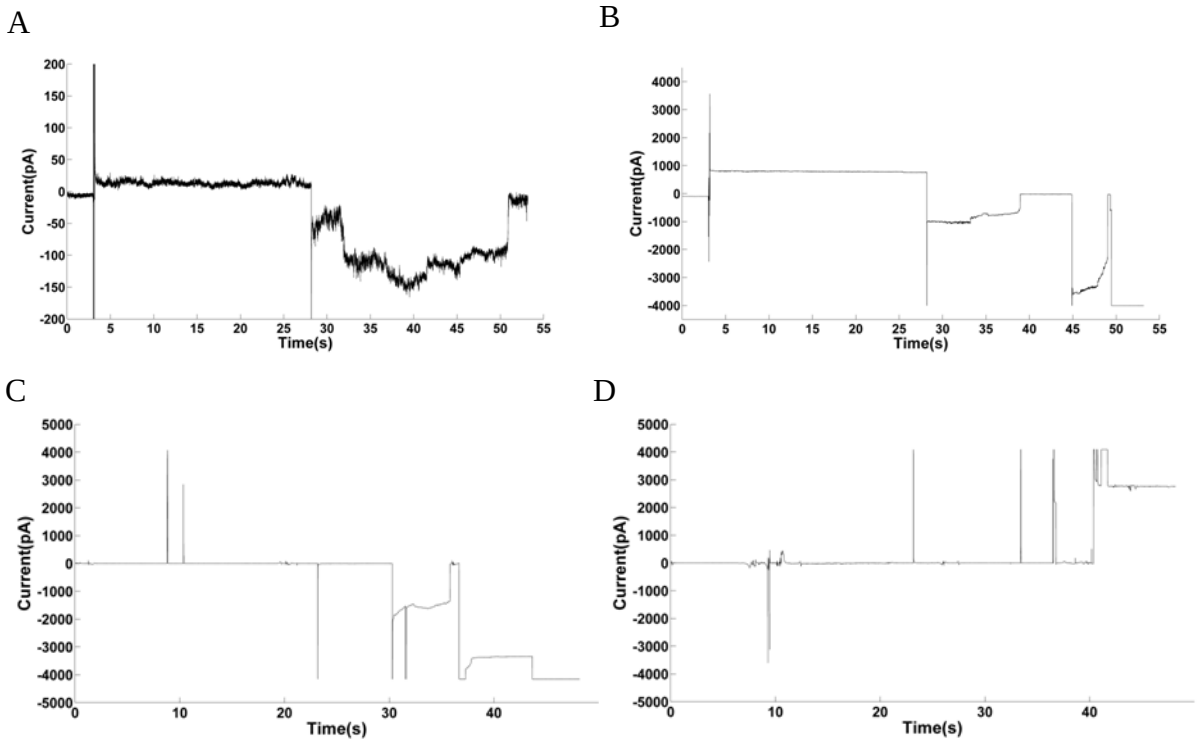

Figure 34. Rerepresentative traces of pore formation in Gd_2O_3 (A-B) and Er2O3 (C-D) bilayer interaction. Applied voltage: (A-B), 0 mV for 3 s, and then triangle wave for 180 ms, followed by 70 mV for 25 s and -70 mV for another 25 s. (C-D), 70 mV for the first 22 s, followed by -70 mV for another 23 s.

Gd_2O_3, Er_2O_3, and Eu_2O_3 only exhibited type I and type II interactions (Table 4). The bilayers were either ruptured instantly or damaged after showing pore formation (Figure 34).

Ruibin Li and coworkers recently showed that rare earth oxides including La_2O_3, Gd_2O_3, Er_2O_3, and Eu2O3 damaged liposomes by stripping the phosphate groups from lipid bilayers[177], with which our results agreed. In their study CeO_2 did not break the liposomes made of phosphatidic acid lipids in 60 mM NaCl, pH 7 buffer. In contrast, our results showed that CeO_2 interacted with 28/32 bilayers. 24/28 bilayers were eventually ruptured, while the other 4 bilayers returned to normal after showing pore formation activities. We attributed the difference between our results and Li's results to the fact that we conducted our experiments with a combination of 6 different lipids representing 95% of lysosomal membrane composition in lysosomal buffer condition: 80 mM NaCl, pH 4.5.

4.3.4 Nanoparticles of different surface coating

Silver nanoparticles of either PVP or BPEI surface coating were used in our study. Our results showed that BPEI silver particles slightly interacted with bilayers whereas PVP silver particles did not (Figure 35A). 3 out of 9 bilayers interacted with both 50 nm and 100 nm BPEI particles, and 1 out of 9 with 10 nm BPEI particles. The particles interacted with bilayers by generating pores (Figure 35B), which was voltage dependent. There was pore formation under positive voltage but not under negative voltage. Those results were consistent with the fact that BPEI silver particles were positively charged and that PVP particles were negatively charged. We believed that the interaction between BPEI particles and bilayers was due to the electrostatic interaction between the positive charge on particle and the zwitterionic phosphocholine lipid

head. Our results also agreed with El Badawy and coworkers' findings that the positively charged BPEI sliver particle was more toxic than the negatively charge PVP particles[178].

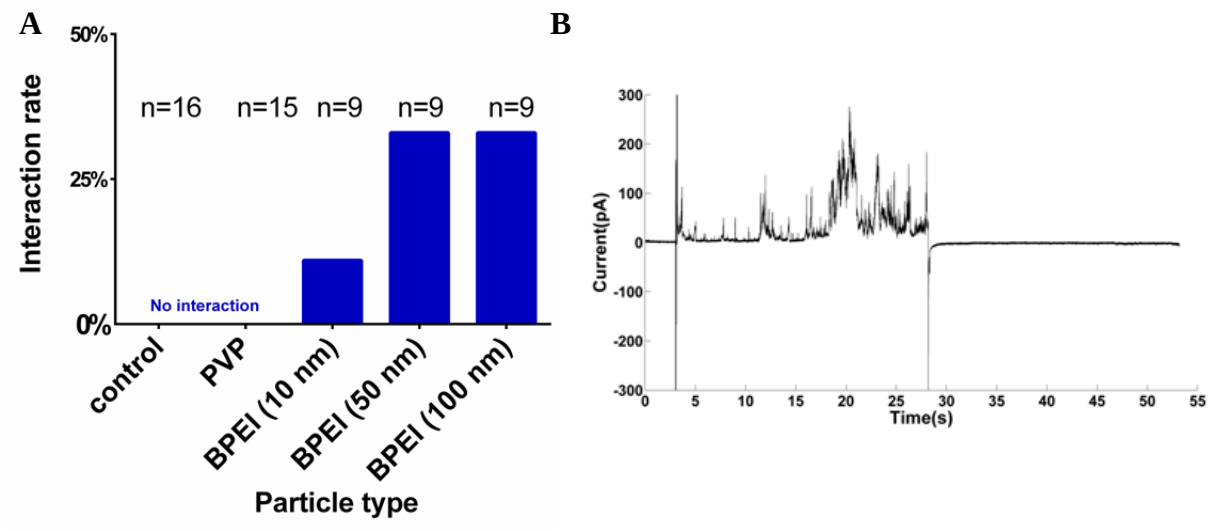

Figure 35. Interaction between bilayers and sliver nanoparticles of different surface coating. (A) Interaction rate of sliver-bilayer depends on the surface coating. Particles with citrate coating did not interact with bilayers, while particles with BPEI coating slightly interacted with bilayers. (B) Representative current recordings of BPEI silver particle with bilayers. The interaction was voltage dependent. Applied voltage: 0 mV for 3 s, and then triangle wave for 180 ms, followed by 70 mV for 25 s and -70 mV for another 25 s.

We also found that Platinum nanoparticles of 5 nm or 30 nm in diameter with sodium citrate coating did not interact with bilayers either (Figure 30). This result was not surprising given that the zeta potential of the nanoparticles is -42.2 mV, which is similar to that of COOH-NP. Chwalibog and coworkers discovered that platinum nanoparticles with diameter of 2-19 nm disintegrated the cytoplasmic membrane of *Staphylococcus aureus* (bacteria) and *Candida albicans* (fungi)[179]. We think the difference in nanoparticle surface coating contributed to the

variation of the results. In Chwalibog's study, the nanoparticles were not coated, with a zeta potential of -9.6 mV.

4.3.5 Cobalt oxide

As shown in Figure 36, Cobalt oxide (Co_3O_4) nanoparticles interacted with bilayers in two different ways: the particles broke bilayers instantly (Figure 36A) or caused transient pore formation (Figure 36BC) on bilayers. Our results also showed that Co_3O_4 nanoparticles interacted with bilayers in a dose-dependent manner. When the particle concentration was at 500 μg/ml, 90% or 9 out of 10 bilayers showed interactions with the particles. When the concentration decreased to 100 μg/ml, there was 20% or 2 out of 10 bilayers that were damaged, which was not significantly different from the control group without any particles. Therefore, 100 μg/ml Co_3O_4 nanoparticles were not considered having interaction with bilayers. Among the 9 bilayers ruptured by the particles, 7 of them were damaged instantly, with the other 2 showing transient pore formation before rupture. Since the transient pores opened and closed very sharply like ion channels, we believed that there was only one pore for each pore formation event. As such, the diameter of the pores was estimated at 5.4 nm (Figure 36B) or 7.8 nm (Figure 36C).

To the best of our knowledge, there has not been any study investigating the interaction between Co_3O_4 and cell membranes or lipid bilayers although there are reports about Co_3O_4 releasing cobalt ions which are more toxic to cells compared to the Co_3O_4 particles[180,181]. According to those studies, cells can uptake Co_3O_4 nanoparticles. Combined with our results, it is possible that Co_3O_4 particles can directly interact with intracellular membrane systems, which could be another aspect of the particles' toxicity.

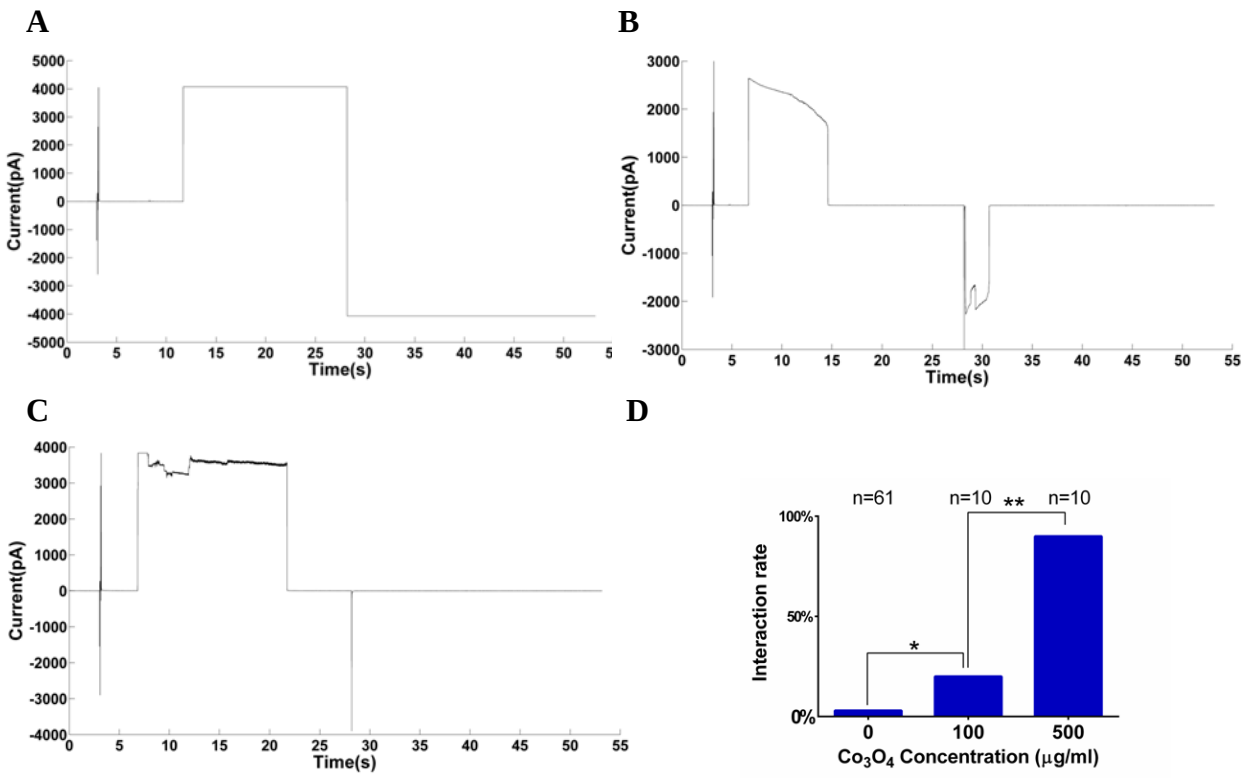

Figure 36. Representative current recordings of Co_3O_4-bilayer interaction. (A) Bilayers were ruptured by Co_3O_4 instantly. (B-C) Bilayers showed transient pore formation. (D) Rate of Co_3O_4-bilayer interaction as a function of Co_3O_4 nanoparticle concentration. The interaction rate was 90% when Co_3O_4 concentration was 500μg/ml, 20% at 100 μg/ml, and 3% at 0 μg/ml (control), respectively. The difference between 500 μg/ml and 100 μg/ml or control was statistically significant, whereas the difference between 100 μg/ml and control was not significant. The number of bilayers tested for each group was denoted as "n=number". "**"p(Fisher's test) < 0.05, "*"p(Fisher's test) > 0.05. Applied voltage: 0 mV for 3 s, and then triangle wave for 180 ms, followed by 70 mV for 25 s and -70 mV for another 25 s.

4.3.6 Indium oxide

Research has been done to study the toxicity of Indium oxide (In_2O_3) nanoparticles in animal models and it showed that In_2O_3 was toxic to the lungs of Hamsters[182]. However, it is still not clear how In_2O_3 can be harmful, especially from the perspective of particle-membrane interaction. In our study, we tried to use our bilayer platform to probe possible interaction between indium oxide nanoparticles and membranes. Our results showed that In_2O_3 interacted with bilayers (Figure 37). Again, there were two different types of In_2O_3-bilayer interaction: instant bilayer rupture or pore formation followed by bilayer rupture (Figure 37). Compared to the control group, experimental groups with either 500 μg/ml or 100 μg/ml In_2O_3 showed significant particle-bilayer interaction. The interaction rate was 75% or 15/20 when In_2O_3 concentration was 500 μg/ml, while it was 50% or 9/18 when the concentration was 100 μg/ml. However, there was significant difference between the two concentration groups in terms of particle-bilayer interaction. The pores that resulted from the interaction behaved like ion channels (Figure 37BD) with distinguished step changes of 4pA, 10 pA, 25 pA, and 40 pA, which correspond to pore size of 0.31 nm, 0.50 nm, 0.79nm, and 0.99 nm, respectively. The pore formation eventually led to bilayer rupture.

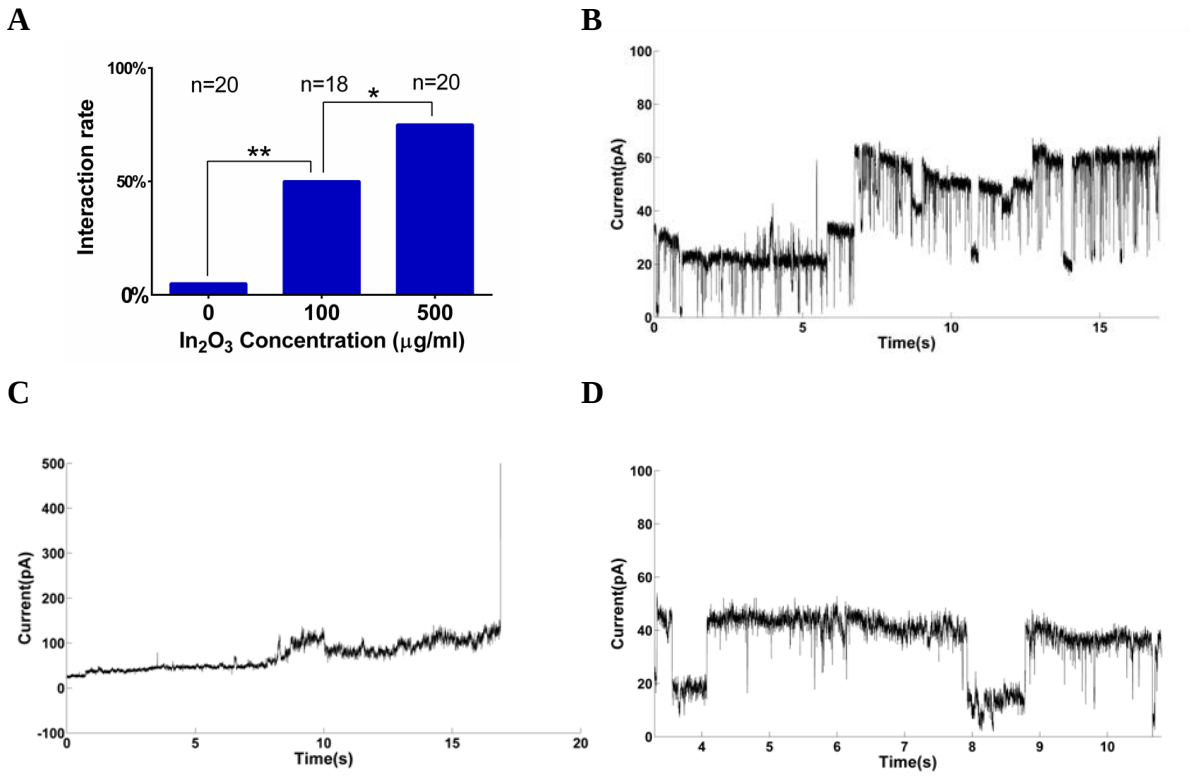

Figure 37. In_2O_3-bilayer interaction. (A) Rate of In_2O_3-bilayer interaction as a function of In_2O_3 nanoparticle concentration. The interaction rate was 75% when In_2O_3 concentration was 500μg/ml, 50% at 100 μg/ml, and 5% at 0 μg/ml (control), respectively. The difference between 500 μg/ml or 100 μg/ml and control was statistically significant, whereas the difference between 500 μg/ml and 100 μg/ml was not significant. The number of bilayers tested for each group was denoted as "n=number". "**"p(Fisher's test) < 0.05, "*"p(Fisher's test) > 0.05. (B-D) Representative current recordings of pore formation in In_2O_3-bilayer interaction. Applied voltage: 70 mV. The three traces were from three different experiments.

4.3.7 Zinc Oxide, Copper oxide, and C_{60} fullerene

Zinc oxide (ZnO) also showed the ability to damage bilayers. At 100 μg/ml, ZnO broke 6 out 7 bilayers instantly. When the concentration was reduced to 50 μg/ml, 10 out of 14 bilayers were

ruptured and 4 of the 10 bilayers showed pore formation prior to rupture (Figure 38). Again, our results agreed with multiple studies[183,184] in which the capability of ZnO to disrupt cell membranes was assessed through the measurement of release of a cellular interior content, Lactate Dehydrogenase (LDH).

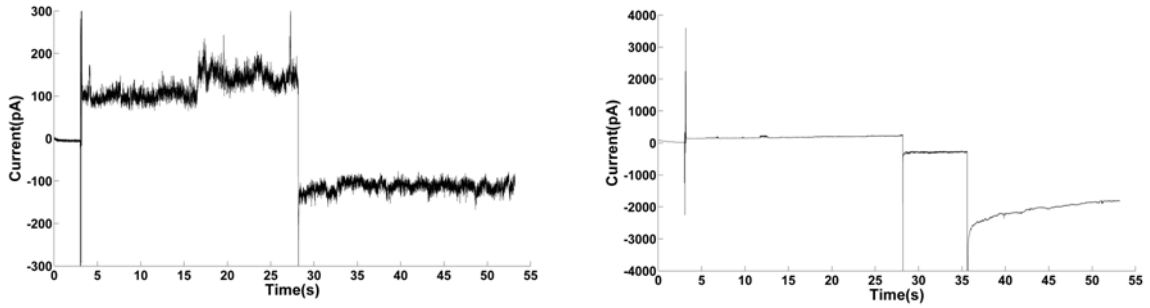

Figure 38. Representative traces of pore formation in ZnO-bilayer interaction. Applied voltage: 0 mV for 3 s, and then triangle wave for 180 ms, followed by 70 mV for 25 s and -70 mV for another 25 s.

Copper oxide (CuO) showed great potency for bilayer rupture by breaking 18 out of 19 bilayers instantly combined at 100 and 500 μg/ml. Our results also agreed with Karlsson and coworkers' findings that CuO was able to induce particle-membrane interaction, possibly by absorbing lipids from the membrane[185]. Therefore, we hypothesize that CuO nanoparticles are capable of removing lipids from the membrane and generating pores that lead to membrane rupture.

C_{60} damaged 10 out of 12 bilayers instantly. Previous work by Prylutska and coworkers also showed that C_{60} fullerenes induced pores on lipid bilayers[186].

4.3.8 Titanium oxide, Hafnium oxide, and Iron oxide

Titanium oxide (TiO_2), Hafnium oxide (HfO_2), and Iron oxide (Fe_3O_4) were found not to interact with bilayers, even at a high concentration of 500 μg/ml. The results for TiO_2 and Fe_3O_4 agreed with Karlsson and coworkers' findings that TiO_2 and Fe_3O_4 did not decrease cell viability[187]. Researchers also found TiO_2 did not strip lipids from liposomes[177]. There are also studies that show HfO_2 is relatively non-toxic[188].

4.4 Conclusion

With our lipid bilayer array platform, for the first time we have identified that CeO_2, Co_3O_4, and In_2O_3 can break lysosomal membranes, and that Fe_3O_4, HfO_2, and TiO_2 can not. Also, our platform confirmed that ZnO, C_{60}, CuO, Er_2O_3, Eu_2O_3, La_2O_3, and Gd_2O_3 can disrupt lipid bilayers. The data from our bilayer array platform also indicates that the ability of nanoparticles to destruct membranes largely depends on the surface coating. In general, positive coating like BPEI makes the particles more potent to membranes, and negative coating like citrate or PVP makes the particles safer.

Furthermore, our results about nanoparticles' ability to rupure bilayers are highly correlated with the cytotoxicity data in the literature. Therefore, our bilayer array platform has a great potential of being used for nanoparticle toxicity screening.

Chapter 5

5. Conclusion and future plans

5.1 Conclusion

Firstly, we developed an artificial lipid bilayer array platform that is of high yield, scalable, automatable, accessible to electrical measurement, and requires minimal operator input and equipment. The platform has been validated with simultaneous bilayer formation and ion channel measurement in parallel in 32 wells with yield of about 80%. In addition, we designed a modular system for array and electrode placement that allowed the measurement plates and electrodes to be quickly removed and accurately repositioned. We manually cycled this apparatus four times, resulting in the formation and measurement of 120 wells at 80% yield in 80 minutes. Since invented in 2012, the platform has produced thousands of lipid bilayers.

Secondly, we validated the application of our lipid bilayer platform in nanoparticle-membrane interaction study, using amine or carboxyl modified polystyrene nanoparticles. With our platform, lipid bilayers were made of lipids that represent 95% of the lipid composition of either mammalian plasma membrane or lysosomal membrane. Our results confirmed that in general amine modified polystyrene nanoparticle (NH_2-NP) has the ability to damage lipid bilayers and that carboxyl modified polystyrene nanoparticles (COOH-NP) does not. Factors including ionic strength, particle concentration, bilayer charge, and pH were investigated regarding their impact on NH_2-NP – bilayer interaction, which led to the conclusion that the particle-bilayer interaction is electrostatic. Our results also showed that NH_2-NP does not break plasma membrane but lysosomal membrane because serum proteins outside plasma membrane bind to the nanoparticles. For the first time, we discovered that NH_2-NP ruptures bilayers by generating

either transient or persistent pores on bilayers. Deep pore analysis showed that the pore size was significantly affected by the ionic strength and voltage orientation, modestly by bilayer charge, and slightly by voltage magnitude.

Thirdly, we conducted nanoparticle toxicity screening with our bilayer array platform. For the first time we identified that CeO_2, Co_3O_4, and In_2O_3 can damage lysosomal membranes, and that Fe_3O_4, HfO_2, and TiO_2 cannot. Also, our platform confirmed that ZnO, C_{60}, CuO, Er_2O_3, Eu_2O_3, La_2O_3, and Gd_2O_3 disrupt lipid bilayers. The data from our bilayer array platform also indicated that the ability of nanoparticles to destruct membranes largely depends on the surface coating. In general, positive coating like BPEI makes the particles more potent to membranes, and negative coating like citrate or PVP makes the particles safer. Our results about nanoparticles' ability to rupture bilayers are highly correlated with the cytotoxicity data in the literature. Therefore, our bilayer array platform has a great potential of being used for nanoparticle toxicity screening.

In summary, we have invented an easy and high yield lipid bilayer array platform, successfully demonstrated its application in nanoparticle-bilayer interaction study, and finally discovered that some nanoparticles can damage lysosomal membranes.

5. 2 Future plans

Moving forward, there should be more efforts for both technology advancement and application demonstration. For the bilayer array platform, we plan to miniaturize the system based on our core principle of forming bilayers via simple fluid addition. To miniaturize the system, we would like to utilize fabrication technologies[189,190] to make apertures less than 10 μm. Meanwhile, other elements of our normal chip for bilayer formation will also be scaled down using microfluidic technologies. The miniaturized system will potentially offer several benefits:

(1) Lower noise level; (2) Smaller working volume. The low noise is very critical for stochastic sensing, especially DNA sequencing[86]. Small working volume helps reduce the consumption of materials used for bilayer formation, especially for some precious chemical for ion channel drug screening. For nanoparticle study, we plan to screen more nanoparticles and meanwhile dig deep to probe the mechanism of particle-bilayer interaction. The nanoparticles for the next round of screening will include non-metal elements such as Si and SiO_2. We discovered that CeO_2, Co_3O_4, In_2O_3, ZnO, C_{60}, CuO, Er_2O_3, Eu_2O_3, La_2O_3, and Gd_2O_3 damage bilayers. Next, we would like to investigate why they are potent to bilayers by varying conditions including ionic strength, bilayer charge, pH, and serum. In addition, we also want to use cell assays such as hemolysis and cellular content release to confirm the findings from our lipid bilayer arrays.

6. References

(1) Mueller, P.; Rudin, D. O.; Tien, H. T.; Wescott, W. C. Reconstitution of Cell Membrane Structure in Vitro and Its Transformation into an Excitable System. *Nature* **1962**, *194*, 979–980.

(2) Montal, M.; Mueller, P. Formation of Bimolecular Membranes from Lipid Monolayers and a Study of Their Electrical Properties. *Proc Natl Acad Sci U S A* **1972**, *69*, 3561–3566.

(3) Schindler, H. Formation of Planar Bilayers from Artificial or Native Membrane Vesicles. *FEBS Lett* **1980**, *122*, 77–79.

(4) Coronado, R.; Latorre, R. Phospholipid Bilayers Made from Monolayers on Patch-Clamp Pipettes. *Biophys J* **1983**, *43*, 231–236.

(5) Schmidt, C.; Mayer, M.; Vogel, H. A Chip-Based Biosensor for the Functional Analysis of Single Ion Channels. *Angew Chem Int Ed Engl* **2000**, *39*, 3137–3140.

(6) L.M. Tsofina, E. A. L. and A. V. B. Production of Bimolecular Protein-Lipid Membranes in Aqueous Solution. *Nature* **1966**, *21*, 681–683.

(7) Malmstadt, N.; Nash, M. a; Purnell, R. F.; Schmidt, J. J. Automated Formation of Lipid-Bilayer Membranes in a Microfluidic Device. *Nano Lett.* **2006**, *6*, 1961–1965.

(8) Mayer, M.; Kriebel, J. K.; Tosteson, M. T.; Whitesides, G. M. Microfabricated Teflon Membranes for Low-Noise Recordings of Ion Channels in Planar Lipid Bilayers. *Biophys. J.* **2003**, *85*, 2684–2695.

(9) Orth, A.; Johannes, L.; Römer, W.; Steinem, C. Creating and Modulating Microdomains in Pore-Spanning Membranes. *Chemphyschem* **2012**, *13*, 108–114.

(10) Höfer, I.; Steinem, C. A Membrane Fusion Assay Based on Pore-Spanning Lipid Bilayers. *Soft Matter* **2011**, *7*, 1644.

(11) Funakoshi, K.; Suzuki, H.; Takeuchi, S. Lipid Bilayer Formation by Contacting Monolayers in a Microfluidic Device for Membrane Protein Analysis. *Anal Chem* **2006**, *78*, 8169–8174.

(12) Bayley, H.; Cronin, B.; Heron, A.; Holden, M. A.; Hwang, W. L.; Syeda, R.; Thompson, J.; Wallace, M. Droplet Interface Bilayers. *Mol Biosyst* **2008**, *4*, 1191–1208.

(13) Hwang, W. L.; Chen, M.; Cronin, B.; Holden, M. a; Bayley, H. Asymmetric Droplet Interface Bilayers. *J. Am. Chem. Soc.* **2008**, *130*, 5878–5879.

(14) Holden, M. A.; Needham, D.; Bayley, H. Functional Bionetworks from Nanoliter Water Droplets. *J Am Chem Soc* **2007**, *129*, 8650–8655.

(15) Poulos, J. L.; Portonovo, S. A.; Bang, H.; Schmidt, J. J. Automatable Lipid Bilayer Formation and Ion Channel Measurement Using Sessile Droplets. *J Phys Condens Matter* **2010**, *22*, 454105.

(16) Le Pioufle, B.; Suzuki, H.; Tabata, K. V; Noji, H.; Takeuchi, S. Lipid Bilayer Microarray for Parallel Recording of Transmembrane Ion Currents. *Anal Chem* **2008**, *80*, 328–332.

(17) Zagnoni, M.; Sandison, M. E.; Marius, P.; Morgan, H. Bilayer Lipid Membranes from Falling Droplets. *Anal Bioanal Chem* **2009**, *393*, 1601–1605.

(18) Poulos, J. L.; Jeon, T. J.; Damoiseaux, R.; Gillespie, E. J.; Bradley, K. A.; Schmidt, J. J. Ion Channel and Toxin Measurement Using a High Throughput Lipid Membrane Platform. *Biosens Bioelectron* **2009**, *24*, 1806–1810.

(19) Aghdaei, S.; Sandison, M. E.; Zagnoni, M.; Green, N. G.; Morgan, H. Formation of Artificial Lipid Bilayers Using Droplet Dielectrophoresis. *Lab Chip* **2008**, *8*, 1617–1620.

(20) Poulos, J. L.; Nelson, W. C.; Jeon, T.-J.; Kim, C.-J. C. J.; Schmidt, J. J. Electrowetting on Dielectric-Based Microfluidics for Integrated Lipid Bilayer Formation and Measurement. *Appl. Phys. Lett.* **2009**, *95*, 13706.

(21) Kawano, R.; Tsuji, Y.; Sato, K.; Osaki, T.; Kamiya, K.; Hirano, M.; Ide, T.; Miki, N.; Takeuchi, S. Automated Parallel Recordings of Topologically Identified Single Ion Channels. *Sci Rep* **2013**, *3*, 1995.

(22) Bean, R. C.; Shepherd, W. C.; Chan, H.; Eichner, J. Discrete Conductance Fluctuations in Lipid Bilayer Protein Membranes. *J. Gen. Physiol.* **1969**, *53*, 741–757.

(23) BOHEIM, B. S. & G. Alamethicin-Induced Single Channel Conductance Fluctuations in Biological Membranes. *Nature* **1979**, *282*, 336–339.

(24) Morrow, J. S.; Veatch, W. R.; Stryer, L. Transmembrane Channel Activity of Gramicidin A Analogs: Effects of Modification and Deletion of the Amino-Terminal Residue. *J. Mol. Biol.* **1979**, *132*, 733–738.

(25) Belmonte, G.; Cescatti, L.; Ferrari, B.; Nicolussi, T.; Ropele, M.; Menestrina, G. Pore Formation by Staphylococcus Aureus Alpha-Toxin in Lipid Bilayers. Dependence upon Temperature and Toxin Concentration. *Eur Biophys J* **1987**, *14*, 349–358.

(26) Gouaux, J. E.; Braha, O.; Hobaugh, M. R.; Song, L.; Cheley, S.; Shustak, C.; Bayley, H. Subunit Stoichiometry of Staphylococcal Alpha-Hemolysin in Crystals and on Membranes: A Heptameric Transmembrane Pore. *Proc. Natl. Acad. Sci. U. S. A.* **1994**, *91*, 12828–12831.

(27) Friddin, M. S.; Smithers, N. P.; Beaugrand, M.; Marcotte, I.; Williamson, P. T. F.; Morgan, H.; de Planque, M. R. R. Single-Channel Electrophysiology of Cell-Free Expressed Ion Channels by Direct Incorporation in Lipid Bilayers. *Analyst* **2013**, *138*, 7294–7298.

(28) Oshima, A.; Hirano-Iwata, A.; Mozumi, H.; Ishinari, Y.; Kimura, Y.; Niwano, M. Reconstitution of Human Ether-a-Go-Go-Related Gene Channels in Microfabricated Silicon Chips. *Anal. Chem.* **2013**, *85*, 4363–4369.

(29) Tao, X.; MacKinnon, R. Functional Analysis of Kv1.2 and Paddle Chimera Kv Channels in Planar Lipid Bilayers. *J Mol Biol* **2008**, *382*, 24–33.

(30) Coronado, Roberto; Miller, C. Decamethonium and Hexamethonium Block K+ Channels of Sarcoplasmic Reticulum. **1980**, *288*, 495–497.

(31) ROSENBERG， ROBERT & EAST，JOAN. Cell-Free Expression of Functional Shaker Potassium Channels. *Nature* **1992**, *12*, 166–169.

(32) Leptihn, S.; Thompson, J. R.; Ellory, J. C.; Tucker, S. J.; Wallace, M. I. In Vitro Reconstitution of Eukaryotic Ion Channels Using Droplet Interface Bilayers. *J Am Chem Soc* **2011**, *133*, 9370–9375.

(33) Hartshorne, R. P.; Keller, B. U.; Talvenheimo, J. a; Catterall, W. a; Montal, M. Functional Reconstitution of the Purified Brain Sodium Channel in Planar Lipid Bilayers. *Proc. Natl. Acad. Sci. U. S. A.* **1985**, *82*, 240–244.

(34) Hartshorne, R. P.; Keller, B. U.; Talvenheimo, J. a; Catterall, W. a; Montal, M. Functional Reconstitution of Purified Sodium Channels from Brain in Planar Lipid Bilayers. *Ann. N. Y. Acad. Sci.* **1986**, *479*, 293–305.

(35) Oh, Y.; Benos, D. J. Rapid Purification of an Amiloride-Sensitive Na+ Channel from Bovine Kidney and Its Functional Reconstitution. *Protein expression and purification*, 1993, *4*, 312–319.

(36) Senyk, O.; Ismailov, I.; Bradford, a L.; Baker, R. R.; Matalon, S.; Benos, D. J. Reconstitution of Immunopurified Alveolar Type II Cell Na+ Channel Protein into Planar Lipid Bilayers. *Am. J. Physiol.* **1995**, *268*, C1148–56.

(37) Sariban-Sohraby, Sarah; Latorre, Ramon; Burg, Maurice; Olans, Lori; Benos, D. Amiloride-Sensitive Epithelial Na Channels Reconstituted into Planar Lipid Bilayer Membranes. *Nature* **1984**, *308*, 80–83.

(38) Guo, X. T.; Uehara, a; Ravindran, a; Bryant, S. H.; Hall, S.; Moczydlowski, E. Kinetic Basis for Insensitivity to Tetrodotoxin and Saxitoxin in Sodium Channels of Canine Heart and Denervated Rat Skeletal Muscle. *Biochemistry* **1987**, *26*, 7546–7556.

(39) Krueger, Bruce; Worley III, Jennings; French, R. Single Sodium Channels from Rat Brain Incorporated into Planar Lipid Bilayer Membranes. *Nature* **1983**, *303*, 172–175.

(40) Martin, C; Ashley, R. Reconstitution of a Voltage-Activated Calcium Conducting Cation Channel from Brain Microsomes. *Cell Calcium* **1993**, *14*, 427–438.

(41) Hymel, L. I. N.; Inui, M.; Fleischer, S.; Schindler, H. Purified Ryanodine Receptor of Skeletal Muscle Sarcoplasmic Reticulum Forms Ca2+-Activated Oligomeric Ca2+ Channels in Planar Bilayers. *Proc Natl Acad Sci U S A* **1988**, *85*, 441–445.

(42) Lai, A.; Erickson, H.; Rousseau, E.; Liu, Q.-Y.; Meissner, G. Purification and Reconstitution of the Calcium Release Channel from Skeletal Muscle. *Nature* **1988**, *331*, 315–319.

(43) Balden, E.; Walker, a M.; Cukierman, S. Reconstitution of Single Calcium Channels from Secretory Granules of Rat Adenohypophysis in Planar Lipid Membranes. *Mol. Cell. Endocrinol.* **1991**, *77*, 85–90.

(44) Stefani, E.; Fink, R.; Palade, P. T.; Bruin, G. Annu. Rev. Physiol. 51, 367 (1989). 2. **1992**, *207*.

(45) Nelson, M.; French, R.; Krueger, B. Voltage-Dependent Calcium Channels from Brian Incorporated into Planar Lipid Bilayers. *Nature* **1984**, *308*, 77–80.

(46) Rosenberg, R. L.; Hess, P.; Reeves, J. P. .; Smilowitz, H.; Tsien, R. W. . Calcium Channels in Planar Lipid Bilayers : Insights into Mechanisms of Ion Permeation and Gating. *Science (80-.).* **1986**, *231*, 1564–1566.

(47) Sehlatter, E.; Cneger, R.; Welsh, M. J.; Liedtke, C. M. P U R I F I c a T I O N a N D R E c O N S T I T U T I O N O F E P I T H E L I a L Chloride Channels. **1990**, *191*, 572–583.

(48) Ran, S.; Fuller, C. M.; Arrate, M. P.; Latorre, R.; Benos, D. J. Functional Reconstitution of a Chloride Channel Protein from Bovine Trachea. *J. Biol. Chem.* **1992**, *267*, 20630–20637.

(49) Salvail, D.; Cloutier, M.; Rousseau, E. Functional Reconstitution of an Eicosanoid-Modulated Cl- Channel from Bovine Tracheal Smooth Muscle. *Am. J. Physiol. Cell Physiol.* **2002**, *282*, C567–77.

(50) Singh, H.; Cousin, M. a; Ashley, R. H. Functional Reconstitution of Mammalian "Chloride Intracellular Channels" CLIC1, CLIC4 and CLIC5 Reveals Differential Regulation by Cytoskeletal Actin. *FEBS J.* **2007**, *274*, 6306–6316.

(51) Nelson N, Anholt R, Lindstrom J, M. M. Reconstitution of Purified Acetylcholine Receptors with Functional Ion Channels in Planar Lipid Bilayers. *Proc Natl Acad Sci U S A* **1980**, *77*, 3057–3061.

(52) Boheimt, G.; Hanket, W.; Barrantest, F. J.; Eiblo, H.; Sakmannf, B.; Fels, G.; Maelicke, A. Agonist-Activated Ionic Channels in Acetylcholine Receptor Reconstituted into Planar Lipid Bilayers. **1981**, *78*, 3586–3590.

(53) El-Arabi, A. M.; Salazar, C. S.; Schmidt, J. J. Ion Channel Drug Potency Assay with an Artificial Bilayer Chip. *Lab Chip* **2012**, *12*, 2409–2413.

(54) Portonovo, S. A.; Salazar, C. S.; Schmidt, J. J. hERG Drug Response Measured in Droplet Bilayers. *Biomed Microdevices* **2012**.

(55) Farre, C.; Fertig, N. HTS Techniques for Patch Clamp-Based Ion Channel Screening - Advances and Economy. *Expert Opin Drug Discov* **2012**, *7*, 515–524.

(56) Graef, J. D.; Benson, L. C.; Sidach, S. S.; Wei, H.; Lippiello, P. M.; Bencherif, M.; Fedorov, N. B. Validation of a High-Throughput, Automated Electrophysiology Platform for the Screening of Nicotinic Agonists and Antagonists. *J. Biomol. Screen.* **2013**, *18*, 116–127.

(57) Bennett, P. B.; Guthrie, H. R. E. Trends in Ion Channel Drug Discovery: Advances in Screening Technologies. *Trends Biotechnol.* **2003**, *21*, 563–569.

(58) Willumsen, N. J.; Bech, M.; Jensen, B. S.; Korsgaard, M. P. G.; Christophersen, P. High Throughput Electrophysiology : New Perspectives for Ion Channel Drug Discovery. **2003**, 3–12.

(59) Liebert, M. A. Ion Channel Drug Discovery. **2004**, *2*, 543–552.

(60) Schmidt, J. Stochastic Sensors. *J. Mater. Chem.* **2005**, *15*, 831.

(61) Glasmästar, K.; Larsson, C.; Höök, F.; Kasemo, B. Protein Adsorption on Supported Phospholipid Bilayers. *J. Colloid Interface Sci.* **2002**, *246*, 40–47.

(62) Knoll, W.; Frank, C. W.; Heibel, C.; Naumann, R.; Offenhäusser, a; Rühe, J.; Schmidt, E. K.; Shen, W. W.; Sinner, a. Functional Tethered Lipid Bilayers. *J. Biotechnol.* **2000**, *74*, 137–158.

(63) Bayley, H.; Martin, C. R. Resistive-Pulse Sensing-From Microbes to Molecules. *Chem. Rev.* **2000**, *100*, 2575–2594.

(64) Gu, L. Q.; Braha, O.; Conlan, S.; Cheley, S.; Bayley, H. Stochastic Sensing of Organic Analytes by a Pore-Forming Protein Containing a Molecular Adapter. *Nature* **1999**, *398*, 686–690.

(65) Bayley, H.; Braha, O.; Gu, L.-Q. Stochastic Sensing with Protein Pores. *Adv. Mater.* **2000**, *12*, 139–142.

(66) Braha, O.; Walker, B.; Cheley, S.; Kasianowicz, J. J.; Song, L.; Gouaux, J. E.; Bayley, H. Designed Protein Pores as Components for Biosensors. *Chem. Biol.* **1997**, *4*, 497–505.

(67) Braha, O.; Gu, L. Q.; Zhou, L.; Lu, X.; Cheley, S.; Bayley, H. Simultaneous Stochastic Sensing of Divalent Metal Ions. *Nat. Biotechnol.* **2000**, *18*, 1005–1007.

(68) Wu, H. C.; Bayley, H. Single-Molecule Detection of Nitrogen Mustards by Covalent Reaction within a Protein Nanopore. *J Am Chem Soc* **2008**, *130*, 6813–6819.

(69) Boersma, A. J.; Brain, K. L.; Bayley, H. Real-Time Stochastic Detection of Multiple Neurotransmitters with a Protein Nanopore. *ACS Nano* **2012**, *6*, 5304–5308.

(70) Rotem, D.; Jayasinghe, L.; Salichou, M.; Bayley, H. Protein Detection by Nanopores Equipped with Aptamers. *J Am Chem Soc* **2012**, *134*, 2781–2787.

(71) Rosen, C. B.; Rodriguez-Larrea, D.; Bayley, H. Single-Molecule Site-Specific Detection of Protein Phosphorylation with a Nanopore. *Nat. Biotechnol.* **2014**, *32*, 179–181.

(72) Kasianowicz, J. J.; Brandin, E.; Branton, D.; Deamer, D. W. Characterization of Individual Polynucleotide Molecules Using a Membrane Channel. *Proc. Natl. Acad. Sci. U. S. A.* **1996**, *93*, 13770–13773.

(73) Ashkenasy, N.; Sánchez-Quesada, J.; Ghadiri, M. R.; Bayley, H. Recognizing a Single Base in an Individual DNA Strand: A Step Toward Nanopore DNA Sequencing. **2005**, *44*, 1401–1404.

(74) Bayley, H. Sequencing Single Molecules of DNA. *Curr Opin Chem Biol* **2006**, *10*, 628–637.

(75) Akeson, M.; Branton, D.; Kasianowicz, J. J.; Brandin, E.; Deamer, D. W. Microsecond Time-Scale Discrimination among Polycytidylic Acid, Polyadenylic Acid, and Polyuridylic Acid as Homopolymers or as Segments within Single RNA Molecules. *Biophys. J.* **1999**, *77*, 3227–3233.

(76) Meller, a; Nivon, L.; Brandin, E.; Golovchenko, J.; Branton, D. Rapid Nanopore Discrimination between Single Polynucleotide Molecules. *Proc. Natl. Acad. Sci. U. S. A.* **2000**, *97*, 1079–1084.

(77) Astier, Y.; Braha, O.; Bayley, H. Toward Single Molecule DNA Sequencing: Direct Identification of Ribonucleoside and Deoxyribonucleoside 5'-Monophosphates by Using an Engineered Protein Nanopore Equipped with a Molecular Adapter. *J. Am. Chem. Soc.* **2006**, *128*, 1705–1710.

(78) Rincon-Restrepo, M.; Mikhailova, E.; Bayley, H.; Maglia, G. Controlled Translocation of Individual DNA Molecules through Protein Nanopores with Engineered Molecular Brakes. *Nano Lett.* **2011**, *11*, 746–750.

(79) Derrington, I. M.; Butler, T. Z.; Collins, M. D.; Manrao, E.; Pavlenok, M.; Niederweis, M.; Gundlach, J. H. Nanopore DNA Sequencing with MspA. *Proc. Natl. Acad. Sci. U. S. A.* **2010**, *107*, 16060–16065.

(80) Kumar, S.; Tao, C.; Chien, M.; Hellner, B.; Balijepalli, A.; Robertson, J. W.; Li, Z.; Russo, J. J.; Reiner, J. E.; Kasianowicz, J. J.; *et al.* PEG-Labeled Nucleotides and Nanopore Detection for Single Molecule DNA Sequencing by Synthesis. *Sci Rep* **2012**, *2*, 684.

(81) Xu, M.; Fujita, D.; Hanagata, N. Perspectives and Challenges of Emerging Single-Molecule DNA Sequencing Technologies. *Small* **2009**, *5*, 2638–2649.

(82) Bayley, H. Holes with an Edge. 15–17.

(83) Branton, D.; Deamer, D. W.; Marziali, A.; Bayley, H.; Benner, S. a; Butler, T.; Di Ventra, M.; Garaj, S.; Hibbs, A.; Huang, X.; *et al.* The Potential and Challenges of Nanopore Sequencing. *Nat. Biotechnol.* **2008**, *26*, 1146–1153.

(84) Manrao, E. A.; Derrington, I. M.; Laszlo, A. H.; Langford, K. W.; Hopper, M. K.; Gillgren, N.; Pavlenok, M.; Niederweis, M.; Gundlach, J. H. Reading DNA at Single-Nucleotide Resolution with a Mutant MspA Nanopore and phi29 DNA Polymerase. *Nat Biotechnol* **2012**, *30*, 349–353.

(85) Bayley, H. Sequencing Single Molecules of DNA. *Curr Opin Chem Biol* **2006**, *10*, 628–637.

(86) Wanunu, M. Nanopores: A Journey towards DNA Sequencing. *Phys Life Rev* **2012**, *9*, 125–158.

(87) Bayley, H.; Cremer, P. S. Stochastic Sensors Inspired by Biology. *Nature* **2001**, *413*, 226–230.

(88) Carney, R. P.; Astier, Y.; Carney, T. M.; Voïtchovsky, K.; Jacob Silva, P. H.; Stellacci, F. Electrical Method to Quantify Nanoparticle Interaction with Lipid Bilayers. *ACS Nano* **2013**, *7*, 932–942.

(89) De Planque, M. R. R.; Aghdaei, S.; Roose, T.; Morgan, H. Electrophysiological Characterization of Membrane Disruption by Nanoparticles. *ACS Nano* **2011**, *5*, 3599–3606.

(90) Negoda, A.; Kim, K.-J.; Crandall, E. D.; Worden, R. M. Polystyrene Nanoparticle Exposure Induces Ion-Selective Pores in Lipid Bilayers. *Biochim. Biophys. Acta* **2013**, *1828*, 2215–2222.

(91) Ramachandran, S.; Kumar, G. L.; Blick, R. H.; van der Weide, D. W. Current Bursts in Lipid Bilayers Initiated by Colloidal Quantum Dots. *Appl. Phys. Lett.* **2005**, *86*, 083901.

(92) Leroueil, P. R.; Berry, S. a; Duthie, K.; Han, G.; Rotello, V. M.; McNerny, D. Q.; Baker, J. R.; Orr, B. G.; Holl, M. M. B. Wide Varieties of Cationic Nanoparticles Induce Defects in Supported Lipid Bilayers. *Nano Lett.* **2008**, *8*, 420–424.

(93) Xiao, X.; Montaño, G. a; Edwards, T. L.; Allen, A.; Achyuthan, K. E.; Polsky, R.; Wheeler, D. R.; Brozik, S. M. Surface Charge Dependent Nanoparticle Disruption and Deposition of Lipid Bilayer Assemblies. *Langmuir* **2012**, *28*, 17396–17403.

(94) Leroueil, P. R.; Hong, S.; Mecke, A.; Jr, J. R. B.; Orr, G.; Holl, M. M. B. Nanoparticle Interaction with Biological Membranes. *Acc Chem Res.* **2007**, *40*, 335–342.

(95) Han, X.; Studer, a.; Sehr, H.; Geissbühler, I.; Di Berardino, M.; Winkler, F. K.; Tiefenauer, L. X. Nanopore Arrays for Stable and Functional Free-Standing Lipid Bilayers. *Adv. Mater.* **2007**, *19*, 4466–4470.

(96) Kleefen, A.; Pedone, D.; Grunwald, C.; Wei, R.; Firnkes, M.; Abstreiter, G.; Rant, U.; Tampe, R. Multiplexed Parallel Single Transport Recordings on Nanopore Arrays. *Nano Lett* **2010**.

(97) Smith, K. A.; Gale, B. K.; Conboy, J. C. Micropatterned Fluid Lipid Bilayer Arrays Created Using a Continuous Flow Microspotter. *Anal Chem* **2008**, *80*, 7980–7987.

(98) Castell, O. K.; Berridge, J.; Wallace, M. I. Quantification of Membrane Protein Inhibition by Optical Ion Flux in a Droplet Interface Bilayer Array. *Angew. Chem. Int. Ed. Engl.* **2012**, *51*, 3134–3138.

(99) Baaken, G.; Ankri, N.; Schuler, A. K.; Ruhe, J.; Behrends, J. C. Nanopore-Based Single-Molecule Mass Spectrometry on a Lipid Membrane Microarray. *ACS Nano* **2011**, *5*, 8080–8088.

(100) Suzuki, H.; Le Pioufle, B.; Takeuchi, S. Ninety-Six-Well Planar Lipid Bilayer Chip for Ion Channel Recording Fabricated by Hybrid Stereolithography. *Biomed Microdevices* **2009**, *11*, 17–22.

(101) Portonovo, S. A.; Schmidt, J. Masking Apertures Enabling Automation and Solution Exchange in Sessile Droplet Lipid Bilayers. *Biomed Microdevices* **2012**, *14*, 187–191.

(102) Kang, X.; Cheley, S.; Rice-Ficht, A. C.; Bayley, H. A Storable Encapsulated Bilayer Chip Containing a Single Protein Nanopore. *J. Am. Chem. Soc.* **2007**, *129*, 4701–4705.

(103) Heron, A. J.; Thompson, J. R.; Mason, A. E.; Wallace, M. I. Direct Detection of Membrane Channels from Gels Using Water-in-Oil Droplet Bilayers. *J. Am. Chem. Soc.* **2007**, *129*, 16042–16047.

(104) Thompson, J. R.; Heron, A. J.; Santoso, Y.; Wallace, M. I. Enhanced Stability and Fluidity in Droplet on Hydrogel Bilayers for Measuring Membrane Protein Diffusion. *Nano Lett.* **2007**, *7*, 3875–3878.

(105) Malmstadt, N.; Jeon, T. J.; Schmidt, J. J. Long-Lived Planar Lipid Bilayer Membranes Anchored to an In Situ Polymerized Hydrogel. *Adv. Mater.* **2008**, *20*, 84–89.

(106) Thompson, J. R.; Cronin, B.; Bayley, H.; Wallace, M. I. Rapid Assembly of a Multimeric Membrane Protein Pore. *Biophys. J.* **2011**, *101*, 2679–2683.

(107) Castell, O. K.; Berridge, J.; Wallace, M. I. Quantification of Membrane Protein Inhibition by Optical Ion Flux in a Droplet Interface Bilayer Array. *Angew Chem Int Ed Engl* **2012**, *51*, 3134–3138.

(108) Ota, S.; Suzuki, H.; Takeuchi, S. Microfluidic Lipid Membrane Formation on Microchamber Arrays. *Lab Chip* **2011**, *11*, 2485–2487.

(109) Parveen, S.; Misra, R.; Sahoo, S. K. Nanoparticles: A Boon to Drug Delivery, Therapeutics, Diagnostics and Imaging. *Nanomedicine* **2012**, *8*, 147–166.

(110) De Jong, W. H.; Borm, P. J. a. Drug Delivery and Nanoparticles:applications and Hazards. *Int. J. Nanomedicine* **2008**, *3*, 133–149.

(111) Davis, M. E.; Chen, Z. G.; Shin, D. M. Nanoparticle Therapeutics: An Emerging Treatment Modality for Cancer. *Nat. Rev. Drug Discov.* **2008**, *7*, 771–782.

(112) Baptista, P. V; Doria, G.; Quaresma, P.; Cavadas, M.; Neves, C. S.; Gomes, I.; Eaton, P.; Pereira, E.; Franco, R. Nanoparticles in Molecular Diagnostics. *Prog. Mol. Biol. Transl. Sci.* **2011**, *104*, 427–488.

(113) Chapman, S.; Dobrovolskaia, M.; Farahani, K.; Goodwin, A.; Joshi, A.; Lee, H.; Meade, T.; Pomper, M.; Ptak, K.; Rao, J.; *et al.* Nanoparticles for Cancer Imaging: The Good, the Bad, and the Promise. *Nano Today* **2013**, *8*, 454–460.

(114) Kaiser, J.-P.; Diener, L.; Wick, P. Nanoparticles in Paints: A New Strategy to Protect Façades and Surfaces? *J. Phys. Conf. Ser.* **2013**, *429*, 012036.

(115) Robertson, T. a.; Sanchez, W. Y.; Roberts, M. S. Are Commercially Available Nanoparticles Safe When Applied to the Skin? *J. Biomed. Nanotechnol.* **2010**, *6*, 452–468.

(116) Buzea, C.; Pacheco, I. I.; Robbie, K. Nanomaterials and Nanoparticles: Sources and Toxicity. *Biointerphases* **2007**, *2*, MR17.

(117) Sapkota, A.; Symons, J. M.; Kleissl, J.; Wang, L.; Parlange, M. B.; Ondov, J.; Breysse, P. N.; Diette, G. B.; Eggleston, P. a; Buckley, T. J. Impact of the 2002 Canadian Forest Fires on Particulate Matter Air Quality in Baltimore City. *Environ. Sci. Technol.* **2005**, *39*, 24–32.

(118) Wind O. *110*, 80–87.

(119) Stephens, B.; Azimi, P.; El Orch, Z.; Ramos, T. Ultrafine Particle Emissions from Desktop 3D Printers. *Atmos. Environ.* **2013**, *79*, 334–339.

(120) Rogers, F.; Arnott, P.; Zielinska, B.; Sagebiel, J.; Kelly, K. E.; Wagner, D.; Lighty, J. S.; Sarofim, A. F. Real-Time Measurements of Jet Aircraft Engine Exhaust. *J. Air Waste Manag. Assoc.* **2005**, *55*, 583–593.

(121) Love, S. a; Maurer-Jones, M. a; Thompson, J. W.; Lin, Y.-S.; Haynes, C. L. Assessing Nanoparticle Toxicity. *Annu. Rev. Anal. Chem. (Palo Alto. Calif).* **2012**, *5*, 181–205.

(122) Marquis, B. J.; Love, S. a; Braun, K. L.; Haynes, C. L. Analytical Methods to Assess Nanoparticle Toxicity. *Analyst* **2009**, *134*, 425–439.

(123) Yu, T.; Malugin, A.; Ghandehari, H. Impact of Silica Nanoparticle Design on Cellular Toxicity and Hemolytic Activity. *ACS Nano* **2011**, *5*, 5717–5728.

(124) Dobrovolskaia, M. A.; Clogston, J. D.; Neun, B. W.; Hall, J. B.; Anil, K.; Mcneil, S. E. NIH Public Access. **2009**, *8*, 2180–2187.

(125) Chen, J.; Hessler, J. a; Putchakayala, K.; Panama, B. K.; Khan, D. P.; Hong, S.; Mullen, D. G.; Dimaggio, S. C.; Som, A.; Tew, G. N.; *et al.* Cationic Nanoparticles Induce Nanoscale Disruption in Living Cell Plasma Membranes. *J. Phys. Chem. B* **2009**, *113*, 11179–11185.

(126) Li, S.; Malmstadt, N. Deformation and Poration of Lipid Bilayer Membranes by Cationic Nanoparticles. *Soft Matter* **2013**, *9*, 4969.

(127) Yu, Y.; Granick, S. Pearling of Lipid Vesicles Induced by Nanoparticles. *J. Am. Chem. Soc.* **2009**, *131*, 14158–14159.

(128) Tatur, S.; Maccarini, M.; Barker, R.; Nelson, A.; Fragneto, G. Effect of Functionalized Gold Nanoparticles on Floating Lipid Bilayers. *Langmuir* **2013**, *29*, 6606–6614.

(129) Wang, B.; Zhang, L.; Chul, S.; Granick, S. Nanoparticle-Induced Surface Reconstruction of Phospholipid Membranes SCIENCES. **2008**, *105*.

(130) Corredor, C.; Hou, W.-C.; Klein, S. a.; Moghadam, B. Y.; Goryll, M.; Doudrick, K.; Westerhoff, P.; Posner, J. D. Disruption of Model Cell Membranes by Carbon Nanotubes. *Carbon N. Y.* **2013**, *60*, 67–75.

(131) Wang, F.; Bexiga, M. G.; Anguissola, S.; Boya, P.; Simpson, J. C.; Salvati, A.; Dawson, K. a. Time Resolved Study of Cell Death Mechanisms Induced by Amine-Modified Polystyrene Nanoparticles. *Nanoscale* **2013**, *5*, 10868–10876.

(132) Lu, B.; Kocharyan, G.; Schmidt, J. J. Lipid Bilayer Arrays: Cyclically Formed and Measured. *Biotechnol. J.* **2013**, n/a–n/a.

(133) Iversen, T.-G.; Skotland, T.; Sandvig, K. Endocytosis and Intracellular Transport of Nanoparticles: Present Knowledge and Need for Future Studies. *Nano Today* **2011**, *6*, 176–185.

(134) Van Meer, G.; de Kroon, A. I. P. M. Lipid Map of the Mammalian Cell. *J. Cell Sci.* **2011**, *124*, 5–8.

(135) Monopoli, M. P.; Aberg, C.; Salvati, A.; Dawson, K. a. Biomolecular Coronas Provide the Biological Identity of Nanosized Materials. *Nat. Nanotechnol.* **2012**, *7*, 779–786.

(136) Doorley, G. W.; Payne, C. K. Cellular Binding of Nanoparticles in the Presence of Serum Proteins. *Chem. Commun. (Camb).* **2011**, *47*, 466–468.

(137) Wang, F.; Yu, L.; Monopoli, M. P.; Sandin, P.; Mahon, E.; Salvati, A.; Dawson, K. a. The Biomolecular Corona Is Retained during Nanoparticle Uptake and Protects the Cells from the Damage Induced by Cationic Nanoparticles until Degraded in the Lysosomes. *Nanomedicine* **2013**, *9*, 1159–1168.

(138) Giovia, A.; Follo, C.; Caputo, G.; Isidoro, C. Trafficking of Mesoporous Silica and Polystyrene Nanoparticles in Ovarian Cancer Cells : Effects of Size and Surface Charge Groups. **2012**, 4147–4158.

(139) Scott, C. C.; Gruenberg, J. Ion Flux and the Function of Endosomes and Lysosomes: pH Is Just the Start: The Flux of Ions across Endosomal Membranes Influences Endosome Function Not Only through Regulation of the Luminal pH. *Bioessays* **2011**, *33*, 103–110.

(140) Partha, R.; Conyers, J. L. Biomedical Applications of Functionalized Fullerene-Based Nanomaterials. *Int. J. Nanomedicine* **2009**, *4*, 261–275.

(141) Dellinger A, Zhou Z, Connor J, Madhankumar AB, Pamujula S, Sayes CM, K. C. Application of Fullerenes in Nanomedicine: An Update. *Nanomedicine （Lond)* **2013**, *8*, 1191–1208.

(142) Xu, C.; Qu, X. Cerium Oxide Nanoparticle: A Remarkably Versatile Rare Earth Nanomaterial for Biological Applications. *NPG Asia Mater.* **2014**, *6*, e90.

(143) Xu, C.; Lin, Y.; Wang, J.; Wu, L.; Wei, W.; Ren, J.; Qu, X. Nanoceria-Triggered Synergetic Drug Release Based on CeO(2) -Capped Mesoporous Silica Host-Guest

Interactions and Switchable Enzymatic Activity and Cellular Effects of CeO(2). *Adv. Healthc. Mater.* **2013**, *2*, 1591–1599.

(144) Li, M.; Shi, P.; Xu, C.; Ren, J.; Qu, X. Cerium Oxide Caged Metal Chelator: Anti-Aggregation and Anti-Oxidation Integrated H2O2-Responsive Controlled Drug Release for Potential Alzheimer's Disease Treatment. *Chem. Sci.* **2013**, *4*, 2536.

(145) Wason, M. S.; Zhao, J. Cerium Oxide Nanoparticles: Potential Applications for Cancer and Other Diseases. *Am. J. Transl. Res.* **2013**, *5*, 126–131.

(146) Celardo, I.; Pedersen, J. Z.; Traversa, E.; Ghibelli, L. Pharmacological Potential of Cerium Oxide Nanoparticles. *Nanoscale* **2011**, *3*, 1411–1420.

(147) Liu, X.; Qiu, G.; Li, X. Shape-Controlled Synthesis and Properties of Uniform Spinel Cobalt Oxide Nanocubes. *Nanotechnology* **2005**, *16*, 3035–3040.

(148) Lee, Y.; Choi, J.-R.; Lee, K. J.; Stott, N. E.; Kim, D. Large-Scale Synthesis of Copper Nanoparticles by Chemically Controlled Reduction for Applications of Inkjet-Printed Electronics. *Nanotechnology* **2008**, *19*, 415604.

(149) Ahamed, M.; Alhadlaq, H. A.; Khan, M. A. M.; Karuppiah, P.; Al-dhabi, N. A. Synthesis , Characterization , and Antimicrobial Activity of Copper Oxide Nanoparticles. **2014**, *2014*.

(150) Rahnama, A.; Gharagozlou, M. Preparation and Properties of Semiconductor CuO Nanoparticles via a Simple Precipitation Method at Different Reaction Temperatures. *Opt. Quantum Electron.* **2012**, *44*, 313–322.

(151) Jiang, L.-C.; Zhang, W.-D. A Highly Sensitive Nonenzymatic Glucose Sensor Based on CuO Nanoparticles-Modified Carbon Nanotube Electrode. *Biosens. Bioelectron.* **2010**, *25*, 1402–1407.

(152) Song, M.-J.; Hwang, S. W.; Whang, D. Non-Enzymatic Electrochemical CuO Nanoflowers Sensor for Hydrogen Peroxide Detection. *Talanta* **2010**, *80*, 1648–1652.

(153) Radziuk, D.; Skirtach, A.; Gessner, A.; Kumke, M. U.; Zhang, W.; Möhwald, H.; Shchukin, D. Ultrasonic Approach for Formation of Erbium Oxide Nanoparticles with Variable Geometries. *Langmuir* **2011**, *27*, 14472–14480.

(154) Feng, J.; Shan, G.; Maquieira, A.; Koivunen, M. E.; Guo, B.; Hammock, B. D.; Kennedy, I. M. Used as a Fluorescent Label in an Immunoassay for Atrazine. **2003**, *75*, 5282–5286.

(155) Abrikossova, N.; Skoglund, C.; Ahrén, M.; Bengtsson, T.; Uvdal, K. Effects of Gadolinium Oxide Nanoparticles on the Oxidative Burst from Human Neutrophil Granulocytes. *Nanotechnology* **2012**, *23*, 275101.

(156) Ramadoss, A.; Krishnamoorthy, K.; Kim, S. J. Facile Synthesis of Hafnium Oxide Nanoparticles via Precipitation Method. *Mater. Lett.* **2012**, *75*, 215–217.

(157) Rivera Gil, P.; Hühn, D.; del Mercato, L. L.; Sasse, D.; Parak, W. J. Nanopharmacy: Inorganic Nanoscale Devices as Vectors and Active Compounds. *Pharmacol. Res.* **2010**, *62*, 115–125.

(158) Soulantica, K.; Erades, L.; Sauvan, M.; Senocq, F.; Maisonnat, a.; Chaudret, B. Synthesis of Indium and Indium Oxide Nanoparticles from Indium Cyclopentadienyl Precursor and Their Application for Gas Sensing. *Adv. Funct. Mater.* **2003**, *13*, 553–557.

(159) Elouali, S.; Bloor, L. G.; Binions, R.; Parkin, I. P.; Carmalt, C. J.; Darr, J. a. Gas Sensing with Nano-Indium Oxides (In2O3) Prepared via Continuous Hydrothermal Flow Synthesis. *Langmuir* **2012**, *28*, 1879–1885.

(160) Kumar, M.; Singh, V. N.; Mehta, B. R.; Singh, J. P. Tunable Synthesis of Indium Oxide Octahedra, Nanowires and Tubular Nanoarrow Structures under Oxidizing and Reducing Ambients. *Nanotechnology* **2009**, *20*, 235608.

(161) Han, S.-Y.; Herman, G. S.; Chang, C. Low-Temperature, High-Performance, Solution-Processed Indium Oxide Thin-Film Transistors. *J. Am. Chem. Soc.* **2011**, *133*, 5166–5169.

(162) Zhang, D.; Li, C.; Han, S.; Liu, X.; Tang, T.; Jin, W.; Zhou, C. Ultraviolet Photodetection Properties of Indium Oxide Nanowires. *Appl. Phys. A Mater. Sci. Process.* **2003**, *77*, 163–166.

(163) Gupta, A. K.; Gupta, M. Synthesis and Surface Engineering of Iron Oxide Nanoparticles for Biomedical Applications. *Biomaterials* **2005**, *26*, 3995–4021.

(164) Shen, Y. F.; Tang, J.; Nie, Z. H.; Wang, Y. D.; Ren, Y.; Zuo, L. Preparation and Application of Magnetic Fe3O4 Nanoparticles for Wastewater Purification. *Sep. Purif. Technol.* **2009**, *68*, 312–319.

(165) Khanjani, S.; Morsali, A. Synthesis and Characterization of Lanthanum Oxide Nanoparticles from Thermolysis of Nanostructured Supramolecular Compound. *J. Mol. Liq.* **2010**, *153*, 129–132.

(166) Yang, J.; Nie, Z.; Wang, Y. Microstructure and Emission Ability of Rare Earth Oxides Doped Molybdenum Cathodes. *Appl. Surf. Sci.* **2003**, *215*, 87–95.

(167) Nanoparticles, B.; Bouzigues, C.; Gacoin, T.; Alexandrou, A. Biological Applications of Rare-Earth. *ACS Nano* **2011**, *5*, 8488–8505.

(168) Yamagishi, Y.; Watari, A.; Hayata, Y.; Li, X.; Kondoh, M.; Yoshioka, Y.; Tsutsumi, Y.; Yagi, K. Acute and Chronic Nephrotoxicity of Platinum Nanoparticles in Mice. *Nanoscale Res. Lett.* **2013**, *8*, 395.

(169) Kwon, S. J.; Bard, A. J. DNA Analysis by Application of Pt Nanoparticle Electrochemical Ampli Fi Cation with Single Label Response. *J Am Chem Soc* **2012**, *134*, 10777–10779.

(170) Chen, M.; Yang, Z.; Wu, H.; Pan, X.; Xie, X.; Wu, C. Antimicrobial Activity and the Mechanism of Silver Nanoparticle Thermosensitive Gel. *Int. J. Nanomedicine* **2011**, *6*, 2873–2877.

(171) Chen, X.; Schluesener, H. J. Nanosilver: A Nanoproduct in Medical Application. *Toxicol. Lett.* **2008**, *176*, 1–12.

(172) Ghosh, M.; Chakraborty, A.; Mukherjee, A. Cytotoxic, Genotoxic and the Hemolytic Effect of Titanium Dioxide (TiO2) Nanoparticles on Human Erythrocyte and Lymphocyte Cells in Vitro. *J. Appl. Toxicol.* **2013**, *33*, 1097–1110.

(173) Vamanu, C. I.; Cimpan, M. R.; Høl, P. J.; Sørnes, S.; Lie, S. a; Gjerdet, N. R. Induction of Cell Death by TiO2 Nanoparticles: Studies on a Human Monoblastoid Cell Line. *Toxicol. In Vitro* **2008**, *22*, 1689–1696.

(174) Jin, C.-Y.; Zhu, B.-S.; Wang, X.-F.; Lu, Q.-H. Cytotoxicity of Titanium Dioxide Nanoparticles in Mouse Fibroblast Cells. *Chem. Res. Toxicol.* **2008**, *21*, 1871–1877.

(175) Liu, Y.; He, L.; Mustapha, a; Li, H.; Hu, Z. Q.; Lin, M. Antibacterial Activities of Zinc Oxide Nanoparticles against Escherichia Coli O157:H7. *J. Appl. Microbiol.* **2009**, *107*, 1193–1201.

(176) Rasmussen, J. W.; Martinez, E.; Louka, P.; Wingett, D. G. Zinc Oxide Nanoparticles for Selective Destruction of Tumor Cells and Potential for Drug Delivery Applications. *Expert Opin Drug Discov* **2010**, *7*, 1063–1077.

(177) Li, R.; Ji, Z.; Chang, C. H.; Dunphy, D. R.; Cai, X.; Meng, H.; Zhang, H.; Sun, B.; Wang, X.; Dong, J.; *et al.* Surface Interactions with Compartmentalized Cellular Phosphates Explain Rare Earth Oxide Nanoparticle Hazard and Provide Opportunities for Safer Design. *ACS Nano* **2014**, *8*, 1771–1783.

(178) El Badawy, A. M.; Silva, R. G.; Morris, B.; Scheckel, K. G.; Suidan, M. T.; Tolaymat, T. M. Surface Charge-Dependent Toxicity of Silver Nanoparticles. *Environ. Sci. Technol.* **2011**, *45*, 283–287.

(179) Chwalibog, A.; Sawosz, E.; Hotowy, A.; Szeliga, J.; Mitura, S.; Mitura, K.; Grodzik, M.; Orlowski, P.; Sokolowska, A. Visualization of Interaction between Inorganic Nanoparticles and Bacteria or Fungi. *Int. J. Nanomedicine* **2010**, *5*, 1085–1094.

(180) Papis, E.; Rossi, F.; Raspanti, M.; Dalle-Donne, I.; Colombo, G.; Milzani, A.; Bernardini, G.; Gornati, R. Engineered Cobalt Oxide Nanoparticles Readily Enter Cells. *Toxicol. Lett.* **2009**, *189*, 253–259.

(181) Ghodake, G.; Seo, Y. D.; Lee, D. S. Hazardous Phytotoxic Nature of Cobalt and Zinc Oxide Nanoparticles Assessed Using Allium Cepa. *J. Hazard. Mater.* **2011**, *186*, 952–955.

(182) Tanaka, A.; Hirata, M.; Homma, T.; Kiyohara, Y. Chronic Pulmonary Toxicity Study of Indium-Tin Oxide and Indium Oxide Following Intratracheal Instillations into the Lungs of Hamsters. *J. Occup. Health* **2010**, *52*, 14–22.

(183) Song, W.; Zhang, J.; Guo, J.; Zhang, J.; Ding, F.; Li, L.; Sun, Z. Role of the Dissolved Zinc Ion and Reactive Oxygen Species in Cytotoxicity of ZnO Nanoparticles. *Toxicol. Lett.* **2010**, *199*, 389–397.

(184) Yang, Q.; Ma, Y. Irradiation-Enhanced Cytotoxicity of Zinc Oxide Nanoparticles. *Int. J. Toxicol.* **2014**, *33*, 187–203.

(185) Karlsson, H. L.; Cronholm, P.; Hedberg, Y.; Tornberg, M.; De Battice, L.; Svedhem, S.; Wallinder, I. O. Cell Membrane Damage and Protein Interaction Induced by Copper Containing Nanoparticles--Importance of the Metal Release Process. *Toxicology* **2013**, *313*, 59–69.

(186) Prylutska, S.; Bilyy, R.; Overchuk, M.; Bychko, a.; Andreichenko, K.; Stoika, R.; Rybalchenko, V.; Prylutskyy, Y.; Tsierkezos, N. G.; Ritter, U. Water-Soluble Pristine Fullerenes C₆₀ Increase the Specific Conductivity and Capacity of Lipid Model Membrane and Form the Channels in Cellular Plasma Membrane. *J. Biomed. Nanotechnol.* **2012**, *8*, 522–527.

(187) Karlsson, H. L.; Cronholm, P.; Gustafsson, J.; Möller, L. Copper Oxide Nanoparticles Are Highly Toxic: A Comparison between Metal Oxide Nanoparticles and Carbon Nanotubes. *Chem. Res. Toxicol.* **2008**, *21*, 1726–1732.

(188) Field, J. a; Luna-Velasco, A.; Boitano, S. a; Shadman, F.; Ratner, B. D.; Barnes, C.; Sierra-Alvarez, R. Cytotoxicity and Physicochemical Properties of Hafnium Oxide Nanoparticles. *Chemosphere* **2011**, *84*, 1401–1407.

(189) Yanagi, I.; Akahori, R.; Hatano, T.; Takeda, K. Pulse-Voltage Injection. *Sci Rep* **2014**, 1–7.

(190) Li, J.; Stein, D.; Mcmullan, C.; Branton, D. Ion-Beam Sculpting at Nanometre Length Scales. *Nature* **2001**, *412*, 2–5.